Title: Sensing mechanism in semiconducting hybrid structures for DMMP detection

Author: Paulina Powroźnik

Citation style: Powroźnik Paulina. (2020). Sensing mechanism in semiconducting hybrid structures for DMMP detection. Praca doktorska. Katowice : Uniwersytet Śląski

UNIVERSITY OF SILESIA
FACULTY OF SCIENCE AND TECHNOLOGY

AUGUST CHEŁKOWSKI INSTITUTE OF PHYSICS

Doctoral Thesis

SENSING MECHANISM IN SEMICONDUCTING HYBRID STRUCTURES FOR DMMP DETECTION

Paulina Powroźnik

Doctoral thesis done
at the Institute of Physics –
Center for Science and Education
at Silesian University of Technology
in Gliwice

Supervisor:
dr hab. inż. Wiesław Jakubik, prof. PŚ
Auxiliary Supervisor:
dr hab. inż. Maciej Krzywiecki

Gliwice 2020

Acknowledgements

This thesis was partially financed by the National Science Center Poland project number 2016/21/N/ST5/03335 titled “Sensing mechanisms in hybrid detectors of chemical warfare agents”. The author’s traineeship at the Department of Physics of Durham University was funded by the ORZEL project (European Union's Horizon 2020 grant number 691684). The DFT calculations have been carried out using grants for computer time from the Paderborn Center for Parallel Computing (PC^2). The photoelectron spectroscopies, thermal desorption spectroscopy, atomic force microscopy and sensor response measurements have been performed in the Electron Spectroscopies and Functional Materials Laboratory (ESpeFuM) at the Institute of Physics, Silesian University of Technology.

I would like to sincerely thank my Supervisors, prof. Wiesław Jakubik and dr hab. Maciej Krzywiecki for their scientific support, discussions and for motivating me for work and constant development. I would like to thank them also for their kindness and all the help that I received from them.

I would like to express my gratitude to all the people that directly contributed to results of this dissertation. I am grateful to prof. Wolf Gero Schmidt and his group, particularly dr Uwe Gerstmann and dr Hazem Aldahhak, for inviting me for a stage and helping me to learn and to perform DFT calculations. I thank professor’s Andrew Monkman group of Electroactive Organic Materials at Durham University for giving me a possibility to prepare the samples for my research during my traineeship at their laboratory. I am grateful to the Head of Division of Applied Physics, prof. Jerzy Bodzenta for allowing me to do my research at DAP, giving me useful advices regarding my work and being supportive. I would like to thank prof. Lucyna Grządziel for the scientific discussions, help in the interpretation of results and her kindness and support. I thank dr Łukasz Drewniak for the technical help with experiments and for being friendly and helpful officemate. I thank dr Agata Blacha-Grzechnik for giving me opportunity to participate in ORZEL project, her friendly support, help in thesis editing and for bringing me to work. I thank Jarosław Wrotniak for helping me to set up the sensor response laboratory.

I want to thank all my colleagues, those that I mentioned above and also Justyna, Dominika, Ania, Basia, Alina and Ania for all the support and help, coffee breaks and a nice atmosphere at work.

I am grateful to my mother for not giving up and to my late father for trying to do his best. I thank my sister for being my best friend and for supporting me in all the ways. I thank Franco for putting up with me in these last years, supporting me and encouraging me to do my best.

I also thank all my friends. Finally, I would like to thank my cat Newton that has been studying and writing with me for almost ten years.

The thesis is organized as follows: in the Chapter 1 the motivation of the research carried out within this thesis is introduced basing on the state of the art and the objectives of the thesis are presented; the Chapter 2 gives a theoretical background about gas sensing principles, including the definitions and classification of gas sensors, the theory of gas adsorption and its influence on semiconductor's surface; in the Chapter 3 the literature review about semiconducting materials investigated in the field of gas sensors, especially for DMMP detection, is presented; in Chapter 4, the theoretical and experimental methods for sensing mechanisms evaluation applied in this thesis are described; in the Chapter 5 the original results of research performed within this thesis are presented; in the Chapter 6 the most important outcomes of the studies presented in the thesis are summarized and concluded, and the outlook for the future work is proposed.

The preliminary study presented in the sections 5.1.2 and 5.1.3 has been published in the Eurosensors 2015 and Eurosensors 2016 conferences proceedings:

- P. Powroźnik, W. Jakubik, A. Kaźmierczak-Bałata, Detection of organophosphorus (DMMP) vapour using phthalocyanine-palladium bilayer structures, Procedia Engineering 120 (2015), 368-371;
- P. Powroźnik, M. Krzywiecki., L. Grządziel., W. Jakubik, Study of Sensing Mechanisms in Nerve Agent Sensors Based on Phthalocyanine-palladium Structures, Procedia Engineering (2016) 168, 586-589.

The main results shown in the sections 5.1.4 and 5.2 have been published in the Sensors and Actuators B: Chemical and The Journal of Physical Chemistry C journals:

- P. Powroźnik, L. Grządziel, W. Jakubik, M. Krzywiecki, Sensors and Actuators B: Chemical (2018) 273, 771-777.
- H. Aldahhak, P. Powroźnik, P. H. Pander, W. Jakubik, F. B. Dias, W. G. Schmidt, U. Gerstmann and M. Krzywiecki, https://pubs.acs.org/doi/10.1021/acs.jpcc.9b11116

1 Introduction

1.1 Motivation

Gas sensors attracted big interest due to their wide range of applications in many fields, e. g. environmental protection, combustion gases detection, medical diagnosis, military and civil safety. In order to successfully develop detection techniques, new sensing materials are being constantly searched as well as the modifications of well-known sensing materials are applied. In the last decades especially the research of chemical warfare agent, sarin has been intensified.

Chemical warfare agents (CWA) are lethal class of compounds that threaten civilians. Nowadays, in response to terroristic activity, there is an urgent need for sensitive, selective and fast sensors of CWA. CWA can be classified in four categories: nerve agents, choking agents, blister agents and blood agents. Among *G*-series nerve agents, sarin is an organophosphorus compound classified as weapon of mass destruction by UN Resolution No. 687. It can cause death by suffocation within 1 – 10 min. Disabling and lethal exposures to sarin occur above 15 ppb and 64 ppb respectively for 10 min of exposure[1]. Sensing devices are required to detect extremely low sarin concentration in a very short time. At the same time, the sensor production and operation costs are important issues. The thorough, atom scale understanding of the sensing mechanism is expected to be extremely helpful to tune respective devices and eventually to realize competitive sensor components for industrial production.

Due to the safety requirements, for sarin sensors investigation in laboratory work simulant of sarin - dimethyl methylphosphonate (DMMP), reducing gas[2] is commonly used[3] (Figure 1.1). It has similar chemical structure to sarin, but it is much less toxic. Both – sarin and DMMP possess the same characteristic P=O group that plays the important role in their detection.

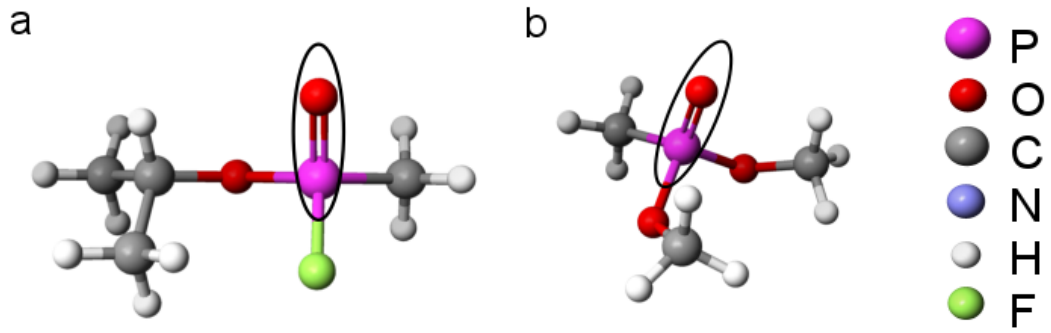

Figure 1.1. Chemical structure of a: Sarin b: DMMP (sarin simulant). Both – sarin and DMMP possess the same characteristic P=O group that plays the important role in the detection

In last two decades many materials e.g. carbon nanotubes[4,5,6], zeolites[7] and organic compounds[8,9,10] were studied as DMMP sensors and modifications to improve sensitivity and selectivity of semiconductive metal oxides were proposed[11,12,13]. However, the potential new materials and structures for effective DMMP sensing are still being widely investigated.

This thesis is focused on sensing mechanism evaluation in DMMP detection with sensing structures based on phthalocyanines (Pc). Pcs, both metal-free pthalocyanines (H_2Pc) and metallo-phthalocyanines (MPc) are organic semiconductors that have been widely studied in the field of organic electronics[14,15,16,17,18,19,20,21]. They have been especially applied in solar cells[14,15,16,17] and gas sensors[18,19,20,21]. They are good gas sensitive materials because of their thermal and chemical stabilities and a strong dependence of electrical conductivity on chemical species present in the atmosphere[22]. Other reasons to use phthalocyanines as gas sensitive materials are their ease of deposition as high quality films, and the possibility of functionalization by changing the central atom or adding substitutes to the phthalocyanine rings[18,20,23,24,25] and creation of hybrid structures with other materials[26,27,28,29].

The sensitivity of phthalocyanines (i. e. H_2Pc, CuPc, NiPc, PbPc, ZnPc) to DMMP has been reported in several papers[2,30,31,32]. However, the electrical conductivity changes of devices based on bare phthalocyanine layers exposed to DMMP were not satisfying. In order to understand the origin of weak electrical responses of Pc films to DMMP, the full understanding of processes occurring during DMMP adsorption on Pc surface is necessary. Bohrer *et al.*[2] attributed the low sensor response of MPcs to weak electron donors to the low availability of the strongest adsorption sites, i.e., metal centers, due to the oxygen adsorption from ambience. Yet, there are other conceivable factors which might be responsible such as the orientation of the Pc molecules within the sensing layer or the charge redistribution upon the gas adsorption. There is a number of theoretical studies available on molecular adsorption on phthalocyanines[33,34]. However, they did not take into account those factors. They were focused on single gas molecule interaction with isolated Pc molecule. This approach neglects such aspects as adsorption sites availability due to the Pc molecules orientation in the sensing layer and the charge relocation between Pc molecules.

On the other hand, the interaction of DMMP with semiconducting metal oxides (SMOs), i.e. SnO_2, ZnO, TiO_2, MgO, WO_3, SiO_2, Y_2O_3, Fe_2O_3, Al_2O_3, has been well recognized by experimental methods[35,36,37,38,39,40,41,42,43,44,45,46,47]. In the last decade also theoretical studies of DMMP adsorption on various semiconducting metal oxides (SMOs) have been developed[48,49,50,51,52]. The SMOs reveal good sensitivity to DMMP with relatively high conductivity changes in the presence of this organophosphorus compound. However, the disadvantage of SMOs as gas sensors in general are their high operating temperature (200-500 ^oC)[53] and poor selectivity[54]. The intention of the proposed concept to utilize SMO/Pc hybrid structures is to combine well known sensing properties of metal oxides, such as high changes of electrical conductivity in the presence of reducing and oxidizing gases and good stability with advantages of Pcs, such as low work temperature and better selectivity compared to SMOs. It this thesis MoO_3 has been chosen among SMOs to investigate hybrid SMO/Pc structures. MoO_3 has been studied as a potential material for gas sensors for more than twenty years[55,56,57,58] as an alternative for other SMOs such as SnO_2 or ZnO. It was found that MoO_3 exhibits good sensitivity especially to reducing agents, such as H_2[59,60], CO[58,61], NH_3[62,63] and CH_4[64]. In the last decade these studies have been intensified, focusing mostly on modification of MoO_3 morphology to achieve better sensing performance[65,66,67,68]. In the context of DMMP detection, it is worth noting that most of the recent papers reported sensitivity of MoO_3 to organic compounds, such as ethanol[63,64], methanol[64], trimethylamine[65] and xylene[61]. Given that DMMP is an organic reducing agent, MoO_3 is a good candidate for its detection. Furthermore,

MoO_3 possesses such advantages as lower work temperature than other SMO sensing materials[53] and ease of deposition by thermal evaporation[54].
Following Jakubik et al. previous expertise with double-layered Pc structures in hydrogen detection[69], the Pd ultra-thin layers were used as the catalyst to enhance the sensing properties of H_2Pc. It was assumed that the mechanism of sensor response increase in the presence of palladium can be of a double nature. If the palladium remains in its metallic form, the process is augmented by palladium clusters which due to their interaction with reducing gases[70,71] enhance the diffusion of DMMP into the sensing structure. However, in the certain conditions during technological process, the palladium can be oxidized forming palladium(II) oxide[72], which can probably interact with DMMP similarly to other metal oxides[2,73]. The adsorption of DMMP on the PdO has not been yet considered and investigated.
The gas adsorption and its impact on the sensing material are of crucial importance for the sensor design[74,75,76,77]. However, most of the research is based on sensing properties studies without comprehensive evaluation of mechanisms responsible for sensor performance. In this thesis the fundamental approach to gas adsorption mechanisms investigation is proposed. The methodology is based on the theoretical and experimental study of adsorption energies, preferable adsorption sites determination and charge relocation and associated changes in electronic structure. Theoretical approach is based on semi-empirical and ab-initio modeling of sensing structure's surface interaction with a DMMP molecule. Results of such computer simulations provide information on adsorption energies, chemical bonds formed, dipolar momentums, charge transfer between sensing structure and adsorbed gas and changes in electronic structure caused by gas adsorption. Adsorption energy is the basic parameter that gives the information about the type of adsorption – higher energies suggest stronger chemisorption, while for their low values we can assume physical interaction between molecules. This information indicates materials for further experimental investigation and together with results of experiments allow the comprehensive sensing mechanism description. Experimental methods can be divided into three main groups:

- microscopic methods – sensing structure's surface topography investigation;
- spectroscopic methods – study of chemical composition and electronic structure;
- electrical methods – sensor responses measurements, e. g. by electrical resistance monitoring.

The main part of experimental sensing mechanism evaluation is a study of sensing structures surface chemical composition and electronic structure as well as adsorbed species determination. For this purpose photoelectron spectroscopies (PES) - X-ray (XPS) and ultraviolet (UPS), and thermal desorption spectroscopy (TDS) are utilized. Sensing responses are measured by the most widespread electrical resistance monitoring method. To properly describe the sensing mechanism, the knowledge on surface morphology and topography of the examined samples is essential. The main issue is to determine the surface roughness (R_a) which is crucial for sensing layers: the more developed is the surface the more adsorption active sites are available for any adsorbate detection. In order to investigate sensing structures' topography, atomic force microscopy is utilized. The last step is a measurement of sensing responses through electrical resistance changes.

1.2 Aims and scopes

To the best of author's knowledge there are no literature reports on DMMP detection using hybrid sensing structures based on Pcs, SMOs and Pd. Moreover, there is a lack of comprehensive study of adsorption mechanisms responsible for DMMP detection by Pcs. Therefore, the aims of this thesis are as follows:

- Development of a fundamental approach for gas sensors investigation based on computational modeling and experimental investigation of gas adsorption mechanisms;
- Application of the proposed methodology for evaluation of sensing mechanisms in DMMP detection by semiconducting hybrid structures based on selected Pcs and metal oxides.

In order to meet the objectives, following characterization methods have been applied:

- Theoretical modeling of DMMP adsorption by semi-empirical and DFT methods;
- Electrical sensor response measurements;
- Surface topography characterization by AFM;
- Electronic and chemical structure characterization by XPS and UPS;
- Desorption study by TDS technique.

2 Gas sensing principles

2.1 Definition and classification of chemical sensors

Sensors are devices that transform some nonelectrical values into the measurable electrical or other physical (mass, optical parameters, elastic modulus) signal. It should reproduce the input signal x into output signal y by a function $y=f(x)$ (Figure 2.1).

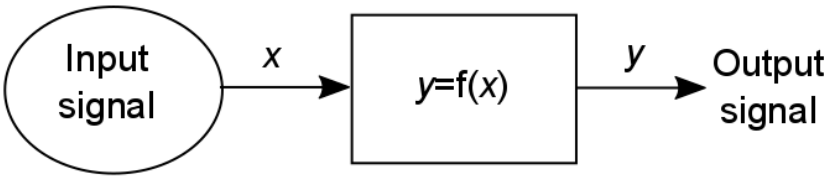

Figure 2.1. The work principle of sensors – transformation of some nonelectrical values into the measurable electrical or other physical (mass, optical parameters) signal. The input signal x should be reproduced into output signal y by a function $y=f(x)$

The sensors that are of particular interest in this thesis are chemical sensors in which the input signal can be a presence of a particular substance, the concentration of gas or organic compound vapor, pH level or humidity. According to IUPAC (International Union of Pure and Applied Chemistry) chemical sensors are devices that transform chemical information (i.e. about toxic gases in the atmosphere) into the analytical signal[78]. R. W. Catterall defined chemical sensor as a device which responds to a particular analyte in a selective way through a chemical reaction and can be used for the qualitative or quantitative determination of the analyte[79].
The received information can be a result of chemical reaction or physical properties of investigated object. The work principle of chemical sensors is based on the changes of at least one property of a sensor as a result of interaction with a detected substance (i.e. gas molecules). Those changes are transformed into measurable signal. The chemical sensor consists of two main elements – receptor and transducer (Figure 2.2). The receptor is a layer of chemically active material that reacts with a detected substance. Transducer converts measured chemical value into the output signal, e.g. electrical, optical, acoustic.

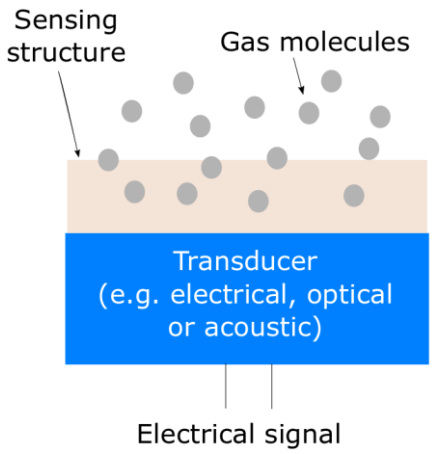

Figure 2.2. The schematic representation of chemical sensor which consists of two main elements: receptor (sensing layer or structure) and transducer.

According to the type of applied transducer, gas sensors can be divided into two main groups (Liu *et al.*[80]): based on variation in electrical properties and based on variation in other properties. The sensing methods based on variation in electrical properties are applied for materials like SMOs or organic semiconductors. Comini[81] made further classification of gas sensors based on variation of electrical properties according to the specific measurement method as following:

- DC conductometric gas sensors (chemoresistive gas sensors);
- Field-Effect-Transistors (FETs) based gas sensors;
- Photoluminescence (PL) based gas sensors.

Chemoresistive gas sensors are the most important group in the air pollution monitoring and toxic gases detection. They have been widely studied since eighty years and they are available commercially since 1962[82]. In the last five decades the application of chemoresistive gas sensors in many fields (household security, industrial emission control, environmental monitoring, vehicle emission control, biomedical field) has increased[83]. Today, the nanotechnology gives new opportunities of semiconducting sensing materials development and improvement of chemoresistive gas sensors properties[84]. At the same time notable part of research has been focused on FET based gas sensors that utilize electronic work function (WF) variation instead of electrical conductivity[85,86,87,88]. Recently, also gas sensors based on PL has gained interest in detection of gases such as i.e. CO[89], CO_2[90], H_2[91], O_3[92], H_2S[93].

2.2 Chemoresistive solid-state gas sensors work principle

Chemoresistive method of gas detection is based on measurements of changes in the electrical resistance of sensor layer (or sensor structure), caused by substances in the gaseous state. Output signal in this type of sensors is a result of change in the electrical conductivity of receptor-transducer element in presence of investigated gases, often in ppm concentration level. Chemoresistive gas sensor consists of four basic elements:

- receptor-transducer element – responsible for receiving information about a gas and converting into electrical signal; the base of this element is a sensing material or materials;
- substrate (e.g. silicon, aluminum oxide, glass);
- electrodes (e.g. gold, aluminum);
- heater.

The most widely used sensing materials are solid-state semiconductive materials, i.e. semiconductors. Adsorption of gas molecules on the sensing layer surface often leads to electrical charge transfer between semiconductor and investigated substance. In result of this transfer concentration of charge carriers in semiconductive layer changes, as a consequence electrical conductivity of receptor-transducer element is changed. In case of n-type semiconductor resistance decreases during reaction with reducing gases and increases in presence of oxidizing gases, for p-type semiconductors effect is reverse (Figure 2.3).

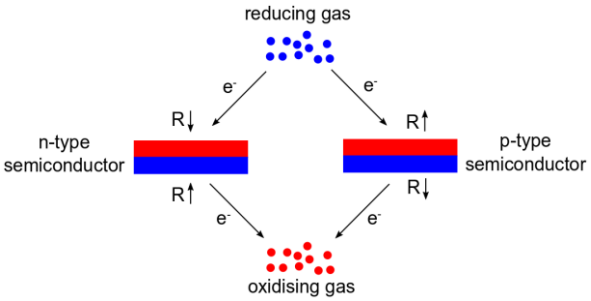

Figure 2.3. Work principle of chemoresistive solid-state gas sensor based on semiconducting material. Adsorption of gas molecules leads to of electrical transfer charge between semiconductor and investigated substance. As a consequence conductivity of receptor-transducer element is changed.

Single layers of bare semiconductors are often not efficient enough in gas sensing, so the common approach is using dopants or sensing structures consisting of two or more materials. The role of additional materials is to catalyze the interaction in order to improve the sensitivity or selectivity. More information on materials used in chemoresistive gas sensors will be given in the Chapter 3.

The work principle of gas sensors can be summarized in three couplings (Figure 2.4))[94]:

- first coupling – between gas molecules and sensing layer's parameters;
- second coupling – between sensing layer's parameters and detection setup;
- third coupling – signal processing (information about gas concentration).

The crucial step in gas sensors design is the first coupling – sensing mechanism evaluation. The full understanding of a sensing mechanism leads to the construction of a more efficient device.

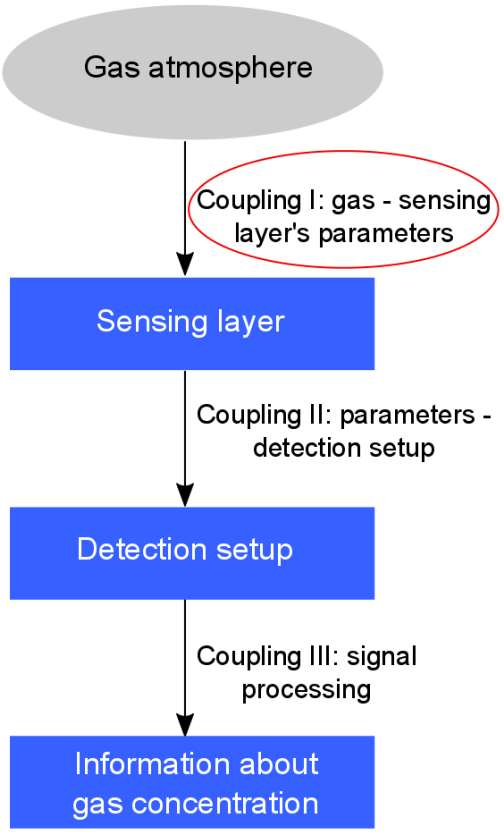

Figure 2.4. The work principle of gas sensors summarized in three couplings - the first coupling is the crucial step in gas sensors design[94]

2.3 Sensing mechanisms: Physisorption and chemisorption

Gas *adsorption* at the surface of solid state is a phenomenon causing an accumulation of gas molecules on that surface. In general, adsorption is an accumulation of substances present in the phase volume on the interface between two phases[95]. The concentration of a gas near the solid state surface at equilibrium is usually higher than in the gas phase volume. The adsorption process occurs as a concentration change of an adsorbed substance on the interface. It depends on properties of both – adsorbing phase (adsorbent) and adsorbed phase (adsorbate). Adsorption should be distinguished from another phenomenon – *absorption* that is a penetration of gas molecules into the solid state volume through diffusion[96]. When adsorption and absorption occur simultaneously, the process is called *sorption*.
Gas adsorption on a solid state is spontaneous process, in which the change in Gibbs free energy of the system is negative. The transition from the free gas to the adsorbed layer reduces the translational freedom of the adsorbate, so also the change in entropy is negative. Therefore, considering following thermodynamic relationship[97]:

$$\Delta G = \Delta H - T\Delta S < 0 \qquad \textbf{2.1}$$

where G is Gibbs free energy, H is enthalpy and S is entropy, the enthalpy of adsorption is negative. Thus, the adsorption is an exothermic process. Adsorbed molecule can leave the surface of an adsorbent in the endothermic process called desorption. The adsorption and desorption processes determine generally the sensing mechanism in the applied sensor structure and are crucial for all parameters of the sensor device, i.e. sensitivity, selectivity, response and recovery times.
Adsorption processes can be divided into two main groups depending on the interaction forces – physical adsorption (*physisorption*) and chemical adsorption (*chemisorption*).
Physisorption is caused by the intermolecular interaction forces. Adsorbate is interacting with the adsorbent surface via van der Waals (vdW) force. It does not take place on all the surface, but only at so called *adsorption sites* (active centers). Amount of adsorbed gas does not increase linearly with increasing adsorbate pressure at the constant temperature. It reaches the saturation level when all adsorption sites are occupied. The adsorption finishes when monomolecular adsorbate layer is formed. Often with the further pressure increase, the amount of adsorbed gas starts to increase again. In this case multimolecular coverage is created – further adsorbate layers are attached to the first layer.
Physical adsorption usually takes place instantaneously and the process is dynamic and reversible. Surface energy plays an important role in the physisorption. In the ideal system with a uniform surface, all the places have the same adsorptive properties and the adsorption process does not need activation and is reduced to the monomolecular adsorbate layer. Adsorbed molecules should not interact with each other. However, the real surface is usually inhomogeneous. This means that the surface energy is also not homogeneous. During the adsorption process, first the sites with higher surface energy are occupied[97,98].
Chemisorption is connected with the electrons transfer between the solid state and a gas and formation of a chemical bonding between them[99]. Chemisorption, in contrary to the

physisorption, requires high activation energy (energy of chemical bonding) and is conditioned by chemical affinity between adsorbent and adsorbate. The chemisorbed molecule interacts mostly with the nearest atom on the surface. Thus, chemical adsorption is restricted to the monomolecular layer. However, when the gas pressure is high enough at moderately low temperature, the further adsorbate layers can be created through physisorption or weak chemisorption. Chemisorption can be either slow or fast. At lower temperatures the process is slow. The gas can be at first physisorbed and then come into chemical reaction with the surface. At low temperatures chemical adsorption can be so slow that practically only physisorption is observed. At higher temperatures physisorption is negligible and only chemisorption is notable. The interaction of the adsorbed molecule with a given surface can be illustrated by a potential energy curve (Figure 3.1). In case of pure physisorption, energy curve is given as a Lennard-Jones potential with a shallow minimum at relatively large distance from the surface, typically $r > 0.3$ nm. Chemisorption process is described by a Morse potential with much deeper minimum at shorter values of r. In general case, chemisorption can be dissociative with dissociation energy D (see Figure 2.5). The physisorption and chemisorption cross at a point of transfer (see Figure 3.1). It can occur above or below the zero-energy line, representing the adsorption activation energy (E_a^{ads}). The process can be either activated or non-activated depending on the exact location of the crossing point. From the energy curve, the energy of adsorption (ΔE_{ads}) and activation energy of reverse process, desorption (E_a^{des}) can be obtained. From the Figure 3.1, the relationship between E_a^{ads}, E_a^{des} and ΔE_{ads} is following[97]:

$$\boldsymbol{E_a^{des} - E_a^{ads} = -\Delta E_{ads}} \qquad \textbf{2.2}$$

Since the activation energy for adsorption is usually much smaller than that for desorption, the following approximation of eq. 2.2 is often applied[97]:

$$\boldsymbol{E_a^{des} \approx -\Delta E_{ads}} \qquad \textbf{2.3}$$

In order to achieve the reversibility of the adsorption process, the energy equal to or higher than E_a^{des} has to be delivered to the system.

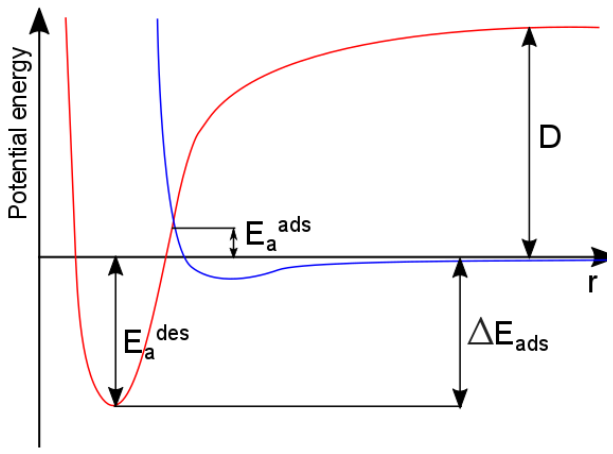

Figure 2.5. Potential energy curve for adsorption process: blue curve represents Lennard-Jones potential for physisorption, red curve represents Morse potential for dissociative chemisorption.

The brief comparison of physisorption and chemisorption characteristics is presented in the Table 2.1.

Table 2.1. The comparison between physisorption and chemisorption

Physisorption	**Chemisorption**
Interaction through weak Van der Waals forces	Interaction through chemical bonding
Low energy of adsorption (2-9 kcal/mol)	High energy of adsorption (>20 kcal/mol)
No activation energy required	High activation energy required
Full reversible	Partially reversible
Fast at low temperature	Slow at low temperature, fast at high temperature
Possible formation of multimolecular adsorbate layers	Phenomenon stabilized at full monomolecular coverage

2.4 Adsorption isotherms

The measured dependence of adsorbed gas amount on pressure and temperature can be plotted as an adsorption isotherm[99]:

$$\boldsymbol{v = f(p)_T} \qquad \textbf{2.4}$$

It describes the amount of adsorbed gas at the constant temperature as a function of the pressure. The shape of adsorption isotherm provides qualitative information about adsorption process and can enable quantitative estimation of a surface covered by an adsorbate.
Several adsorption isotherms have been reported in the literature as useful in the understanding of adsorption process. Brunauer *et al.* in 1945 classified types of isotherms for the systems below the gas critical temperature[100]. However, the three isotherm equations most frequently applied are those derived by Langmuir, by Brunauer, Emmet and Teller (BET) and by Freundlich.
The basic model to calculate the monomolecular adsorption isotherm is the one proposed by Langmuir. It is based on the following assumptions[101]:

1) The adsorbent surface is uniform and the adsorption takes place on the adsorption sites.
2) The adsorption process is dynamic – adsorbate molecules not only cover the adsorbent surface, but also detach.
3) The adsorbent-adsorbate system is in the adsorption equilibrium state.
4) Adsorbed molecules do not interact with each other.
5) The heat of adsorption as well as probability of adsorption is identical at every adsorption site.
6) The value of a heat of adsorption equals the energy of adsorbent crystal lattice vibrations. After the vibrations energy transfer to adsorbed molecules, desorption takes place.

The rate of adsorption on a unit adsorbent surface in the unit time is proportional to:

- surface not covered by adsorbate;
- temperature;
- gas pressure (p).

If S stands for the adsorbent surface covered by adsorbate molecules, the uncovered surface is 1-S. The rate of adsorption can be expressed by the following equation[97]:

$$\boldsymbol{V_A = k_A p(1 - S)} \quad \textbf{2.5}$$

where k_A is a rate of adsorption proportionality factor.
The rate of desorption is proportional to the surface covered by adsorbate (S) as follows[97]:

$$\boldsymbol{V_D = k_D S} \quad \textbf{2.6}$$

where k_D is a rate of desorption proportionality factor.
In the adsorption equilibrium state the rate of adsorption equals the rate of desorption[97]:

$$\boldsymbol{V_A = V_D} \quad \textbf{2.7}$$

$$\boldsymbol{k_A p(1 - S) = k_D S} \quad \textbf{2.8}$$

Solving the Eq. 2.6 one gets the Langmuir isotherm equation[97]:

$$\boldsymbol{S = \frac{k_A p}{k_D + k_A p}} \quad \textbf{2.9}$$

Because only the part of adsorbent surface depending on the number of adsorption sites is active, it has to be assumed that active surface is proportional to the adsorbent mass. The adsorbate mass which is adsorbed for the unit mass of adsorbent (C_A) is proportional to the part of covered surface[97]:

$$\boldsymbol{C_A = k_M S} \quad \textbf{2.10}$$

where k_M is a proportionality factor.
Comparing eq. 2.9 and eq. 2.10, one gets another form of Langmuir isotherm equation[97]:

$$\boldsymbol{C_A = \frac{k_M k_A p}{k_D + k_A p}} \quad \textbf{2.11}$$

The eq. 2.11 can be simplified to the following form[97]:

$$\boldsymbol{C_A = \frac{\alpha p}{1 + \beta p}} \quad \textbf{2.12}$$

where $\alpha = k_M k_A / k_D$ and $\beta = k_A / k_D$.
Langmuir adsorption isotherm can be applied in chemisorption description, since it fulfills the basic assumptions of the model – it is localized. Besides the eq. 2.12, for chemisorption following formula is also used[97]:

$$\boldsymbol{\frac{p}{V} = \frac{1}{b V_M} + \frac{p}{V_M}} \quad \textbf{2.13}$$

where V_M is volume in normal conditions of gas adsorbed at the site of monomolecular layer creation, V is a respective adsorbate volume at the pressure p and b is a ratio of condensation and evaporation rates of adsorbed gas.
The Langmuir adsorption isotherm is presented in the Figure 2.6. As one can observe, with increasing pressure (p), the amount of adsorbed substance (C_A) grows until the saturation level, which is a state of equilibrium between adsorption and desorption.
Langmuir adsorption isotherm is a base for other isotherms. One of the most used is Freundlich isotherm (Figure 2.6). Its equation has a following form[97]:

$$C_A = \text{const} \cdot p^{1/n} \qquad 2.14$$

The value of n in the exponent is usually higher than 1, so the function of C_A in terms of p is convex. In contrary to the Langmuir isotherm it is not linear for low pressures and it does not saturate at high pressure.
The Langmuir isotherm is well applicable in the situation of low coverage, but it fails at high adsorbate pressure, thus high coverage. S. Brunauer, P.H. Emmet and E. Teller adapted the Langmuir's model to describe multimolecular adsorption process. They derived the equation called BET equation[102]:

$$V = \frac{V_M k_M p}{(p_S - p)\cdot\left[1+\frac{(k_E-1)p}{p_S}\right]} \qquad 2.15$$

where V is a volume of adsorbed gas at the pressure p, p_S is a pressure of saturated adsorbate vapor, V_M is a volume of adsorbate required to form monomolecular adsorbate layer on the whole adsorbent surface and k_E is an energetic constant. Energetic constant k_E approximately equals in the temperature T[102]:

$$k_E = e^{\frac{q_p - q_s}{RT}} \qquad 2.16$$

where q_p is a heat of monomolecular layer adsorption, q_s a heat of condensation and R is a universal gas constant.
The derivation of BET model is based on the balance of the rates of evaporation and condensation for the various adsorbed molecular layers and on the assumption that a characteristic heat of adsorption applies for the first monolayer, while the heat of condensation applies to adsorption in the second and subsequent molecular layers (Figure 2.6).
BET equation is applied to determine the surface covered by the adsorbate and the specific surface area of adsorbent.

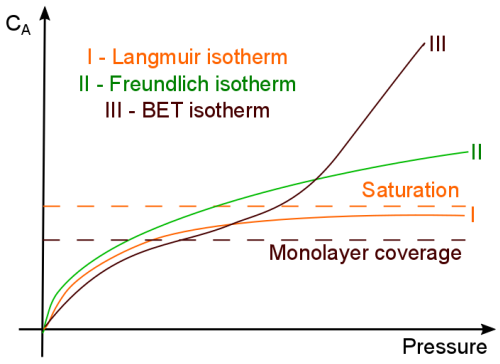

Figure 2.6. Adsorption isotherms: Langmuir (I – blue line), Freundlich (II – green line) and BET (III – red line) adsorption isotherms: C_A is the adsorbate mass adsorbed for the unit mass of adsorbent (coverage); orange dashed line shows the saturation coverage for Langmuir adsorption model, brown dashed line indicates monolayer coverage for BET model of multilayer adsorption

2.5 Gas adsorption on semiconductor's surface

To understand better the influence of gas adsorption on a semiconductor electrical properties, one has to be familiar with a work function (WF) concept. Since the local vacuum level (E_{VAC}) is a central of the WF definition, it will be explained first. The E_{VAC} is defined as the energy level of an electron position at rest at the distance of "few nanometers" from the solid surface[103]. The "few nanometers" distance corresponds to a distance short enough for electron to experience the full impact of the surface electrostatic field. In the semiconductor the electrons closest in energy to E_{VAC} are those at the valence band maximum (E_V) or HOMO level. The energy difference between E_{VAC} and this level known as the ionization energy (IE) is the minimum energy necessary to remove an electron from the system. The energy gained by dropping an electron from the vacuum level to the lowest unoccupied state (E_C or LUMO), is the electron affinity (EA) of the solid. Typical inorganic and organic semiconductors have EAs and IEs in the range of 2–4 eV and 4.5–6.5 eV, respectively[103]. The parameter of a biggest importance for gas sensors is a WF which is defined as the energy necessary to remove an electron from the Fermi level and place it at E_{VAC} [103]. In a metal, E_F is placed at the boundary between occupied and unoccupied states making IE and EA equal to the WF of the material. In a non-degenerate semiconductor there are generally no electrons at the Fermi level and WF in these materials is a statistical value between IE and EA. In a semiconductor, WF directly depends on the position of E_{VAC} and on E_F, which depends on the density of states, temperature, carrier density and doping concentration in the material. WF is determined quantitatively *via* PE, which provides absolute measurements of both E_F and E_{VAC} positions. The WF (Φ) of semiconductor consists of three contributions: the difference between the Fermi level (E_F) and the conduction band (E_C) in the bulk $(E_C\text{-}E_F)_b$, band bending eV_S and EA (χ) (Figure 2.7)[104]:

$$\boldsymbol{\Phi = (E_C - E_F)_b + eV_S + \chi} \qquad \textbf{2.17}$$

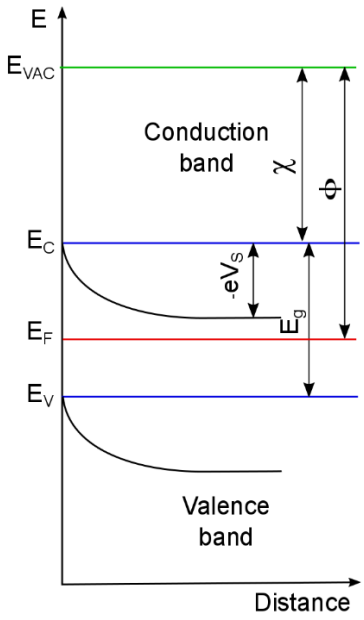

Figure 2.7. WF (Φ) of semiconductor consists of three contributions: the difference between the Fermi level (E_F) and the conduction band (E_C) in the bulk $(E_C\text{-}E_F)_b$, band bending (eV_S) and electron affinity (χ).

Gas adsorption process can change semiconductor work function by influencing all three of its components (eq. 2.17). If we assume that gas adsorption at the surface does not affect the difference between Fermi level and conduction band in the bulk, changes in work function are expressed then by following equation[105]:

$$\Delta\boldsymbol{\varphi} = \Delta\chi + \boldsymbol{e\Delta V_S} \qquad \textbf{2.18}$$

In order to understand the influence of adsorbed species on work function components, one can distinguish between "neutral and "charged" adsorbed molecules. The "charged" species are ionsorbed (strongly chemisorbed) species that have influence on band bending and electrical conductivity. They undergo delocalized charge transfer with the semiconductor – the counter charge of ionized adsorbate at the surface is delocalized within a depletion layer in the semiconductor and thus changes the concentration of free charge carriers in the conduction band. The species that do not influence the electrical conductivity of semiconductor ("neutral" species – weak chemisorbed or physisorbed) undergo localized charge transfer. This localized charge transfer is equivalent to the creation of a surface dipole that causes a potential drop across the electric double layer formed by the adsorbed molecule and the surface. The latter influences the electron affinity of a semiconductor.
In order to calculate change in electron affinity one can describe the dipolar layer formed on the surface of the sensor as parallel capacitor[104] for which potential difference can be written as:

$$\boldsymbol{V_{dip}} = \frac{\sigma}{\boldsymbol{C_{dip}}} = \frac{\sigma \cdot \boldsymbol{d}}{\boldsymbol{\varepsilon_0 \varepsilon_r}} \qquad \textbf{2.19}$$

where σ is polarization superficial charge density, C_{dip} is capacity of the layer, ε_0 is vacuum electrical permittivity, ε_r relative permittivity of the material and d is a diameter of gas molecule. Charge density can be obtained from the relation between σ and the component of the polarization perpendicular to the surface P_n:

$$\boldsymbol{\sigma = P_n} \qquad \textbf{2.20}$$

Polarization P_n is defined as dipolar momentum of the unit volume:

$$\boldsymbol{P_n} = \frac{\boldsymbol{N \cdot p_n}}{\boldsymbol{V}} = \frac{\boldsymbol{p_n}}{\boldsymbol{d^3}} \qquad \textbf{2.21}$$

where N is number of dipoles in the volume V and p_n is normal dipolar momentum of the adsorbate layer.
From eq. 2.19-2.21 we obtain:

$$\boldsymbol{V_{dip}} = \frac{\boldsymbol{p_n}}{\boldsymbol{\varepsilon_0 \varepsilon_r \cdot d^2}} \qquad \textbf{2.22}$$

Since band bending eV_s is linked with the surface conductivity G by Morrison's equation, its change can be calculated from the resistance changes in the presence of detected gas. The conductivity of the structure is expressed as[106]:

$$\boldsymbol{G = G_0 \exp(-\frac{eV_s}{kT})} \qquad \textbf{2.23}$$

where k is Boltzmann constant, T – temperature, V_S is the surface potential and G_0 includes the bulk intergranular conductance and geometrical effects. Hence, change of band bending $e\Delta V_s$ can be obtained from the following equations:

$$G_a = G_0 \exp\left(-\frac{eV_{sa}}{kT}\right) \quad 2.24$$

$$G_g = G_0 \exp\left(-\frac{eV_{sg}}{kT}\right) \quad 2.25$$

where G_a and G_g are conductivities in the air and in the studied gas respectively, V_{sa} and V_{sg} are surface potentials in the air and after adsorption of the gas respectively. After dividing eq. 2.25 per eq. 2.24 and considering that $G_a/G_g=R_g/R_a$ (where R_a and R_g stand for the resistance in the air and in the studied gas correspondingly) we get:

$$e\Delta V_s = kT \ln\left(\frac{R_g}{R_a}\right) \quad 2.26$$

The eq. 2.24 and eq. 2.25 were dedicated for the thick-film gas sensor model[106]. One of the main parameters distinguishing the thin and thick layer in the sense of electronic processes, including the interaction with adsorbate on the surface, is the Debye length (L_D) - distance, in which charge carriers electrostatic effect persists. Debye length is expressed by the following equation[106]:

$$L_D = \sqrt{\frac{\varepsilon_0 kT}{e^2 n_p}} \quad 2.27$$

where n_p is a major charge carriers concentration.
Thus, the latter equation can be applied for the sensor structures that in terms of electronic behaviour possess attributes of thick film – the thickness is relatively high with respect to the Debye length.
Figure 2.8 illustrates the changes in WF of n-type semiconductor undergoing both chemisorption and physisorption processes.

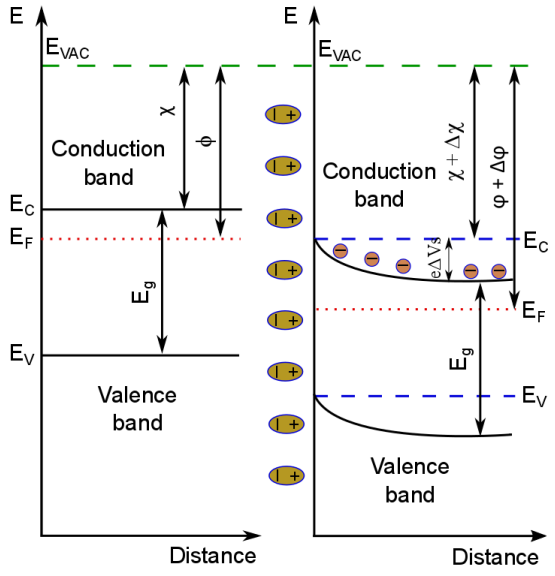

Figure 2.8. The work function changes ($\Delta\varphi$) in n-type semiconductor undergoing both chemisorption and physisorption processes – see text

3 Materials for DMMP sensors

3.1 Semiconductor metal oxides for gas sensors

SMOs is one of the most investigated groups of materials for gas sensors. They have attracted big attention because of their low cost, simplicity of use, flexibility in production and a high number of detectable gases. In 1953 it was demonstrated for Ge that electrical resistance of a semiconductor is sensitive to the impurities in its volume and at the surface[107]. Later the sensitivity of ZnO thin films heated to 300 ºC to reactive gases in the air has been reported[108]. Finally similar properties, but with higher stability were shown for SnO_2[109]. It initiated a development of commercial gas sensors, i.e. FIGARO devices.
The principle of SMO sensors is based on the change in electrical conductance during interaction with the gas molecules. Metal oxides for gas sensors should be selected due to their electronic structure. The early metal oxide-based sensors possessed undesirable characteristics, like slow sensor response, cross-selectivity, long-term signal drift and slow response time[110]. Since then various SMOs have been tested in order to find the materials with appropriate characteristics[53, 111]. The most popular sensing materials among n-type SMOs are SnO_2, ZnO, TiO_2 and WO_3 [112]. The p-type SMOs mostly used are NiO and CoO[110]. The operation principle of SMO based sensors in the nutshell is as follows: trapping of electrons at adsorbed gas molecules and band bending induced by these charged molecules cause the change in electrical conductivity. This mechanism was explained in detail in the Chapter 2.
In the fabrication of metal oxide gas sensors both – thick film and thin film techniques are applied. The SMO films are deposited by screen printing, spin coating, RF sputtering or chemical vapour deposition[113]. The most used substrates are glass, silicon, alumina or ceramic[53,110]. In order to collect electrical signal, gold, platinum, silver or aluminium electrodes are deposited on the substrate in various designs, among which the most common is interdigitated electrodes (IDE) structure[53,110]. The property of detection reaction that occurs in SMO is that they require high level of thermal activation[114]. The typical operation temperatures of this type of devices are in the range of 200-500 ºC[53]. In order to provide the high temperature, heating elements are printed on the back of the substrate. Heater substrates are high-power consuming, what is the biggest disadvantage of gas sensors based on SMOs.
There are several factors influencing the sensor properties of metal oxide sensing films, among which the main are[115,110]:

- chemical composition;
- surface modification by noble metal particles;
- microstructure;
- film thickness – thinner films are more sensitive to gases[116];
- temperature.

Chemical composition is an important factor since different metal oxides are favorable in some of gas sensor properties, but very few of them are suitable to all requirements. Because of this,

the research had focused on composite materials, like SnO_2-ZnO[117, 118], ZnO-CuO[119], Fe_2O_3-ZnO[120]. The numerous ternary, quaternary and complex metal oxides are also of interest[121,122]. The combination of metal oxides with other components, i.e. organic semiconductors and carbon nanotubes has been also widely investigated[123,124,125,126.]

Conductivity response of many gas sensors can be determined by the efficiency of catalytic reactions with detected gas on the surface of sensing material. Therefore, in order to improve the performance of gas sensor, catalytic activity of sensing material can be controlled. Since the catalytic activity of widely used SMOs is poor[127], *noble metals* are used as catalyst. There have been many papers reporting enhancement of sensitivity by applying noble metals such as Pt, Pd, Au, Ag[128, 129, 130, 131, 132, 133, 134, 135,136, 137, 138].

Another factor influencing sensitivity and selectivity is *microstructure*. Because the performance of solid-state gas sensors is determined by both, receptor and transducer functions, it is important to synthesize metal oxides with optimal morphology and crystallographic structure. The grain size of the oxide affects sensitivity as well as selectivity to particular gases[53]. Sensitivity can be increased using metal oxides with small grain sizes and narrow necks. This is because when the grain size is less than twice the thickness of surface charge layer, the grain is fully involved in the space-charge layer[139].

The last factor playing important role in the gas sensor performance is *operating temperature*. The typical dependence of a metal oxide sensor response has a bell-like shape with a maximum at a certain temperature[140]. This dependence arises due to the following reasons:

- the charge of oxygen species adsorbed at the oxide's surface depends on temperature[141];
- the oxidation reaction rate increases with temperature;
- all adsorption, desorption and diffusion processes are temperature-dependent[142].

Thus, temperature modulation leads to the response patterns characteristic for the species that are present in the gas mixture[143]. The operating temperature is determined by the operating mechanism of the material – surface conductance or bulk conductance. The oxides following surface electric conductance effects operate at lower temperatures (400 - 600 ^oC) and those following bulk electric conductance effects operate at high temperatures (>700 ^oC)[144]. The most common materials following surface electric conductance effects are ZnO and SnO_2[144].

3.2 Organic semiconductors for gas sensors

In the previous section it was mentioned that since the characteristics of gas sensors based on metal oxides were not satisfying, the investigation had focused on improving them by different modifications. However, in the same time researchers have been studying organic semiconductors as potential materials for chemoresistive sensors. The big advantage of organic semiconductors is that they do not interact as strongly with oxygen and water as inorganic semiconductors and they can be easily modified chemically, so they can be applied to produce devices with high selectivity and operable at lower temperature[145]. Within the class of organic chemoresistive sensors, there are several materials used for the sensing layers: organic conjugated polymers and polymer composites, carbon nanotubes and Pcs.

Conjugated polymers gained a big interest in the field of gas sensors because of their synthetic flexibility that allows tailoring the chemical and physical properties over a broad range of values. They also exhibit tunable selectivity to volatile organic compounds. Their main advantages as gas sensors are easy and low-cost fabrication, ability to operate at room temperature and fast response and recovery times. Their disadvantages are variability from sensor to sensor and sensitivity to the humidity. The latest trends in polymer chemiresistors research are focused on the fabrication of nanostructures (nanowires, nanotubes and nanofibres) and combination of metal oxide nanostructures with polymer films.
Carbon nanotubes gained interest in gas sensors research because of their unique electrical and mechanical properties, such as: large surface area to volume ratio[145], big sensitivity of electrical properties to the effects of charge transfer and chemical doping, ease of functionalization. Since carbon nanotubes are not sensitive to many organic vapors, especially nonpolar molecules, they have to be functionalized with polymer coatings or palladium films[6, 146]. Their main advantages are low work temperature and good reversibility. The weakness of this sensing material is inability to selectively grow semiconducting nanotubes and the complex techniques required to handle single nanotubes.
Phthalocyanines are macrocyclic planar molecules which spontaneously arrange as linear stacks which form semiconducting crystals. Solid phthalocyanines acts as *p*-type semiconductor with hole conduction. They are widely applied semiconducting organic small molecules. Both – metal-free and metallo-phthalocyanines have been widely studied in a field of gas sensors[18,19,20,21,22,147,148]. They are good sensitive materials because of their thermal and chemical stability and range of electrical conductivity changes in a presence of oxidizing or reducing gases[149,150]. Phthalocyanines in the air are stable even up to 400-500 ºC and in the vacuum most of complexes do not decompose[150]. The electrical conductivity of phthalocyanines changes in the presence of gases, because adsorption of electron-withdrawing or donating molecules causes charge transfer. The studies have shown that the ability of phthalocyanines to sense gases can be affected by several factors, such as: film morphology and thickness, work temperature and post-deposition annealing.

3.3 Inorganic and organic semiconductors investigated in DMMP detection

In the last two decades a lot of research has been conducted in the field of nerve agents simulants, especially DMMP sensors. Various techniques were utilized for the detection of nerve agents, including conductometry, quartz crystal microbalance or surface acoustic wave setups, etc. using wide range of materials[2,4,5,6,7,8,9,10,11,12,13,151,152,153,154,155,156].
Among semiconducting oxides, following compounds have been tested as potential DMMP sensors: SnO_2, ZnO, WO_3, In_2O_3, CuO, Y_2O_3, MnO_2 TiO_2 and graphene oxide[11,12,13,151,152,153,154,155,156]. Tomchenko *et al.*[152] investigated a group of thick-film nanocrystalline metal oxides (SnO_2, WO_3, In_2O_3, CuO and Y_2O_3) in DMMP and diethylchlorophosphate (DCP) detection. The studied materials showed positive characteristics in terms of sensitivity, stability and response time. They compered the results of simulants

detection with those for real nerve agents. Sensors reliably detected sarin, soman and mustard gas from 10 ppb and higher. However, examined sensors possessed big disadvantages like high work temperatures (200-400 ºC) and lack of selectivity. In order to achieve selectivity, they needed to be combined in a sensor array. Brunol *et al.*[73] focused on explaining the reaction mechanism in DMMP detection by SnO_2 sensor. They studied the sensor response for a relatively high concentration of DMMP vapour (200 ppm). The main conclusion regarding the sensor properties was that after the thermal degradation of DMMP, phosphorus compounds progressively pollute SnO_2 surface and induce a response drift versus time. Other researchers introduced various modifications of metal oxides in order to improve their performance in DMMP detection. Kanan *et al.*[12] proposed the application of dual WO_3 based sensors to selectively detect DMMP in the presence of alcohols. They used the approach in which they compare the response of WO_3 films with different porosity. Ran Yoo *et al.*[11] presented Al-doped ZnO nanoparticles as a fast and selective DMMP sensor. They achieved significant decrease of response time compared to ZnO nanoparticles without doping (2 s in respect to 96 s for 10 ppm). However, the work temperature of described sensor was high (350 ºC). Soo Chool Lee *et al.*[13] applied catalysts, such as Mo, Sb and Ni to improve SnO_2 performance in DMMP sensing. Their device exhibited high sensitivity to ppb levels of DMMP and reversibility. As the most metal oxide based detectors, it required high operating temperature.

The big part of the research focused on organic DMMP sensors. Hydrogen-bond acidic polymers and phthalocyanines are of particular importance for the detection of nerve agents[2,3,9,10,23,30,31,32]. DMMP, as a Lewis base with relatively high dipole moment interacts through hydrogen-bond or weak polarization interactions with that type of materials[2]. This kind of sensor response mechanism is desirable regarding low work temperature and reversibility – for the weaker interaction, the lower activation temperature is required and desorption of detected molecules is faster. Organic materials have been tested for DMMP detection by conductometric as well as acoustic methods (surface acoustic wave and quartz crystal microbalance). As it was mentioned in the previous section, phthalocyanines have been widely investigated for many years in the field of gas sensors. Their properties are already well recognized. Because of this, they gained an attention also in DMMP detection. The use of phthalocyanines for DMMP detection has been first reported in the 1980s. Temofonte and Schoch[157] observed the sensor response of NiPc to 6.7 ppb of DMMP at the room temperature. Later Bohrer *et al.*[2] reported the sensitivity of phthalocyanines, especially metal-free phthalocyanine (H_2Pc) in their paper that compared reactivity of various phthalocyanines with different Lewis bases, including DMMP. In the last decade, few papers concerning DMMP detection by phthalocyanine sensing layers have been published[31,32,158,159]. They focused mostly on the modification of Pc chemical composition or its combination with other organic materials in order to achieve high sensitivity and selectivity. Tasaltin *et al.*[32] presented approach, in which they synthesized NiPc and ZnPc with fluorinated alkyl and aryl oxy substituents. Those substituents increase affinity for polar compounds, such as DMMP.

Another group of organic materials widely investigated in DMMP sensing are carbon nanotubes[4,5,6]. When combined with other materials, e.g. polyaniline[6], they exhibit high and fast response and reversibility in the room temperature. This kind of sensing structure was tested only for ppm levels of DMMP. Novak *et al.*[4] observed high sensitivity to DMMP of thin-film transistors constructed from random networks of single-walled carbon nanotubes. Their sensors

were reversible and capable of detecting DMMP at sub-ppb concentration levels. They were also selective against hydrocarbon vapors and humidity. However, in order to achieve further chemical specificity, chemoselective polymers had to be used.

3.4 Semiconductor metal oxides-DMMP interaction mechanism

There are several papers concerning mechanism of DMMP reaction with semiconductive metal oxides, such as TiO_2[35,36,37,38,39,40,41], WO_3[35,38], ZnO[35,50], MgO[35,42,43], Al_2O_3[35,43,44], Fe_2O_3[88,44,45], SiO_2[46], Y_2O_3[47], CeO_2[160], La_2O_3[89], MoO_x[49,51], SnO_2[73]. These studies revealed that DMMP at room temperature binds primarily to Lewis acid metal sites of the oxide (i. e. an under-coordinated metal atom) through the phosphoryl oxygen[37,39,42]. Hydroxyl groups on the surface are the second favored binding site[38]. The main decomposition mechanism of DMMP is breaking of P-OCH_3 bond through an electrophilic or nucleophilic attack[161]. The main products of this decomposition at room temperature are methanol, dimethyl ether and surface metoxy groups. The decomposition of DMMP on metal oxide surface at elevated temperatures results in additional products such as methane, carbon dioxide, carbon monoxide, formaldehyde and hydrogen[45,162,163].

Kim *et al.*[38] investigated interaction of organophosphorus compounds, including DMMP with TiO_2 and WO_3 surfaces probed by vibrational spectroscopy. They found that at room temperature DMMP is adsorbed on the metal oxide surface through hydrogen bonds between the P=O functional group and the hydroxyl groups of metal oxide surface (Figure 3.1).

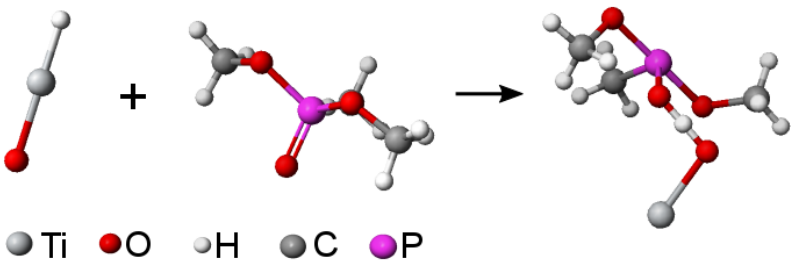

Figure 3.1. DMMP adsorption at room temperature on the metal oxide (here TiO_2) described by Kim *et al.*[38]. At room temperature DMMP is adsorbed on the metal oxide surface through hydrogen bonding of the P=O functional group to the hydroxyl groups of metal oxide surface

At higher temperatures organophosphorus compounds dissociate and form covalently attached species. Decomposition takes place above 200 ºC, by first losing a methoxy group and then the second one above 300 ºC when a stable phosphate surface complex is formed. It can cause poisoning of the sensor film operating in this temperature. The mechanism of sensor electrical conductivity change in case of chemisorbed species at higher temperatures can be described by the simplest model for SMO sensor response to reducing gas[38]:

$$\frac{1}{2}O_2 + 2e^- \leftrightarrow O_{ads}^{2-} \qquad \textbf{3.1a}$$

$$R + O^{2-} \leftrightarrow RO_n + 2ne^- \qquad \textbf{3.1b}$$

where R is the detected gas and RO_n is the oxidized product.

First, the atmospheric oxygen thermally dissociates at the semiconductor surface and is adsorbed as atomic ions by trapping conduction electrons from the solid. Next, reducing gas can undergo catalytic oxidation, removing the ad-oxygen and releasing the captured electron back to the conduction band. During multiple exposures to the target gas, the oxidized product should be liberated to the carrier gas stream in order to provide consistency in the sensor performance.

Brunol *et al.*[73] studied thermal decomposition of DMMP and its interaction with SnO_2. They proposed reaction mechanism based on their investigation and on results of other authors[37,43,44164,165]. They observed that DMMP at temperatures from 300 ºC to 600 ºC decopmoses into two compounds: carbon dioxide and methylphosphonic acid. Thus, the DMMP sensor is solely exposed to CO_2 and methylphosphonic acid. It is well recognized that SnO_2 based gas sensors exhibit low sensitivity to this compound. Hence, it indicates that electrical response to DMMP vapour is principally due to the interaction of phosphorus compounds with the sensor. This hypothesis is in agreement with Kim *et al*[38]. The reaction mechanism responsible for increase in SnO_2 conductance in the presence of DMMP takes place in two stages. First, DMMP adsorbed onto SnO_2 surface reacts with oxygen species (O^-). As a consequence of this reaction, methylphosphonic acid and CO_2 and H_2O are formed. Methylphosphonic acid remains adsorbed onto SnO_2, while CO_2 does not react with the sensor material. At the same time electron is released to the SnO_2 conduction band, leading to an increase in the electrical conductance. This mechanism can be summarized by the following equation:

$$\mathbf{SnO_2 + DMMP \rightarrow [DMMP]_{ads} + 6O^- \rightarrow SnO_2 + [methylphosphonic\ acid]_{ads} + 2CO_2 \uparrow + 2H_2O \uparrow + 6e^-} \quad \mathbf{3.2}$$

Finally, an ionic phosphorus compound irreversibly adsorbed onto SnO_2 surface is formed.

The reaction mechanism described above can be generalized for other metal oxide semiconductors. In case of *p*-type semiconductors (e.g. PdO) electron release would lead to decrease in the electric conductivity.

3.5 Organic semiconductors-DMMP interaction mechanism

The sensing mechanisms in organic semiconductors are quite different than those in SMOs. Due to large molecules with different side chains or termination radicals, the organic semiconductors interaction with gases is more complex.

As described above, SMO sensors rely mostly on redox reactions. Most of organic sensors interaction with gases is rather based on weak intermolecular forces, as van der Waals forces and π stacking, polarizability and hydrogen-bond basicity and acidity[166,167]. Hierlemann *et al.* probed these intermolecular interactions directly by Fourier-transform infrared spectroscopy[168]. In case of MPcs, metal coordinative bonds are potentially the strongest binding sites for Lewis bases adsorption[169]. Strong electron donors can bind either directly to the metal centers or compete with O_2 if the binding site is occupied by O_2 species[2]. Weak electron donors can

physisorb on the organic Pc ring through vdW forces and polarization interactions[2]. The interaction of MPcs (mostly of p-type conductivity) with different oxidizing gases, e.g. O_2, NO_x, O_3, has been found to lead to a conductivity attributed to a redox reaction[157,170]. In contrast, the MPc interaction with reducing gases has been reported to decrease the conductivity due to hole trapping by chemisorbed agent donated electrons[171]. Bohrer *et al.*[2] related the adsorption enthalpies with different MPcs (CoPc, CuPc, ZnPc and NiPc) to the sensitivity expressed by film electric conductivity changes and found the exponential relation between the sensitivity and the binding enthalpy of various reducing agents, including DMMP. The low sensor response to weak electron donors was attributed to the low availability of the strongest adsorption sites, e.g. metal centers, due to the oxygen adsorption from ambience. However, there are other conceivable factors which might be responsible, such as the orientation of the Pc molecules within the sensing layer. There are, for example, more surface adsorption sites available for well-ordered horizontally-aligned structures compared to vertical molecular orientations. The realization of specific film morphologies, however, requires control of various experimental conditions such as the substrate, the deposition technique, the deposition temperature and pressure[172,173,174,175,176].

Also there is a number of theoretical studies available on molecular adsorption on phthalocyanines[33,34]. However, previous gas sensors modeling was limited to single-molecule interactions. It also did not take into account the charge redistribution upon the gas adsorption that is one of the most important factors in gas sensors design, since it determines the measurable changes in the sensing material's electronic structure. Moreover, the combination of theoretical approach with experimental techniques such as photoelectron spectroscopy or TDS is missing in the literature. For this reason in the next chapters, the proposed methods to investigate sensing mechanisms in general are described. In this thesis they were applied for the study of DMMP adsorption on phthalocyanines and hybrid structures based on phthalocyanines.

4 Methodology

4.1 Theoretical methods

The theoretical study of molecules adsorption on surfaces requires solving the many-body Schrödinger equation which in most cases is too complex to allow the exact solution. Hence, a lot of computer-aided quantum chemical models starting from Hartree-Fock (HF) approximation were developed to solve the many-body problem[177]. All methods obtained from HF approximation have severe limitations since they are based on the multi-dimensional wave function $\Psi(r_1,r_2,\ldots,r_N)$, where N is number of electrons in the studied system. The computation effort increases exponentially with the number of electrons. These methods are thus limited to problems with small number of chemically active electrons.
Density functional theory (DFT) proposed in 1964 by Hohenberg and Kohn[178] is a particular methodology that deals with this problem. Its basic idea is the shift from the multi-dimensional wave function to the three-dimensional ground-state density $n(r)$ as a main variable. DFT became a basic approach for obtaining ground-state properties in solid-state physics and surface science.

4.1.1 Semi-empirical methods

Most semi-empirical methods in computational chemistry are based on molecular orbital (MO) theory and use of HF formalism for MO determination. The HF is based on the variational principle which says that calculated approximate energies are equal to or greater than the exact energy. It assumes that the exact wave function for *N*-electron system can be approximated by a single determinant (Slater determinant) of the matrix built form the functions depending on individual electrons coordinates (spinorbitals). The primary approximation in HF method is a central field approximation that excludes electron-electron repulsion in the calculation, taking into account only its net effect. The second approximation is that the wave function is described by some functional form known exactly only for few one-electron systems. The most often used functions are linear combinations of Slater type orbitals (STO) or Gaussian type orbitals (GTO)[179]. The wave function is formed from the linear combination of atomic orbitals or basis functions.
Semi-empirical methods are simplified versions of HF theory that apply empirical corrections in order to improve performance. Within the HF method some pieces of information, like two-electron integrals are approximated or omitted. In semi-empirical calculations the parametrization is used in order to correct the errors introduced by omitting the part of information. This parametrization is made in the way to give results that agree with the experimental data. The advantage of semi-empirical calculations is that they are much faster than ab initio HF calculations. The disadvantage of semi-empirical methods is that they can be used only for the molecules similar to those used for the parametrization and they require

reliable experimental or theoretical data. Another limitation is a different accuracy of semi-empirical results for different classes of compounds. Sometimes a different parametrizations of a given semi-empirical model are required for different properties to obtain good accuracy.
Semi-empirical methods apply three schemes of approximation: (1) the elimination of core electrons from the calculation, (2) the use of minimum number of basis sets, (3) the reduction of the number of two-electron integrals. Within the scheme (3), all modern semi-empirical methods are based on the neglect of differential diatomic overlap (NNDO) approach. In this method the parametrization was carried out for different atomic types and parameters were fitted to reproduce heats of formation, geometrical variables, first ionization energies and dipole moments. The most often used methods within NNDO approach are: MNDO (Modified Neglect of Differential Overlap)[180,181], AM1 (Austin Model 1)[182], PM3 (Parametric Model number 3)[183, 184, 185, 186], PM6 (Parametric Model number 6)[187]. In this thesis one of the most recent semi-empirical methods, PM6 is used. The PM6 approach introduced several modifications to the NDDO core-core interaction term and to the method of parameter optimization. As a result of these changes, more complete parameter optimization has been achieved. It allowed more than 80 elements, including transition metals to be parametrized. However, using PM6 method one has to remember that in its basic form it fails for the description of nonconvalent interactions, such as dispersion interactions and H-bonding[188].

Technical description of performed semi-empirical calculations

All semi-empirical calculations were performed using PM6 with the MO-G for SCIGRESS program (version FJ 2.8 EU 3.2.2.). The simulations were carried out for one molecule of phthalocyanine, palladium cluster and palladium oxide cluster[189] with one DMMP molecule. All initial structures were optimized at first by PM6 method. The adsorption of DMMP molecule on sensing materials and dipole moments of all structures were determined.

4.1.2 Density functional theory

Kohn-Sahm equations

The basis for all quantum chemistry methods is the time-independent non-relativistic Schrodinger equation describing many-electron wave function Ψ:

$$\boldsymbol{E\Psi = T\Psi + V\Psi + V_{ext}\Psi} \qquad \textbf{4.1}$$

where T is kinetic energy operator, V is electron-electron interaction potential and V_{ext} represents external potential that includes Coulomb interaction with nuclei[190]. Above equation contains Born-Oppenheimer approximation assumes the large mismatch between the mass of electron and nucleus. Thus electrons move much faster than nuclei and adapt to the movements of the ions. By this assumption electrons and nuclei degrees of freedom are separated. The many-body problem is first solved for the fixed positions of ions. Then ions positions are optimized by solving electronic many-body problem. Ionic positions become only parameters in the eq. 4.1.

Hohenberg and Kohn proved unique relations between ground-state charge density and corresponding wave function and external potential (first Hohenberg-Kohn theorem):

$$\boldsymbol{n}(\mathbf{r}) \rightarrow |\boldsymbol{\Psi}[\boldsymbol{n}]\rangle\,, \qquad \text{and} \qquad \boldsymbol{n}(\mathbf{r}) \rightarrow \boldsymbol{V_{ext}}(\mathbf{r}) \tag{4.2}$$

The second Hohenberg-Kohn theorem states that the ground state density n_0 minimizes the total energy of the system, resulting in the ground state energy E_0. It makes DFT a primarily ground state theory. Ground-state solution of the Schrodinger equation can be obtained from the variational principle by minimizing the energy with respect to a trial wave function and the charge density:

$$\boldsymbol{E_0} = \min_{\boldsymbol{\Psi}} \langle \boldsymbol{\Psi} | \boldsymbol{T} + \boldsymbol{V} + \boldsymbol{V_{ext}} | \boldsymbol{\Psi} \rangle = \min_{\boldsymbol{n}(\mathbf{r})} \boldsymbol{E}[\boldsymbol{n}(\mathbf{r})], \tag{4.3}$$

where

$$\boldsymbol{E}[\boldsymbol{n}] = \boldsymbol{T}[\boldsymbol{n}] + \boldsymbol{V_H}[\boldsymbol{n}] + \boldsymbol{E_{xc}}[\boldsymbol{n}] + \boldsymbol{V_{ext}}[\boldsymbol{n}] \tag{4.4}$$

$T_S[n]$ is a kinetic energy functional for non-interacting electrons, $V_H[n(\mathbf{r})]$ stands for the functional of the classical Coulomb interaction energy, $V_{ext}[n]$ is the external potential functional. All non-trivial many-body effects are combined into exchange-correlation functional $E_{xc}[n]$. Exchange-correlation potential determines accuracy of DFT calculations, since it needs to be approximated.

To solve the eq. 4.3 one can write the charge density as a sum of single-particle states:

$$\boldsymbol{n}(\mathbf{r}) = \sum_{\boldsymbol{i=1}}^{\boldsymbol{N}} |\boldsymbol{\varphi_i}(\mathbf{r})|^2, \tag{4.5}$$

where N is the total number of electrons.

Applying above expression and minimizing eq. 4.3 under constraint that all $\varphi_i(\mathbf{r})$ are normalized and orthogonal, one obtains the set of Kohn-Sahm equations[191]:

$$\left[-\frac{\hbar^2}{\boldsymbol{2m}}\boldsymbol{\nabla^2} + \boldsymbol{V_{eff}}(\mathbf{r})\right]\boldsymbol{\varphi_i}(\mathbf{r}) = \boldsymbol{\varepsilon_i}\boldsymbol{\varphi_i}(\mathbf{r}), \tag{4.6}$$

The effective potential, V_{eff} is expressed by:

$$\boldsymbol{V_{eff}}(\mathbf{r}) = \boldsymbol{V_H}(\mathbf{r}) + \boldsymbol{V_{xc}}(\mathbf{r}) + \boldsymbol{V_{ext}}(\mathbf{r}), \tag{4.7}$$

where V_{xc} is the functional derivative of exchange-correlation functional.

In order to solve the set of coupled equations, the self-consistent method is applied. Kohn-Sahm equations are first solved from an initially guessed electron density. V_H and V_{xc} are computed using this initial guess. In the next step new density obtained from the previous step is mixed with the old one and Kohn-Sahm equations are solved again. This procedure is repeated until the converged charge density is obtained.

Exchange-correlation functionals

To solve Kohn-Sahm equations, the correct exchange-correlation functionals are required. This functional is not currently known in an exact analytic form. Its simplest representation is the local density approximation (LDA), by which the energy functional is expressed as[192]:

$$\boldsymbol{E_{xc}^{LDA}}[\boldsymbol{n}] = \int \boldsymbol{n}(\mathbf{r}) \cdot \boldsymbol{\varepsilon_{xc}}(\boldsymbol{n}(\mathbf{r})) \cdot \boldsymbol{d}\mathbf{r}, \tag{4.8}$$

where $\varepsilon_{xc}(n(\mathbf{r}))$ is exchange-correlation energy per particle in a homogenous electron gas with a density equal to the density at the position **r**. The exchange-correlation energy can be obtained from quantum Monte Carlo calculations performed for the homogenous electron gas[193]. The LDA provides good results for lattice constants and geometrical configurations, but it often overestimates molecular binding energies[194].
The next generation of functionals takes into account the fact, that real systems are spatially inhomogeneous and exhibit varying densities. This kind of exchange-correlation functionals is called general gradient approximation (GGA). The GGA includes the density gradients $\nabla n(\mathbf{r})$ beside the density itself:

$$\boldsymbol{E_{XC}^{GGA} = \int d^3\mathbf{r} \cdot n(\mathbf{r}) \cdot \varepsilon_{xc}(n, \nabla n, \nabla^2 n, \dots)} \qquad \textbf{4.9}$$

The GGA gives better results for some properties, e.g. it describes better hydrogen bonded systems[195]. There are many various GGA functionals with different explicit dependence on $n(\mathbf{r})$ and $\nabla n(\mathbf{r})$. The examples of approximations commonly used in surface science are so called PW91 (Perdew-Wang)[196] and PBE (Perdew, Burke, Enzerhof)[197].

Periodic boundary conditions – plane wave basis sets

As it was demonstrated before, the ground state properties of many-body system can be calculated using Kohn-Sahm equations. Solving these equations in practice requires the wave function to be spanned with a complete basis set. For small systems with finite number of electrons, the hydrogen-like basis sets localized on the atomic nuclei can be applied. However, for a periodic system the natural choice is a discrete plane wave basis set:

$$\boldsymbol{\varphi_{\mathbf{k},j}(\mathbf{r}) = \frac{1}{\sqrt{\Omega}} \sum_{\mathbf{G}} A_j^{\mathbf{k}}(\mathbf{G}) \exp[i(\mathbf{k}+\mathbf{G}) \cdot \mathbf{r}],} \qquad \textbf{4.10}$$

where **k** lies within the first Brillouin zone, **G** represents reciprocal lattice vectors, Ω is the volume of a unit cell and $A_j^{\mathbf{k}}(\mathbf{G})$ are Fourier coefficients.
The effective potential can be represented by a similar transform:

$$\boldsymbol{V_{eff}(\mathbf{r}) = \sum_{\mathbf{G}} V_{eff}(\mathbf{G}) \exp(i\mathbf{G} \cdot \mathbf{r})} \qquad \textbf{4.11}$$

This leads to the following formulation of the terms (e.g. kinetic energy) within the Kohn-Sahm eq. 4.6:

$$\boldsymbol{E_{kin} = \Omega \sum_{j,\mathbf{k}} f_j^{\mathbf{k}} \sum_{\mathbf{G}} \frac{1}{2} |\mathbf{k}+\mathbf{G}|^2 \cdot \left|A_j^{\mathbf{k}}(\mathbf{G})\right|^2} \qquad \textbf{4.12}$$

To obtain the exact numerical solution, the summation would need to be performed over infinite Fourier series. In practice the expansion at each **k** point has to be finished at some cut-off energy E_{cut}:

$$\boldsymbol{E_{\text{cut}} = \frac{\hbar^2}{2m} |\mathbf{k}+\mathbf{G}|^2} \qquad \textbf{4.13}$$

The advantage of this approximation is that its quality can be simply controlled by a value of E_{cut}. However, one has to remember that increase og E_{cut} increases computational costs of a the calculation. It is crucial to choose the smallest E_{cut} that provides the accurate description of a studied system.

For an infinite solid, where the number of **k** points in infinite, one would have to integrate over the whole Brillouin zone in order to solve Kohn-Sahm equations. It would be required to calculate the following:

$$\overline{\boldsymbol{A}} = \frac{\mathbf{1}}{\boldsymbol{\Omega_{BZ}}} \int_{\boldsymbol{\Omega_{BZ}}} \boldsymbol{d^3\mathbf{k}} \cdot \boldsymbol{A}(\mathbf{k}) \qquad \textbf{4.14}$$

where $A(\mathbf{k})$ is a lattice-periodic function. In practice the wave function at **k** points close to each other is almost identical, so the total wave function can be represented by a finite number of **k** points (N_k). The most common sets of **k** points that do not depend on the type of crystal cell are those described by Monkhorst and Pack[198]. Within this approach the sampling points are distributed homogeneously in the Brillouin zone. The accuracy of this approximation can be increased by choosing sufficiently large number of N_k.
In case of metals, which exhibit discontinuity at the Fermi level for T = 0 K, Monkhorst and Pack approach has to be improved by introducing so-called smearing functions. These functions make the integration smoother. The most common smearing functions are Gaussian-type delta functions and "cold" smearings of Methfessel and Paxton[199] or Marzari and Vanderbilt[200].

Pseudopotential approximation

The approach described in the previous subsections would require large number of plane waves to describe core electrons, since the Kohn-Sahm wave functions exhibit strong oscillations close to the nucleus. To reduce the computational costs, pseudopotential method is applied. It is based on the fact, that for most physical systems the properties of the solid depend mostly on valence electrons. Within this approach the core electrons are treated as "frozen" and are replaced together with the strong ionic potential by a weaker and smoother effective pseudopotential. It is important that pseudo- and all-electron potentials have the same energies and amplitude outside the core radius r_c.
The most used pseudopotentials are norm-conserving (NCPP)[201] and ultrasoft[202] pseudopotentials. The NCPP must fulfill two conditions:

- in the region up to r_c the norm of the pseudo-wave function and the corresponding all-electron wave function are identical;
- pseudo- and all-electron wave functions are identical outside r_c.

Ultrasoft pseudopotentials are useful for the systems where the 2p all-electron wave functions are strongly localized near the core region, e.g. first row elements. Within this approach the charge of a core region is eliminated allowing the wave functions to be as soft as possible, but without fulfilling the norm-conservation condition. Another approach is the projector-augmented wave (PAW) method which introduce the linear transformation from the pseudo to the all-electron wave function[203].

Supercell method

A plane wave basis set that is based on Bloch's theorem can be used only for systems that are periodic in all three spatial dimensions. In case of lower dimensional systems, like surfaces, nanowires or atoms, the supercell approach is applied. It artificially introduces the three dimentional periodicity of a plane wave approach by a periodical repetition of a structure in the three dimensions even when it does not exhibit actual symmetry in all directions. For example, a surface is modelled as alternating slabs of bulk material and vacuum region (Figure 4.1). Vacuum regions that separate the slabs of material in z-direction have to be thick enough to avoid any interactions between the surface slabs or adsorbates.

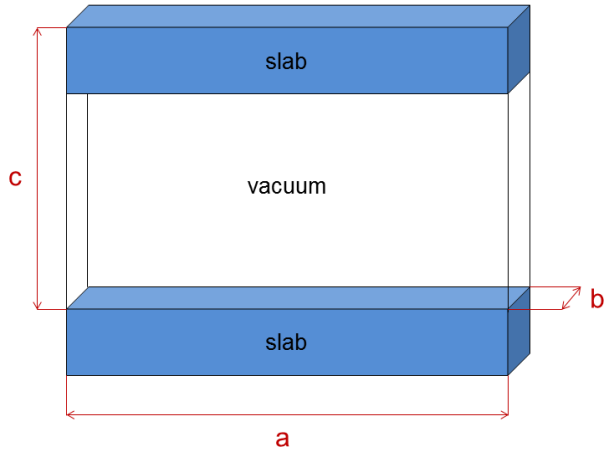

Figure 4.1. Supercell approach for surface modeling with plane wave basis sets: A surface of periodic cell dimensions *axb* is modelled as alternating slabs of bulk material and vacuum region; vacuum regions that separate the slabs of material in z-direction have to be thick enough (*c*) to avoid any interactions between the surface slabs or adsorbates.

Technical description of performed DFT calculations

The plane wave DFT calculations were performed with the Quantum ESPRESSO package[204]. The PBE functional[205] complemented with dispersion correction (DFT-D)[206] were used to model the electron exchange and correlation. Norm-conserving pseudopotentials were used to describe the electron-ion interaction. Plane waves up to a cutoff energy of 90 Ry were used as basis functions. The atomic structure relaxation for single Pc was done in a periodically repeated 30 Å x 30 Å x 27 Å supercells. Molecular monolayers were described within lateral periodicities between 6 Å x 6 Å and 15 Å x 15 Å. Convergence criteria of 10^{-4} eV/ Å for forces and 10^{-8} eV for the total energy were used.
The adsorption energies in both cases (SCIGRESS and Quantum ESPRESSO calculations) were calculated as

$$\boldsymbol{E_{ads} = E_{Pc+DMMP} - (E_{Pc} + E_{DMMP})} \qquad \textbf{4.15}$$

where $E_{Pc+DMMP}$ is the total energy of the MPc+DMMP system and E_{Pc} and E_{DMMP} are the total energies of the single Pc and DMMP molecule in the gas phase, respectively.

4.2 Experimental methods

4.2.1 Photoelectron spectroscopy

Photoemission spectroscopy is based on the photoelectric effect which involves emission of electrons from the sample irradiated with light of sufficiently small wavelength. The number of photoelectrons depends on the light intensity and the energy of electrons on the wavelength of light. Phenomenon of photoemission was reported for the first time by Hertz[207] in 1887. In 1905 it played an important role in confirming Einstein's postulate that light is quantized in photons of energy $h\nu$[208]. Half-century later the photoelectric effect was applied in the spectroscopy. Three different approaches have been developed in parallel:

- Siegbahn improved the energy resolution of electron spectrometers and then combined it with X-ray sources[209]. This led to a technique which today is called XPS;
- Turner *et al.* applied the photoelectronic effect to gases[210];
- Spicer measured photoelectron spectra from solids in vacuum using UV light irradiation[211]. This was the start of UPS. Later use of synchrotrons enabled extention of photon energy range further, to all spectral range between UPS and XPS.

Today XPS in a commonly used technique that provides information on the chemical composition, oxidation state of elements and dispersion of one phase over another.
XPS and UPS are based on photoelectric effect – an atom absorbs a photon of energy $h\nu$ and a core or valence electron with binding energy E_b is released with kinetic energy (Figure 4.2a):

$$\boldsymbol{E_k = h\nu - E_b - \Phi} \qquad \textbf{4.16}$$

where E_k is a kinetic energy of the photoelectron, h is Planck constant, ν is the frequency of the exciting radiation, E_b is a binding energy of the photoelectron with respect to the Fermi level of the sample, Φ is the work function of the spectrometer-sample system.
Figure 4.2b presents the basic principle of PE measurement. The light source is a gas-discharge lamp or a synchrotron radiation source. The light irradiates a sample and the electrons excited by the photoelectric effects are then analyzed with respect to their kinetic energy E_k and their momentum p in an electrostatic analyzer. Knowing the energy of light and the work function, one can determine the binding energy E_b.

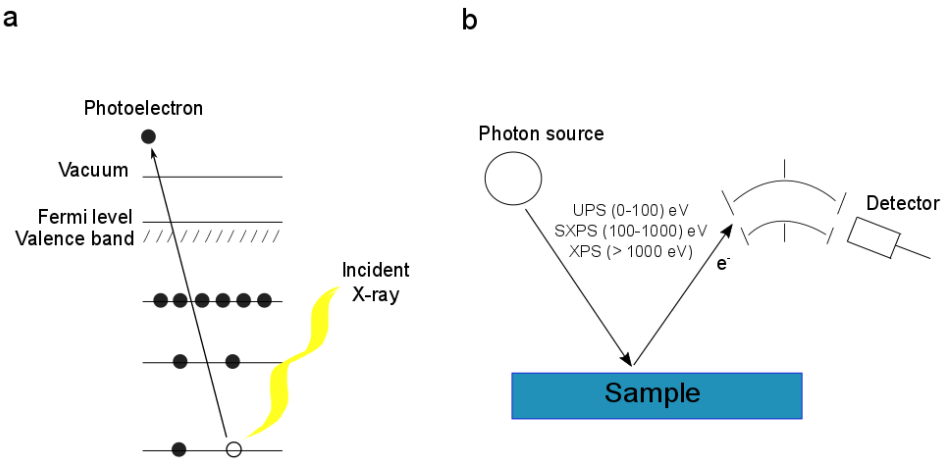

Figure 4.2. Basic principle of PES measurement: The light source is a gas-discharge lamp, an X-ray tube or a synchrotron radiation source; the light irradiates a sample and the electrons excited by the photoelectric effect are then analyzed with respect to their kinetic energy E_k and their momentum p in an electrostatic analyzer.[212]

The X-ray sources usually used are Mg Kα (1253 eV) and Al Kα (1486.3 eV)[213]. In XPS, the intensity of photoelectrons N(E) is measured as a function of their kinetic energy. The XPS spectrum is a plot of N(E) versus E_k, or more often, versus E_b. Peaks at the photoelectron spectrum are labeled according to the quantum numbers of the level from which the electron comes. The total momentum of an electron is $j=l+s$, where l is orbital momentum and s is a spin momentum. Orbital momentum of numbers 0,1,2,3,… are indicated as s,p,d,f,… The spin may be either up (s=+1/2) or down (s=-1/2), so each level with $l \geq 1$ has two sublevels. The energy difference between sublevels is called the spin-orbit splitting.

Since a set of binding energies is characteristic for an element, XPS is principally used to analyze the composition of the sample. The probing depth of XPS depends on inelastic mean free path of photoelectrons and it usually varies between 1.5 and 6 nm[213]. Binding energies contain information about chemical bonds, because the energy levels of core electrons depend slightly on the chemical state of the atom. It causes chemical shifts in the XPS spectra that typically range from 0 to 3 eV.

In UPS, instead of X-rays, UV light is used to excite the sample. The most frequently used sources are helium discharge lamps, which generate He I light at 21.22 eV and He II light at 40.80 eV[213]. At these energies photoemission is limited to the valence electrons. It is suitable for analyzing bonding in metals, molecules and adsorbed species. UPS provides also the macroscopic work function. That is because the slowest loss electrons (high binding energy cut-off in the spectrum) have zero kinetic energy, $E_k = 0$. On the other hand, the Fermi level electrons have the highest kinetic energy, $E_k = h\nu - \varphi$, where φ is a work function of the sample. Thus the width of UPS spectrum (difference between high binding energy cut-off and Fermi level), W equals $h\nu - \varphi$ and the work function can be calculated from the following equation:

$$\boldsymbol{\varphi = h\nu - W} \qquad \textbf{4.17}$$

Both, XPS and UPS show the density of states, but not in the same way. In XPS the valence band photoelectrons leave the sample with energies above 1 keV, while in UPS the kinetic energy of electrons is low, between 5 and 16 eV. This means that in XPS the final photoelectron

state is within unoccupied part of the metal density of states. The UPS spectrum represents a convolution of the densities of occupied and unoccupied states[213].

Technical description of performed PE experiments

XPS and UPS investigations utilized PREVAC EA15 hemispherical electron energy analyzer with 2D multi-channel plate detector. The system base pressure was $9x10^{-9}$ Pa. In case of XPS, the samples were irradiated with an energy of 1486.60 eV provided by an Al-K_α X-ray source (PREVAC dual-anode XR-40B source). 200 eV pass energy was set for survey spectra (scanning step 0.9 eV) while 100 eV pass energy was set (scanning step 0.05 eV) for particular energy regions. In the case of UPS measurements samples were irradiated with helium discharge lamp providing He I spectral line (excitation energy 21.22 eV). The pass energy was set to 5 eV and energy step was set to 0.05 eV. In both methods curved analyzer transfer slits were utilized for enhancing energy resolution. All of the spectra were taken with normal (i.e. 90° between sample plane and analyzer axis) take-off angle. The energy scale of the analyzer was calibrated to Au $4f_{7/2}$ (84.0 eV). For data analysis spectra were fitted utilizing CASA XPS® embedded algorithms and relative sensitivity factors. For background subtraction the Shirley function was used. If not specified in text, the components were represented by a product of Gaussian (70%) and Lorentzian (30%) lines.
Both, XPS and UPS methods can be utilized to evaluate sensing mechanisms. XPS provides information about the chemical bonds created between analytes and sensor structures and the related chemical shifts of the spectra. From UPS one can get the information about a change of the work function caused by a gas adsorption.

4.2.2 Thermal Desorption Spectroscopy

Thermal desorption spectroscopy (TDS) is an experimental method of the examination of molecules desorbed from a surface when the surface temperature is increased. The energy transferred during heating to the species adsorbed on the surface, at one point, causes the desorption. The temperature at which this happens is the desorption temperature that gives the information on the binding energy. TDS shows what species are adsorbed on the surface, analyzing the mass of desorbed molecules. It also gives the amount of adsorbed species from the intensity of peaks on the TDS spectrum. The total amount of adsorbed molecules is determined from the integral of the spectrum.
Figure 4.3 shows a schematic set-up for TDS. The sample is placed on a manipulator in an Ultra High Vacuum (UHV) chamber and heated resistively via tantalum or tungsten filament. The amount of adsorbed molecules is measured by increasing the temperature at a heating rate of typically 0.1 to 25 K/s[213]. A thermocouple is used to monitor the temperature. The heating procedure is usually controlled by the proportional-integral-derivative (PID) control algorithm with a computer or specialised equipment (e.g. Eurotherm) as a controller. The concentration of desorbing species is usually measured with a quadrupole mass spectrometer. Spectrometer can possess several measurement channels and TDS spectrum consists of the intensity of several masses as a function of temperature.

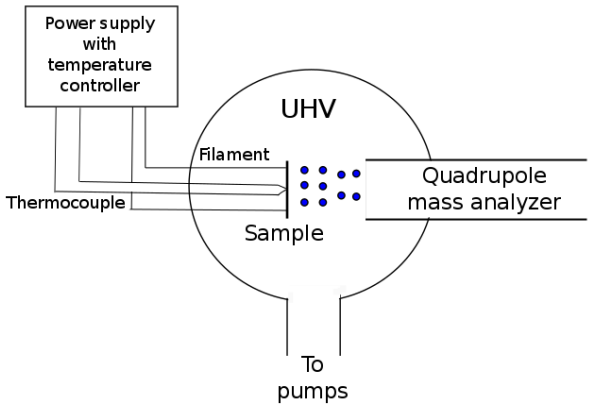

Figure 4.3. Typical set-up for TPD: The sample is placed on a manipulator in UHV chamber and heated resistively via tantalum or tungsten filament; a thermocouple is used to monitor the temperature; the heating procedure is controlled by the PID control algorithm with a computer or specialised equipment (e.g. Eurotherm) as a controller; The concentration of desorbing species is measured with a quadrupole mass spectrometer.

The important issue in TDS is pumping capacity – the pumping speed should be high enough to prevent re-adsorption of the desorbed species. The situation is more critical for light gases than for heavier ones. If the pumping rate is infinitely high, re-adsorption can be ignored and the relative rate of desorption (change in adsorbate coverage per unit time) is expressed by the following Arrhenius equation[214]:

$$\boldsymbol{r = -\frac{d\theta}{dt} = k_{des}\theta^n = \vartheta(\theta)\theta^n e^{-\frac{E_{des}(\theta)}{RT}}} \qquad \textbf{4.18}$$

where:

$T = T_0 + \beta t$
r – rate of desorption
θ - coverage in monolayers
t – time
k_{des} – reaction rate constant for desorption
n - order of desorption
ϑ - pre-exponential factor of desorption
E_{des} – activation energy of desorption
R – gas constant
T – temperature
T_0 – initial temperature of the experiment
β - heating rate (dT/dt)

From the Eq. 6.3 one can see that TDS provides information about:

- adsorbate coverage;
- the adsorption energy;
- lateral interactions between adsorbates, through the coverage dependence on the adsorption energy;
- the pre-exponential factor of desorption, which in turn reflects the desorption mechanism (from the transition state theory of reaction rates).

Since several variables in eq. 4.18 (E_{des}, ν and sometimes n) are a function of the coverage and influence each other[215], the analysis of TDS spectra is difficult in practice. The "complete

analysis method" calculates the pre-exponential factor, activation energy and orders of desorption from a series of spectra for every coverage separately.
Many authors utilize simplified methods of TDS analysis, which make use of such spectral features as the temperature of peak maximum (T_{max}) and the peak width at half-maximum (W). One of them is Redhead method[216] in which the activation energy of desorption is given by:

$$E_{des} = RT_{max}\left[\ln\left(\frac{\nu T_{max}}{\beta}\right) - 3.46\right] \qquad 4.19$$

The Eq. 6.4 is often used to determine E_{des} from a single TDS spectrum[217]. It is approximately correct for the first-order desorption and for values of ν/β between 10^8 and 10^{13} K^{-1} [213]. The Redhead approximation can be applied only if a reliable value of the pre-exponential factor is available.
Another method has been described by Chan, Aris and Weinberg[218]. They expressed $E_{des}(\theta)$ and $\nu(\theta)$ in terms of the peak maximum temperature T_{max} and the peak width at the half maximum and three quarters maximum for the first-order and the second-order desorption, respectively. The values of expressed $E_{des}(\theta)$ and $\nu(\theta)$ obtained by this method are extrapolated to zero coverage, in order to obtain the desorption parameters of a single molecule adsorbed onto empty surface[213].
The only method that operates quite well at high coverages is the "leading edge analysis" that was described by Kuppers[219]. This method recognizes that $\nu(\theta)$ depends on temperature. In order to fix temperature and coverage, a small temperature interval is selected at the low-temperature, high-coverage side of a spectrum. An Arrhenius plot of this interval is a straight line with a slope $-E_{des}(\theta)/R$. The advantage of this kind of analysis is a minimum number of assumptions, however the data has to be of extremely good quality.
The way to determine which procedures can be used is to test them with a set of simulated spectra[213]. Several methods of analyzing TDS are described and compared in an article by A.M de Jong and J.W. Niemantsverdriet[220].
Since the value of E_{des} approximately equals the value of adsorption energy, TDS is a useful tool in sensing mechanisms study. From the TDS spectra, one can obtain the information about the species adsorbed on the sensing structure's surface (both – analyte and impurities). The values of adsorption energies can be compared with the theoretical results in order to confirm the predicted mechanism of adsorption. Moreover, TDS provides the additional information about the decomposition of the desorbed species. This information is useful for the further study of sensor structure reproducibility.

Technical description of performed TDS experiments

The TDS experiments have been performed for bare MoO_3 and MoO_3/ZnPc before and after DMMP exposure in order to identify desorbing ambient-related and DMMP-related species. The thermal desorption from the surface was performed by thermal annealing with controlled temperature ramp (PID-monitored power supply, heating rate 0.5 K/min, base pressure 10^{-9} mbar). Partial pressure of selected desorbing species was controlled with RGA 100 (Stanford Research System) quadrupole mass filter in the temperature range of 40–400 °C. Due to the

experimental setup limitations, the measurements were restricted to the atomic masses up to 100 amu and to the control of 10 different species. In order to detect either the most probable molecules resulting from DMMP decomposition and species adsorbed from ambience, following masses have been chosen: 2 amu (H_2), 18 amu (H_2O), 28 amu (CO), 44 amu (CO_2), 31 amu (phosphorus), 79 (PO_3), 94 amu (methyl phosphonate), 46 amu. (dimethyl ether), 15 amu (methyl), 30 amu (formaldehyde). The spectra decomposition has been performed using Fityk software.

4.2.3 Sensor response

In the Chapter 2, the various methods of sensor response measurements have been described. Among them, the most common is a method based on sensor structure's electrical resistance measurements. This method can be used as a tool in sensing mechanisms evaluation, especially for thick-film structures, for which the Morrisson's equation can be applied to estimate the bend banding changes induced by gas adsorption. Additionally, the shape of sensor response curve (time dependent changes of the structure's resistance upon gas adsorption) can provide the information about the adsorption type.

Technical details of sensor response measurements

Samples were placed in a test chamber possessing inlet and outlet and electrical feedthrough. DMMP vapors were prepared from OVG-4, with certified permeation tube calibrated in 70 ºC. Synthetic dry air (~5 % relative humidity, Air Liquide) was applied as a carrier gas. The flow rate was controlled in order to obtain desired DMMP concentration. The concentration of DMMP in the mixture for the given flow can be calculated from the following equation:

$$\boldsymbol{C = \frac{22.4 q_D}{QM}}, \qquad \textbf{4.19}$$

where C is concentration (ppm), q_D is the permeation rate (ng/min), Q is flow rate (50 ml/min), M is DMMP molecular weight (124.08 g/mol).
The permeation rate in the calibration temperature T_1=70 ºC given by a producer (q_{d1}) equals 152 ng/min. To obtain the permeation rate q_{d2} in the temperature T_1, the following empirical relationship provided by the permeation tube producer was used:

$$\boldsymbol{\log q_{d2} = \log q_{d1} - 2950\left(\frac{1}{T_2} - \frac{1}{T_1}\right)}, \qquad \textbf{4.20}$$

Humidity of flowing air was controlled and measured with Owlstone Water Vapor Generator OHG-4. Resistance of sample was monitored with Agilent Multimeter type 34970A connected to the PC and the results were registered by Agilent BenchLink Datalogger programme. The resistance value was collected in every 10 s. Sensing properties were investigated at room temperature and elevated temperatures (100 ºC). In order to obtain the elevated temperature, samples were placed on the ceramic heater controlled by a DC power supply. Temperature on

the sample's surface was measured by Pt100 temperature controller connected to Agilent 34970A Multimeter.
Figure 4.4 shows the scheme of the sensor response experimental setup. Sensor response (SR) is defined as the percent resistance change calculated according to the following equation:

$$\boldsymbol{SR = \frac{R_0 - R_g}{R_0} \cdot 100\%} \qquad \textbf{4.21}$$

where R_0 is the resistance in ambience and R_g is the resistance of the sensor in the DMMP/carrier gas mixture.

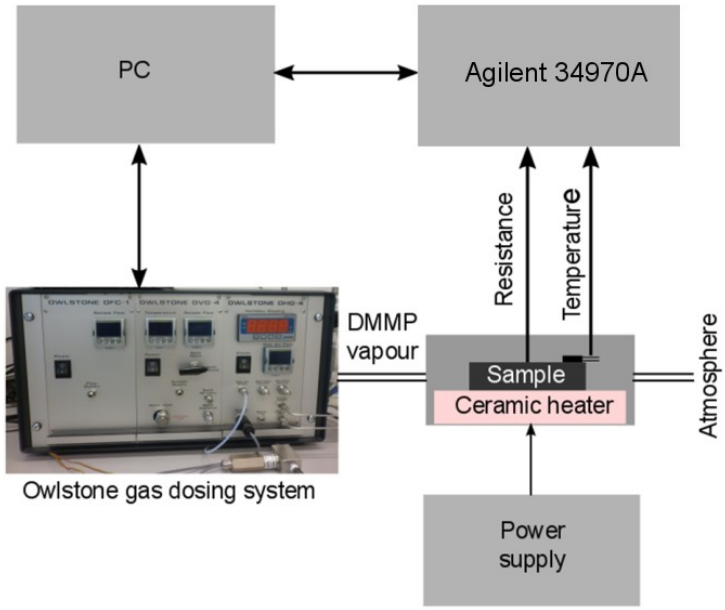

Figure 4.4. Scheme of the sensor response experimental setup

4.2.4 Atomic force microscopy

Atomic force microscopy (AFM) is a kind of scanning probe microscopy in which the localized interaction between a sharp probe and a sample is employed for surface imaging. The AFM can be used on almost all kinds of surfaces. Its applications include high-resolution imaging of surface topography, compositional mapping of heterogeneous samples and studies of local mechanical, electric, magnetic and thermal properties. The measurements can be performed in the scale from nanometers to hundreds of microns[221].
AFM is based on the forces between a tip and atoms in the surface. The tip is mounted on the flexible arm (cantilever) and placed at sub-nanometer distance from the sample. During the scanning, the tip is deflected as a result of the interatomic interaction with surface atoms. Various methods of measuring these deflections exist[222,223,224], i.e. optical or electrical. The surface imaging is realized by detecting the tip-sample force in different locations while the probe is scanning the surface using a piezoelectric actuator. To ensure that the force is kept at a constant level, a feedback control is applied. The main components of atomic force

microscope are probes, detection system, piezo-scanners and electronics for a management of scanning procedures and data acquisition (Figure 4.5).

With AFM, the force between atoms at the tip and the sample which are located as close as 0.1–100 nm can be measured. The forces can be attractive or repulsive. The attractive forces include vdW interaction, electrostatic forces, covalent forces etc. For the materials with hydrophilic properties in ambient condition water meniscus is formed on the surface, causing attractive forces called capillary forces. The repulsive forces can be considered as hard sphere repulsion, Pauli-exclusion interaction and electron–electron Coulomb interaction. The forces at atomic scale can be also classified as short- and long-range forces. The contribution of short-range forces is used to image the atomic arrangements with high resolution. For the distance of 10-100 nm between probe and sample's surface, only the long-range forces, such as van der Waals, electrical and magnetic forces are detected. If the scanning is done on a clean, electrically neutral and non-magnetic surface, only the van der Waals forces contribute to the image. The schematic of a typical force-distance curve (Figure 4.6) can be represented by Lennard-Jones potential. Far from the sample, the cantilever is not affected by interatomic forces and is in its free equilibrium position. Closer to the surface, attractive forces act upon the tip and bend the cantilever towards the sample. When the tip is in contact with the surface, repulsive forces dominate, deflecting the cantilever backwards.

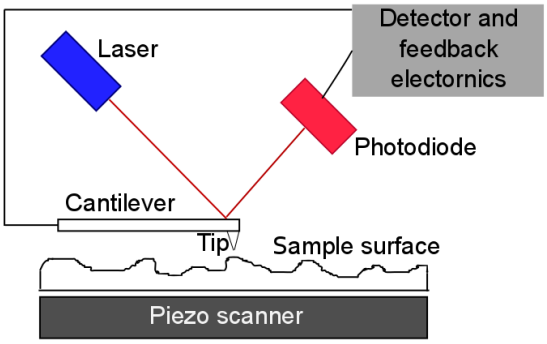

Figure 4.5. Basic principle of AFM measurement

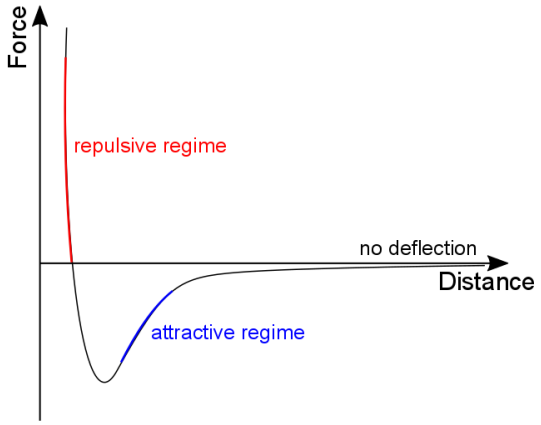

Figure 4.6. The schematic of a typical force-distance curve represented by Lennard-Jones potential.

There are three main operation modes of AFM: contact mode, non-contact mode and tapping mode. The contact mode is usually applied to obtain surface morphology and it is the only one if atomic resolution is required. The non-contact mode is mostly used for imaging magnetic domains or electronic devices. In the ambient conditions liquid meniscus layer is formed on the most samples. To overcome this problem, dynamic contact mode (also called tapping mode) has been developed and it became the standard for work on surfaces that are easily damaged.
The AFM is an auxiliary method in sensor materials investigation, since it does not provide the information about sensing mechanisms. It is used to study indirectly the adsorption sites availability. From the AFM topography image one can obtain the surface roughness which is a

measure of the surface development. Moreover, the phase AFM image can be useful for sensing structures consisting of two different materials. Phase imaging refers to the detection of the phase lag between the signal that drives the cantilever oscillation and its output signal[225]. Thus, it can be used for distinguishing the areas of different mechanical properties (thus e.g. different materials).

Technical description of performed AFM experiments

The PSIA XE-70 scanning microscope worked in non-contact mode. The Budget Sensors Tap300 Al-G cantilevers (resonance freq. 300 kHz, spring constant 40 Nm^{-1}) were used. The XEI®, PSIA and Gwyddion® image processing software allowed to correct sample inclination and distortions caused by z-scanning stage. No other corrections to the images were made. For quantitative topography analysis the Gwyddion® software was also used. As the surface roughness representative, the root mean square (RMS) of roughness was quantified, where the root mean deviation from a plane was analyzed. Surface area estimation was performed by triangulating the surface (as stated in the algorithm description) and summing up their area to obtain the total area. Further details on the methodology can be found in references[226,227,228].

4.3 Samples fabrication

CuPc

Copper phthalocyanine (CuPc) (10 nm or 100 nm) was deposited onto glass (B270) substrate with golden IDE by physical vapor deposition (PVD) method in UHV conditions. Substrate was pre-cleaned with acetone and isopropanol in ultrasonic bath, then rinsed with de-ionized water and purged with pure N_2. CuPc was deposited onto substrate kept at room temperature from sublimed powder (99.7%, Sigma Aldrich GmbH). Prior the deposition the CuPc powder was de-gassed @220°C for 2h. The base pressure of the evaporation system was $6 \cdot 10^{-7}$ Pa. The phthalocyanine thickness control was conducted by quartz crystal microbalance (QCM, Inficon XTC3M), the deposition rate was kept at the level 0.02 nm/s.

Pc/Pd

Metal free phthalocyanine (H_2Pc) or CuPc (100 nm) was deposited onto glass (B270) substrate with golden IDE by PVD method in UHV conditions in the same setup and procedure parameters that for described above CuPc layers. After Pc deposition, additional 10-nm-thick film of palladium (Pd) was evaporated on the phthalocyanine layer in high vacuum conditions (separate chamber, base pressure $5 \cdot 10^{-6}$ Pa) by PVD method. The Pd was evaporated from resistively heated crucible using palladium droplets as target. The thickness and deposition rate was also controlled by Inficon QCM. The deposition rate was kept at the level of <0.01 nm/s in order to keep the Pd vapour at the lowest possible temperature to prevent possible pinhole effect in Pc layer.

MoO_3/ZnPc

Zinc phthalocyanine (ZnPc) (10 nm) was deposited by thermal evaporation method onto glass substrates with interdigitated gold electrodes (Metrohm DropSens) and molybdenium (VI) oxide (MoO_3) thin layer (10 nm). Substrates were pre-cleaned with isopropanol and purged with pure N_2, then kept in the ultraviolet (UV) cleaner for 5 min. Prior ZnPc deposition, thin layer of MoO_3 was evaporated on the substrate at room temperature in high vacuum conditions using Lesker Spectros II Evaporation System with quartz crystal microbalance (QCM) thickness control. The base pressure was 10^{-6} mbar. The deposition rate was kept at the level of 0.01-0.03 nm/s. After MoO_3 deposition, 10-nm-thick film of ZnPc was deposited from the sublimed powder (97%, Sigma Aldrich GmbH) in high vacuum (base pressure 10^{-6} mbar) in the same evaporation system (separate chamber). The deposition rate was kept at the level of 0.05 nm/s.

DMMP exposure

Before the study of DMMP adsorption by PE and TDS methods, the MoO_3/ZnPc sample was placed in the environmental cell (320 ml) possessing gas inlet and outlet and electrical feedthrough. DMMP vapor was prepared from Owlstone vapor generator (OVG-4), with certified permeation tube calibrated in 70ºC. Nitrogen 5.0 (Air Liquide) was applied as a carrier gas. The cell was saturated with nitrogen/DMMP mixture. During the DMMP deposition the chamber outlet was closed. The permeation oven was heated to 100 ºC. The nitrogen/DMMP mixture flow rate was set to 50 ml/min. For the permeation rate calculated from the eq. 4.20 (747.4 ng/min) the DMMP concentration in the carrier gas the given conditions equals 6 ppm. After 2 h the nitrogen/DMMP flow was stopped and the sample was kept for 3 days in the cell with the closed outlet. In order to provide stable temperature during DMMP deposition, the samples were placed on the ceramic heater controlled by a DC power supply. Temperature on the sample's surface was measured by Pt100 temperature controller connected to Agilent 34970A Multimeter.

5 Sensing mechanisms evaluation - results

Before the discussion of the results a word of introduction is essential. The studied structures can be divided into two main groups differing in the methodological approach. The first group was chosen based on the Supervisor's previous expertise (Jakubik *et al.*[69]) with Pc/Pd structures for other reducing gas (H_2) detection. For this kind of structures the most promising material, H_2Pc/Pd, was selected after the SRs measurement and surface morphology examination. The structure was then subjected to XPS analysis of surface's chemical composition after DMMP exposure and phase imaging by AFM. This experimental approach, although some interesting results, had to be supplemented by a theoretical modeling for a better understanding of the physical processes responsible for the sensor structures' performance. For this purpose semi-empirical methods have been employed.
The second group of structures was selected to answer some open questions. According to the reviewed literature, MPcs should be sensitive to DMMP, especially CuPc. The CuPc and CuPc/Pd structures have been considered in the preliminary study, but their performance was not satisfactory. Therefore, the further study was focused on the evaluation of sensing mechanisms for MPcs. For this group of structures the main issue was to explain the physical processes that could potentially drive sensing properties. The most promising MPc, ZnPc, was chosen from semi-empirical modeling of DMMP adsorption instead of time and cost-consuming experimental investigation of all considered MPcs. The detailed theoretical study of DMMP adsorption on ZnPc was carried out by DFT method and sensing mechanism was confirmed by XPS, UPS and TDS study.

5.1 First approach: Metal-free phthalocyanine/palladium structures

Preliminary study to choose the optimum sensing material was carried out on the following structures:

- Single-layers: 10 nm CuPc, 100 nm CuPc;
- Bilayers: 100 nm CuPc + 10 nm Pd, 100 nm H_2Pc + 10 nm Pd

CuPc and H_2Pc werechosen among phthalocyanines basing on the Bohrer *et al.*[2] study of different Pcs sensitivity to various toxic gases, including DMMP.
First, the SRs were measured in order to find the most perspective structure for the further investigation. To support the choice based on SR, the morphology of the sensor structures was characterized by AFM and the SR were correlated with morphological features of the samples. Further evaluation of sensing mechanism was performed on a structure that revealed the highest SR.

5.1.1 Sensor responses

Results of SR measurements for CuPc single-layer structures exposed to DMMP vapors of three different concentrations are presented in the Figure 5.1. The resistance of 10 nm CuPc film did not change with the flowing gases, both pure air and air/DMMP mixture at the room temperature and at elevated temperature. The resistance of the thicker layer was constant in the room temperature, but at 100 °C response increased after first exposure to the synthetic dry air. This can be explained by the drop of temperature in the testing chamber. The sample at 100 °C is cooled by the flowing air due to the relative high temperature difference between the sample's surface and the flowing air that has a room temperature. When the air flow stabilizes during the experiment, the cooling effect becomes negligible. After exposure to 60 ppb of DMMP vapor, further increase of the response was observed. The sensor did not give stable response to higher concentrations of analyte. Presented results show clearly the limitations of the single-layer structures as the DMMP sensor. Therefore, the Pd ultra-thin layers have been used as the catalyst to enhance the sensing properties of examined materials.

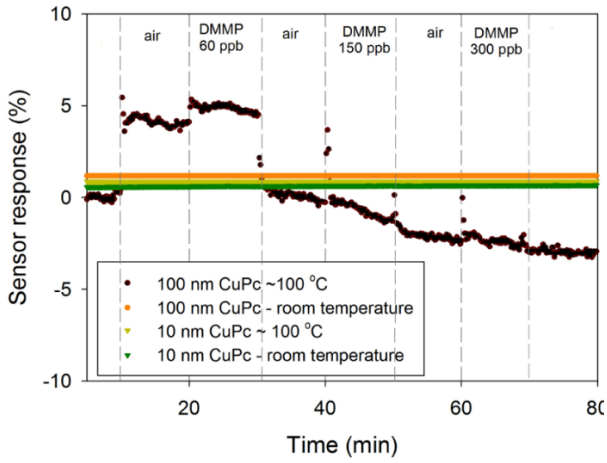

Figure 5.1. Time-dependent SR of monolayer CuPc (10 nm and 100 nm) structures exposed to DMMP vapor at room temperature and at 100°C[229]

Although the palladium layers are expected to increase the sensing properties significantly, the bilayer CuPc/Pd structure was not sensitive to the analyte in the room temperature. Therefore the experiment was repeated at the elevated temperature (100 °C). Time-dependent characteristic for this sensor structure exposed to DMMP vapor at 100 °C is depicted in the Figure 5.2a. Following presented results, one can observe substantially higher responses and better recovery effect than in case of the sensor without palladium layer. However, changes of resistance in the presence of higher DMMP concentrations were lower than after exposure to 60 ppb. It could point the saturation effect of the sensor or it could indicate the irreversible chemisorption of the analyte at the sensing structure's surface. Due to fact that the sensor response of CuPc/Pd structure was found to be strongly unsatisfactory, the different phthalocyanine layers were prepared for examinations. Following findings of Bohrer *et al.*[2] the H_2Pc was chosen as the most perspective alternative for CuPc. In this case, the Pd layer was also added to enhance the sensor response which gave the expected results even at room temperature as can be seen in Figure 5.2b. As it can be observed, the H_2Pc/Pd structure gave higher response than CuPc/Pd. However, it did not reach saturation level in the given time of exposure. Response was constant for different concentrations of analyte. This result could be

explained by Langmuir's model of adsorption[97] – the DMMP coverage reaches the saturation level which is constant for all applied concentrations.

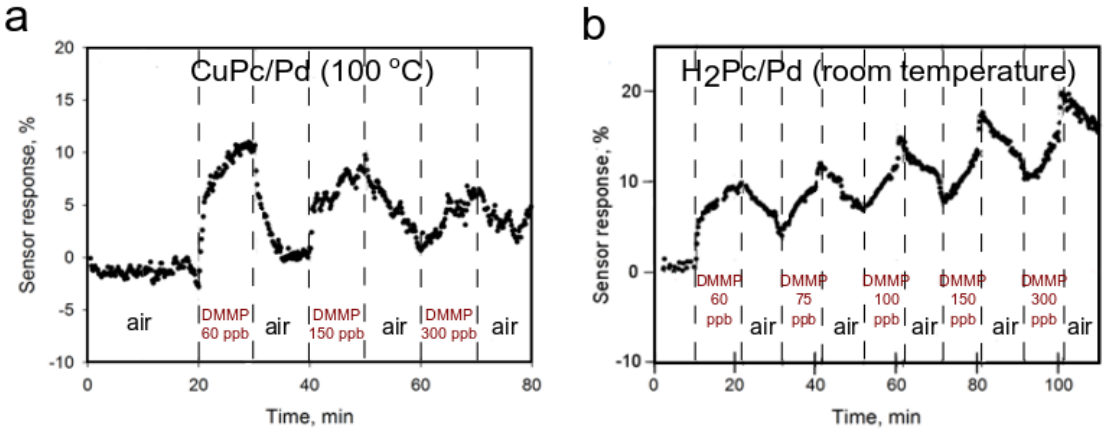

Figure 5.2. Time-dependent SR of bilayer a: CuPc/Pd and b: H_2Pc/Pd structures exposed to DMMP vapor[230]

5.1.2 Surface morphology

The exemplary AFM images taken for single-layer structure are presented in Figure 5.3a (for 10-nm-thick CuPc layer) and in Figure 5.3b (for 100-nm-thick CuPc). As a measure of roughness the RMS of roughness parameter was calculated for all of the samples. In case of 10-nm CuPc the RMS was equal 1.3 nm while for 100 nm CuPc RMS was determined as 3.5 nm. The active surface was determined as 1.009 μm^2 and 1.083 μm^2 respectively which is consistent with what can be seen in the Figure 5.3. The barely developed surface with not fully crystallized structures in case of thinner layers in correlation with almost no sensor effect led to conclusion that the sensor response could be related to not fully developed CuPc layer.

AFM results for bi-layered structures are presented in Figure 5.3c for CuPc-based and Figure 5.3d for H_2Pc-based. The scans present structures of moderate size which are distant from topography of bare Pc surfaces reported in literature[231, 232]. Hence, it points that the Pd layer is not reproducing the calssic Pc topography. Basing on Gwyddion built-in algorithms the determined RMS parameters were 6.6 nm and 9.9 nm while the active surface was 1.220 μm^2 and 1.095 μm^2 respectively, which corresponds to moderately developed surface. However, it has to be noted that the algorithm gives the averaged value over whole examined surface. Simultaneously looking at the topography images one can observe areas of significantly bigger topographical feauters, reaching nearly 80 nm in height, hence the surfaces exhibit developed number of topography – related adsorption sites. It is clearly visible that the addition of palladium thin layer increases significantly the active surface area and the surface's roughness. This obviously have an impact on the sensing properties of the layers as could be seen in SR.

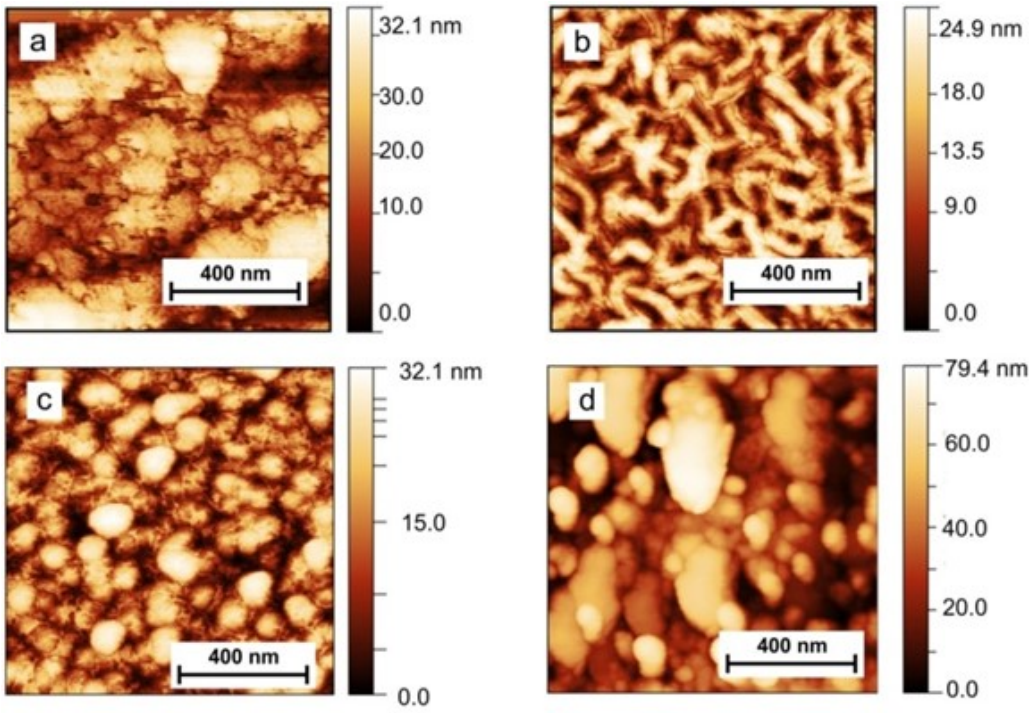

Figure 5.3. Topography image (1x1 μm2) of: a: 10 nm copper phthalocyanine layer, b: 100 nm copper phthalocyanine layer, c: CuPc-Pd bilayer structure, d: H_2Pc-Pd bilayer structure[229]

5.1.3 H_2Pc/Pd/PdO sensing mechanism evaluation

After the preliminary study of various structures' sensitivity to DMMP, H_2Pc/Pd structure has been chosen for a sensing mechanism evaluation. The study was focused on the DMMP adsorption on the H_2Pc/Pd structures at room temperature. Room temperature chemical sensors are of the particular interest because of their low power consumption[233,234,235]. Moreover, the sensor working at low temperature is more likely reversible since at high work temperatures DMMP molecule can dissociate forming covalently attached species[38] that cause poisoning of a sensing material. This effect is undesirable since it inhibits a reversibility of the sensor structure.

In order to describe sensing mechanism, first the sensor response to one DMMP concentration (60 ppb) was analyzed in details, considering the shape of the sensor response curve. Moreover, $e\Delta V_s$ was calculated from the Morrisson's model (eq. 2.26) basing on the measured change of electrical resistance in the presence of DMMP. Next, theoretical modeling of the sensor structure - DMMP interaction was performed by semi-empirical quantum chemistry methods in order to explain the experimental results Different variants of metallic overlayer were considered in the modelling including bare palladium and palladium(II) oxide (PdO). The further experimental investigations were based on XPS chemical characterization of DMMP exposed surface supported by AFM imaging.

Sensor response curve analysis

The SR of the H_2Pc/Pd structure to different DMMP concentrations was shown in the section 5.1.1 (Figure 5.2). Here, the exemplary SR to 60 ppb (lethal concentration of DMMP vapour) is presented (Figure 5.4), in order to analyze it from the point of view of sensing mechanism. As expected for the reducing gas and p-type semiconductor, resistance of the layer increased after DMMP adsorption. Since band bending eV_s is linked with the surface electrical conductivity, G, by Morrison's equation (see Chapter 2) its change can be estimated from experimental data using eq. 2.26. One has to remember that eq. 2.26 is dedicated for the thick-film gas sensors, where the thickness is higher than the Debye length, L_D (eq. 2.27). For H_2Pc n_p equals around $4 \cdot 10^{20}$ m^{-3} [236], hence Debye length in H_2Pc is close to 100 nm. This value is similar to the thickness of the investigated layer. Thus, it was assumed that in terms of electronic behaviour, considered here H_2Pc structure possessed attributes of thick film and assumptions for eq. 2.26 have been fulfilled. For the obtained sensor response (SR ~ 10 %) R_g/R_a in the eq. 2.26 equals 0.9. For this value of R_g/R_a, $e\Delta V_s$ is around 0.003 eV, hence it can be treated as negligible. This result suggests that $\Delta\chi$ plays bigger role in the SR and indicated the dipole interaction (physisorption or weak chemisorption) as a main sensing mechanism, which was also confirmed by the shape of the response curve. The gas adsorption region can be attributed to the multilayer physisorption on the surface imperfections[102]. The first rapid increase of the sensor response (II) was a result of the fast adsorption on the most available sites. Then slow saturation on the less accessible adsorption sites (III) was observed. The following area of the full saturation (IV) is assigned to the equilibrium between adsorption and desorption. On the other hand, the slow desorption (V) can be explained by the capillary condensation of the adsorbate on the micropores[237] which results in the trapping of DMMP molecules on the sensing layer (see Figure 5.4).

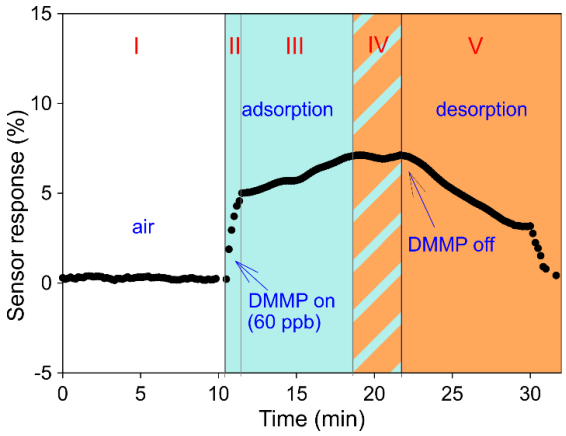

Figure 5.4. SR of the H_2Pc/Pd/PdO structure to 60 ppb of DMMP (I – pure synthetic air exposure, II – fast DMMP adsorption on the most available (first order) adsorption sites, III – slow DMMP adsorption on the second order adsorption sites, IV – full saturation, V – slow desorption[238]

Semi-empirical modeling

In order to theoretically qualify sensing mechanism, author proposed the method based on the evaluation of adsorption energies between sensing layers and DMMP and sensing layers' work function changes estimation. To determine adsorption energies between studied materials,

semi-empirical modeling using SCIGRESS software was performed. In order to rationalize the computational cost, simulations were carried out for one molecule of H_2Pc and one DMMP molecule (Figure 5.5).

Since the computational modeling of adsorption on two-component surface would require too high level of computation, the cluster approach was applied for palladium and palladium oxide modeling[239]. Following the work of Melle-Franco *et al.*[240] it was assumed that using small clusters, the information about adsorption processes can be obtained with a good approximation without high complexity of the calculations. Hence, the palladium trimer (Pd_3) and the stoichiometric Pd_4O_4 cluster of palladium (II) oxide were chosen as the most convenient in this study because of the dimensions of the modelled structure.

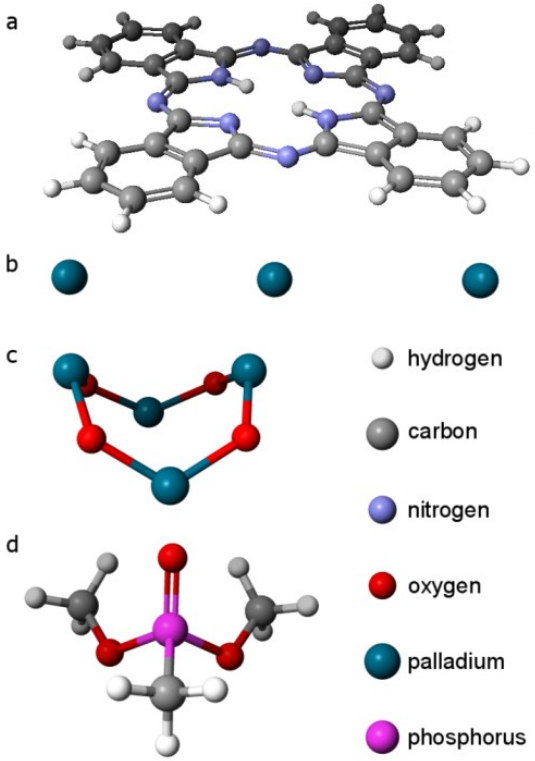

Figure 5.5. Chemical structures used for semi-empirical modeling: a: metal-free phthalocyanine molecule, b: Pd_3 cluster, c: Pd_4O_4 cluster, d) DMMP molecule[238]

Results of the interaction simulations for H_2Pc-DMMP, H_2Pc-Pd-DMMP and H_2Pc-PdO-DMMP are presented in the Figure 5.6. Since the synergic results of the particular structure's interaction with DMMP was a main interest of this study, the electronic processes present on the H_2Pc/Pd/PdO junction have been not considered separately. However, they were extensively discussed elsewhere for similar metal/phthalocyanine systems[241]. Moreover, the interface effects were embedded in the simulation (H_2Pc/Pd or H_2Pc/PdO structures were optimized first and next DMMP adsorption on such structures have been modelled) and as a result of computation one can observe only differences in adsorption energies between bare H_2Pc and DMMP and H_2Pc/Pd or H_2Pc/PdO and DMMP. As one can see, for all the structures, there is no chemical bond visible. The obtained adsorption energies are 0.26 eV, 0.65 eV and 0.87 eV for H_2Pc-DMMP, H_2Pc-Pd-DMMP and H_2Pc-PdO-DMMP respectively (Table 5.1). The values for H_2Pc-DMMP and H_2Pc-Pd-DMMP indicate physisorption[242] and the addition of

palladium increases adsorption energy between phthalocyanine and DMMP. For the H_2Pc-PdO-DMMP interactions one can assume strong physisorption or weak chemisorption[241].

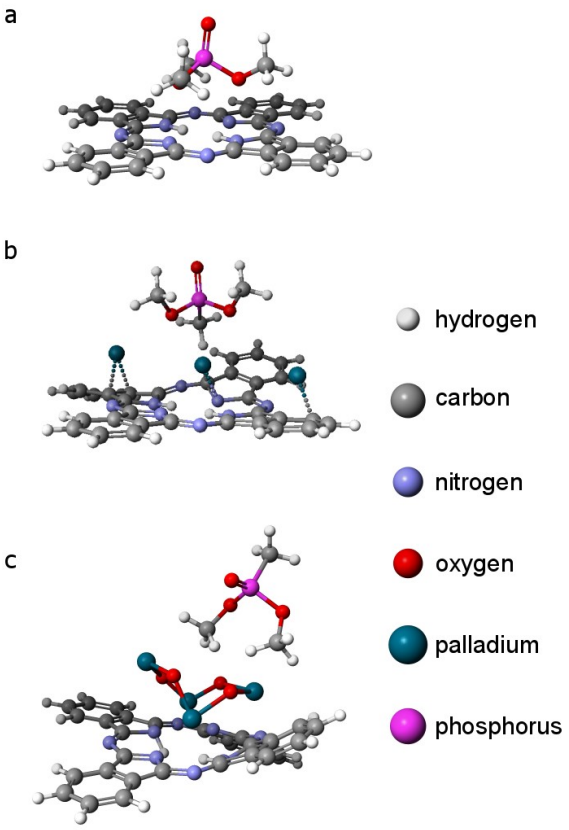

Figure 5.6. The results of semi-empirical modeling of the interaction with one molecule of DMMP for: a: H_2Pc, b: H_2Pc-Pd, c: H_2Pc-PdO structures[238]

Table 5.1. Energies of DMMP adsorption on H_2Pc, H_2Pc/Pd and H_2Pc/PdO calculated by semi-empirical HF PM6 method

Structure	H_2Pc+DMMP	H_2Pc/Pd+DMMP	H_2Pc/PdO+DMMP
E_{ads}, eV	0.26	0.65	0.87

For better understanding of adsorption mechanism, WF changes of the adsorbent surface should be also considered. Change of the electron affinity caused by dipolar momentum of adsorbate layer can be estimated from the Eq. 2.17. Dipolar momentums for H_2Pc-Pd-DMMP and H_2Pc-PdO-DMMP interactions obtained from semi-empirical simulations were 4.6 D and 7.2 D respectively. For DMMP molecules as adsorbate layer ($\varepsilon_r = 22.3$[243], $d = 0.58$ nm[244]) and H_2Pc-Pd or H_2Pc-PdO as a sensing layer, $\Delta\chi$ equals 0.23 eV and 0.36 eV respectively. It confirmed the results from adsorption energies calculation that indicated stronger interaction of H_2Pc/PdO with DMMP molecule. Above values of $\Delta\chi$ are much higher that band bending change estimated from SR, as expected.

Surface morphology – detailed study

In the section 5.1.2 the morphology of the H_2Pc/Pd structure has been shown in the comparison with other structures considered in the preliminary study.
Here, the investigations were followed by the phase imaging scans of the examined areas (Figure 5.7b). This method was used for examination of the Pd layer integrity. As it can be observed in Figure 5.7b, Pd is not covering uniformely the whole Pc surface but it seems to agglomerate into the metal nanoclusters. The tendency of Pd for cluster-like assembly was discussed previously in[70]. The discontinuities in the Pd film (well visible in phase diagram) makes that number of adsorption sites of Pc, uncovered with Pd, can be affected by preferential impurities (e.g. oxygen) uptake from ambience[245,246].

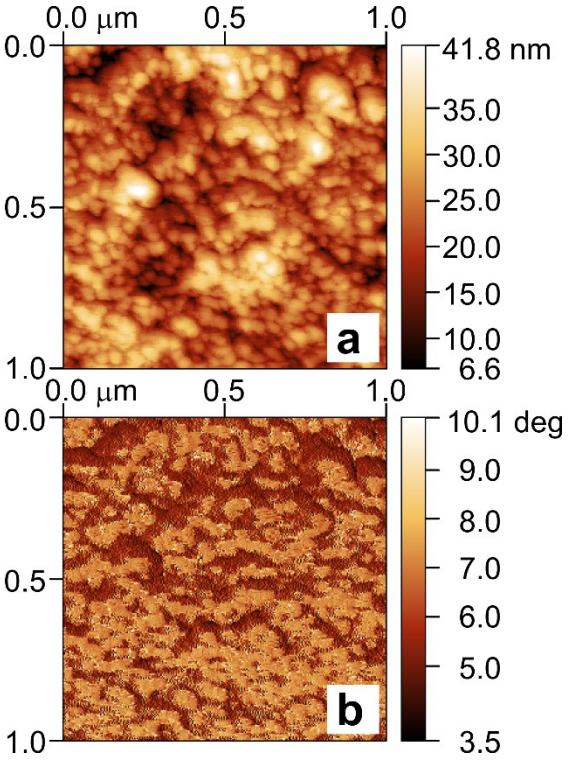

Figure 5.7. Topography image (1x1 µm2) taken for H2Pc/PdO layers: a: topography scan b: structure's phase diagram. The discontinuities in Pd layer are clearly visible as intensity differences in phase diagram[238]

Surface chemical composition

In order to qualify the surface chemical structure of the examined samples, XPS analysis of the H_2Pc/Pd surface after DMMP exposure was performed. The representative XPS energy regions are presented in Figure 5.8. Figure 5.8a main panel depicts decomposition of the most representative for phthalocyanine's structure C 1s region. The main constituents, i.e. C-C and C-N components together with their satellites (S_{C-C} and S_{C-N} respectively) were fitted with the appropriate for Pc layers intensity ratios[247]. Decomposition of the photoemission signal revealed parasite C=O / O-C-O broad component which can be related to the ambience – induced contamination. Due to significant broadening of this component, the accurate distinguishing between proposed contamination components was abandoned. The confirmation

of the carbon – related contamination was supported by O 1s energy region (right inset to Figure 5.8). Decomposition of the O 1s signal revealed three main components, out of which the most important are: the O-Pd component (which gives the support for palladium oxide existence) and intense carbon contamination related peak. The third component assigned to adsorbed water – related oxygen can possess additional components related to contamination, however their revelation would be speculative at the sensitivity level. The left inset to Figure 5.8 presents symmetric N 1s region with expected one N-C component. Further confirmation on existence of palladium in two different oxidation states is given in Figure 5.8b which presents Pd $3d_{5/2}$ BE region. Two distinguished components can be ascribed to metallic Pd (~335.2 eV BE) and to PdO (~336.2 eV BE). The relative intensity of the Pd/PdO components indicates that approximately 1/3 of the Pd was oxidized during or after the deposition process.
Which is important for this study, no trace of phosphorus was detected in XPS measurements. This is the signal that the DMMP molecules were desorbed in UHV conditions which confirmed previous suspicions that no chemisorption occurred during DMMP exposure. This result in agreement with Kim et al.[38] which found that adsorption of DMMP on metal oxides at room temperature occurs through P=O functional groups strong physical interaction with the metal oxide.

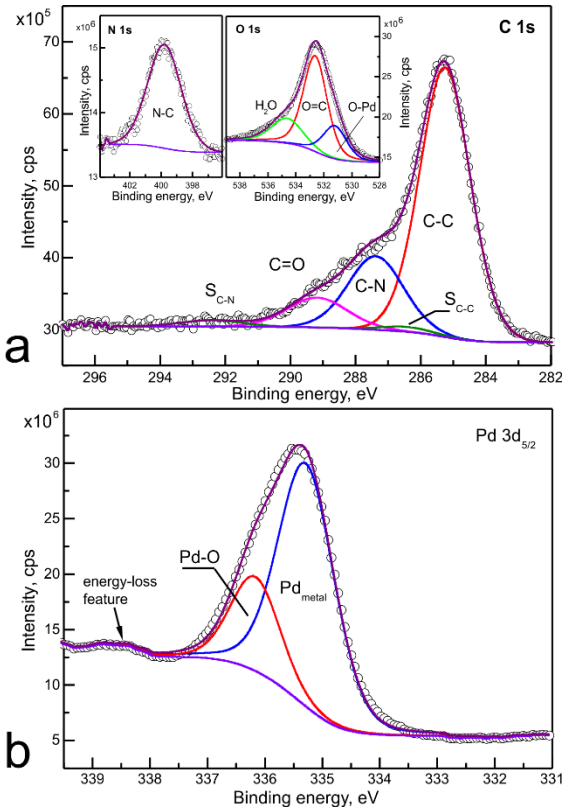

Figure 5.8. Most significant energy regions recorded by XPS for the H_2Pc/Pd surface after DMMP adsorption. Panel a – C 1s energy region; insets to panel a - N 1s (left) and O 1s (right); panel b - Pd $3d_{5/2}$ peak exhibiting metal and metal-oxide contribution. For further details – see text[238]

5.1.4 First approach conclusions

Basing on modeling and real sensor investigation or H_2Pc/Pd/PdO structure, the conclusion arised, that dominating sensing mechanism is dipolar effect with almost negligible charge transfer through the surface of sensing layers. Due to low concentration of charge carriers, decay of electric field related to the interaction (connected with the charge transfer or its relocation over the sensing layer/adsorbate layer interface) with gas on the surface was visible as a small change of band bending. It was two orders of magnitude lower then corresponding dipole interaction (0.003 eV with respect to 0.23 – 0.36 eV). Moreover, calculated adsorption energies indicated physical or weak chemical interactions for H_2Pc/Pd as well as for H_2Pc/PdO. Hence, one can conclude that physisorption is the main mechanism responsible for DMMP molecule attachment to the sensing layer at room temperature. This assumption was confirmed by XPS characterization and sensor response curve shape. The discussion of sensing mechanism in studied H_2Pc/Pd/PdO structure is summarized in the Figure 5.9. DMMP adsorbs on the H_2Pc/Pd/PdO structure's surface by a physical interaction and forms an adsorbate dipolar layer that causes relatively high changes in electron affinity and a small change of the band bending. The surface exhibits various types of adsorption sites due to the structural defects and a formation of palladium agglomerates on the Pc's surface. The adsorption sites are partially occupied by impurities from the ambience. Considerably weak sensor response to the dipolar effect can be due to the small amount of active adsorption sites or their low availability because of surface imperfections (i.e. grain boundaries, structural defects, etc.) and impurities (like e.g. C, O_2) adsorption.

Figure 5.9. The proposed scheme of DMMP dipole-induced adsorption (left panel). Right panel shows the simplified scheme of changes in surface band bending $e\Delta V_s$ and electron affinity $\Delta\chi$ after DMMP adsorption.[238]

5.2 Second approach: metallo-phthalocyanines based structures

As it was presented in the previous sections, DMMP physisorbs at the room temperature on the H_2Pc and its interaction with the sensing material can be enhanced by palladium and palladium oxide. However, MPcs possess active sites for chemisorption (metal centers) which can potentially form a chemical bonding with DMMP[2]. It gives a possibility to achieve higher sensor responses due to the charge transfer. The possibility of DMMP detection by the MPc layer without the expensive catalyzer such as Pd would simplify the sensor and reduce its cost. For this reason, the second part of the study was focused on DMMP adsorption on MPcs. To comprehensively evaluate sensing mechanism, the detailed computational study of DMMP adsorption on these materials was performed and for the most promising material – ZnPc further experimental study was carried out to verify theoretical findings. The ZnPc layers for experimental study were deposited on MoO_3 substrate that was chosen among SMOs basing on the literature. Before the experimental part, the interaction of DMMP with MoO_3 and the most common SMO used in gas sensing, SnO_2 was first compared theoretically by semi-empirical methods.

5.2.1 Preliminary semi-empirical modeling of DMMP adsorption on MPcs

Preliminary theoretical investigation of DMMP adsorption on different phthalocyanines was performed using semi-empirical HF method. The simulations were performed for one molecule of various MPcs (CuPc, ZnPc FePc, and PbPc) with one DMMP molecule. The Pcs were chosen in a way to cover a broad range of the electronegativity of the central atom (see Table 5.2). First, single molecules were relaxed (Figure 5.10). Next, the minimum energy geometries of MPc/DMMP interacting system were searched.

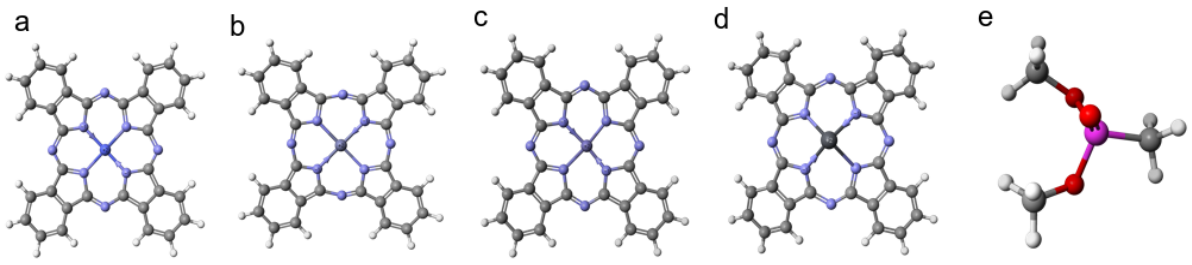

Figure 5.10. Initial structures used in Hartree-Fock semi-empirical simulation: a: CuPc, b: ZnPc, c: FePc, d: PbPc, e: DMMP

In order to find minimum energy conformers, the relaxation of phthalocyanine/DMMP systems was performed using PM6 method for different positions of DMMP molecule on top of the Pc molecule. Figure 5.11 shows final structures with minimum energy. It was found that DMMP

preferably reacts with the phthalocyanine by P=O bond. Since that bond occurs in sarin, it confirms that phthalocyanines are good materials for sarin detection. However, the interaction is not the same for all phthalocyanines. In case of CuPc DMMP does not form a chemical bond with the phthalocyanine. In contradiction, for the ZnPc, the covalent bond is formed between P=O and Zn atom. In the case of FePc and PbPc one can observe the decomposition of DMMP molecule and formation of chemically bonded species.

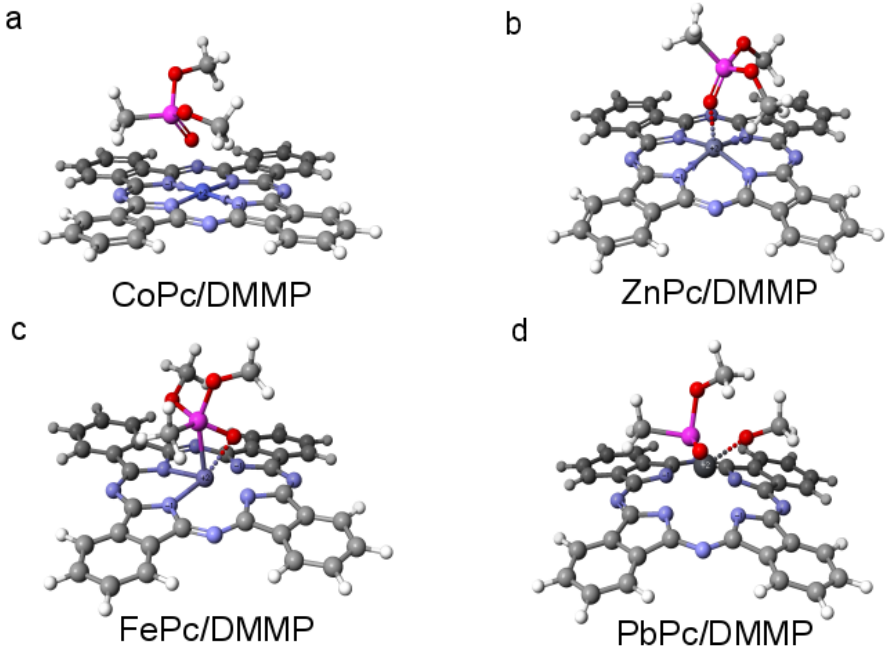

Figure 5.11. Results of semi-empirical modeling of the interaction of one DMMP molecule with: a: CoPc, b: ZnPc, c: FePc, d: PbPc

Adsorption energies of DMMP molecule were determined as a basic parameter that characterizes the interaction of a gas with a sensing structure. Estimated adsorption energies (Table 5.2) indicate that DMMP does not adsorb on CuPc. However, it has to be remembered that PM6 method fails for the description of nonconvalent interactions, such as dispersion interactions and H-bonding and the values of energies for this type of adsorption are highly underestimated (see section 4.1.1). It means that DMMP probably adsorbs on CuPc only through weak vdW interaction. The values of adsorption energies for other MPcs indicate that DMMP strongly chemisorbs on FePc and PbPc, what is a favorable interaction if one wants to enhance the sensor response and the reversibility is not a key issue. The most interesting among investigated materials is ZnPc. Results of semi-empirical modeling show that DMMP adsorbes on this material by much weaker chemical interaction compared to FePc and PbPc what gives an opportunity to obtain easier reversibility and low work temperature for a sensor of relatively high sensitivity.

Table 5.2. Adsorption energies calculated by semi-empirical method for DMMP interaction with MPcs (CoPc, ZnPc, FeP, PbPc)

Structure	E_{ad}, eV	Electronegativity of the central atom
CuPc	0	1.90
ZnPc	-0.78	1.65
FePc	-4.34	1.83
PbPc	-3.47	2.33

5.2.2 Semi-empirical modeling of DMMP adsorption on MoO_3 substrate

In the Introduction to this thesis the possible advantages of hybrid sensing structures based on SMOs and Pcs were indicated. According to the literature, MoO_3 was chosen as SMO substrate for ZnPc deposition. In order to further support this choice, the semi-empirical modelling of MoO_3 interaction with DMMP was performed. Additionally, the adsorption of DMMP on the most common SMO used in gas sensing, SnO_2 was modelled and the results obtained for both oxides were compared.

In order to model the SMOs surfaces, cluster approach was used as in case of PdO and Pd. The proper clusters were chosen again in a way to ensure the sufficient dimensions for the adsorption of one DMMP molecule – for SnO_2 surface, Sn_3O_8 cluster and for MoO_3 surface, Mo_3O_9 cluster – both saturated with hydrogen atoms (Figure 5.12 a and b).

The minimum energy conformers, were found again by the relaxation of SMO/DMMP using PM6 method for different positions of DMMP molecule on the SMO cluster. Figure 5.12 c and d show final structures with minimum energy. It was found that DMMP interacts with MoO_3 by a covalent bond formed between P=O and Mo atom with E_{ads}=-2.6 eV. In case of SnO_2, one can observe the decomposition of DMMP molecule and creation of chemically bonded species with a high E_{ads}=-9.0 eV. These results confirm that MoO_3 could be potentially sensitive to DMMP and given the much lower adsorption energy compared to SnO_2, is preferable from the point of view of work temperature and reversibility.

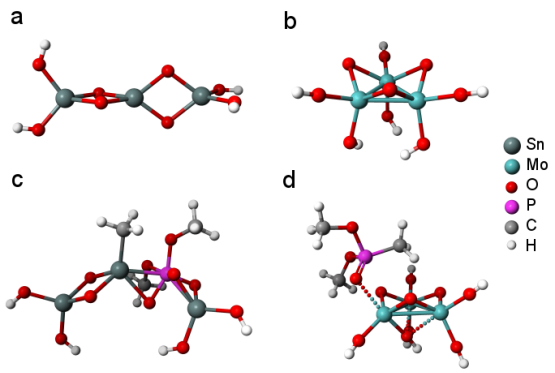

Figure 5.12. a: MoO_3, b: SnO_2 clusters used form semi-empirical modeling of DMMP adsorption and the most stable adsorption geometries for c: MoO_3/DMMP, d: SnO_2/DMMP systems

5.2.3 DFT study of DMMP adsorption on ZnPc

DMMP adsorption on single ZnPc molecule

For the most perspective sensor material, ZnPc, the computational study of DMMP adsorption was extended using DFT approach. The application of this modeling method gives opportunity to take into account vdW interaction, the periodic boundary conditions of the surface and to investigate the influence of a gas on the sensor material's electronic structure.
First, the stable structures of DMMP molecules adsorbed on single ZnPc molecule were determined. This step was undergone by probing a huge variety of possible starting configurations for DMMP with respect to the ZnPc and calculating the adsorption energy of each structure. The considered starting structures included different possible spatial, rotational and relative registries of DMMP with respect to the ZnPc. The stable structures of DMMP on ZnPc can be categorized into three groups. To simplify their characterization, long axis (LA) was defined for ZnPc molecule and oxygen and carbon atoms in DMMP molecule were labeled with subscript indexes 1 and 2 (Figure 5.13).

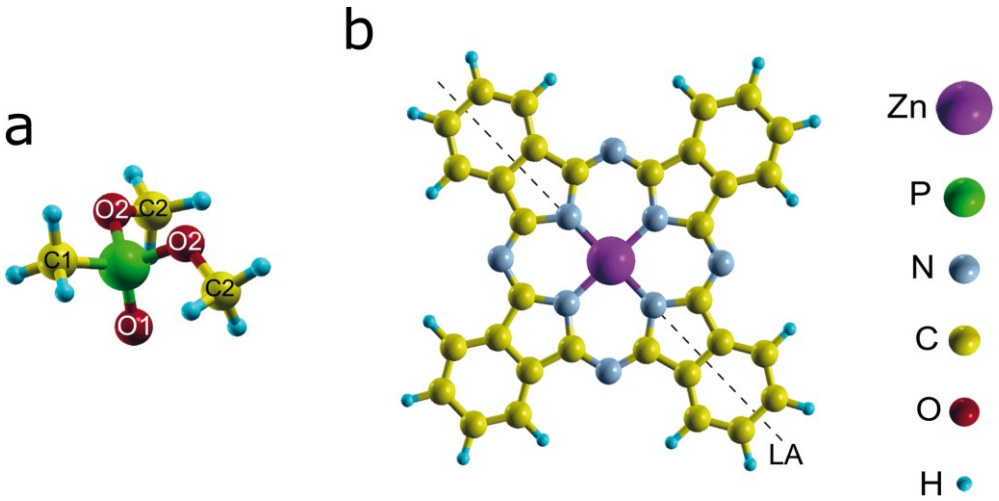

Figure 5.13. Schematic representation of a: the dimethyl methylophosphate (DMMP) and b: ZnPc. On DMMP, the non-equivalent carbon\oxygen atoms are labeled as C1\O1 and C2\O2. On ZnPc, the dashed line marks a long molecular axis (LA).

In category A (Figure 5.14a), a covalent bond is formed between the zinc atom from ZnPc and the reactive O1 atom from DMMP. In category B (Figure 5.14b), a covalent bond is formed between an O2 atom and the Zn atom in ZnPc. Finally, in category 3 (Figure 5.14c), the adsorption of DMMP is dominated by the vdW forces with no indication of a covalent bond between DMMP and ZnPc. The calculations showed that categories B and C are less stable than category A by about 0.2 and 0.56 eV, respectively. These categories are therefore of minor relevance compared to category A at room temperature or above.

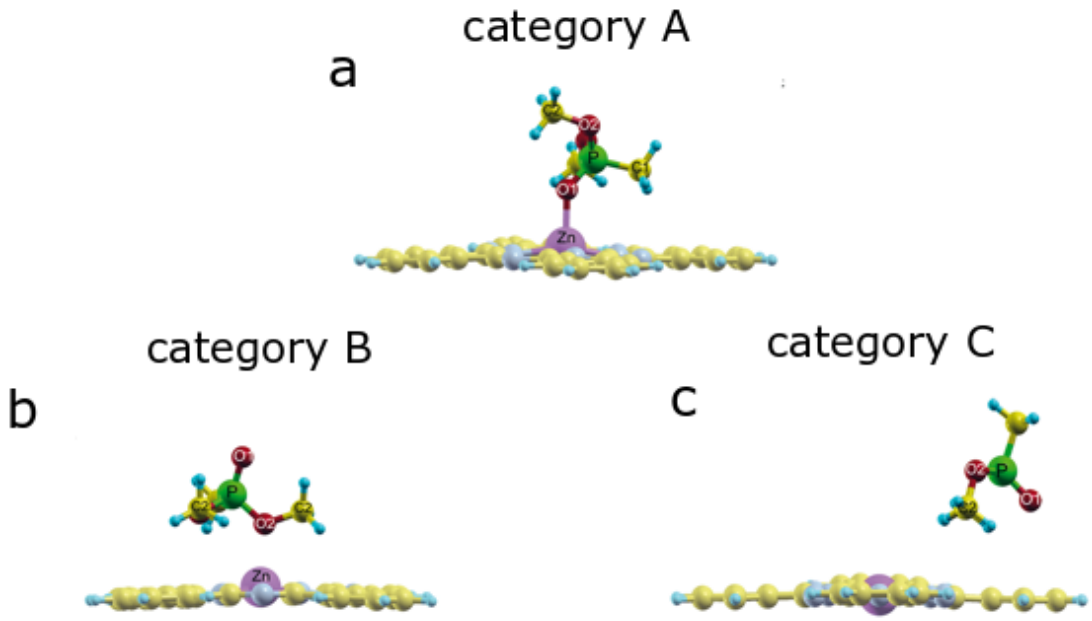

Figure 5.14. Side-views of the different calculated stable structures of DMMP on ZnPc denoted as categories depending on a the type of the formed bond.

In order to describe the adsorption geometry of DMMP on ZnPc in category A, the following parameters were defined (see Figure 5.15):

- O1-Zn distance denoted as *r*,
- the upward movement of the central Zn atom denoted (*d*),
- the angle Zn-O1-P (α) and
- the angle between C1-P and the molecular long axis (LA) denoted as θ, where it describes the azimuthal orientation of DMMP with respect to ZnPc.

Because of the flexibility of DMMP molecule, there is no unique stable structure in category A, but a set of stable and less stable configurations which differ in the values of α *and* θ. In the most stable structure (S-type), DMMP adsorbs on ZnPc by forming a covalent Zn-O1 bond. The adsorption geometry parameters are $r = 2.14$ Å, $d = 0.35$ Å, $\alpha = 140°$ and $\theta = 12°$.

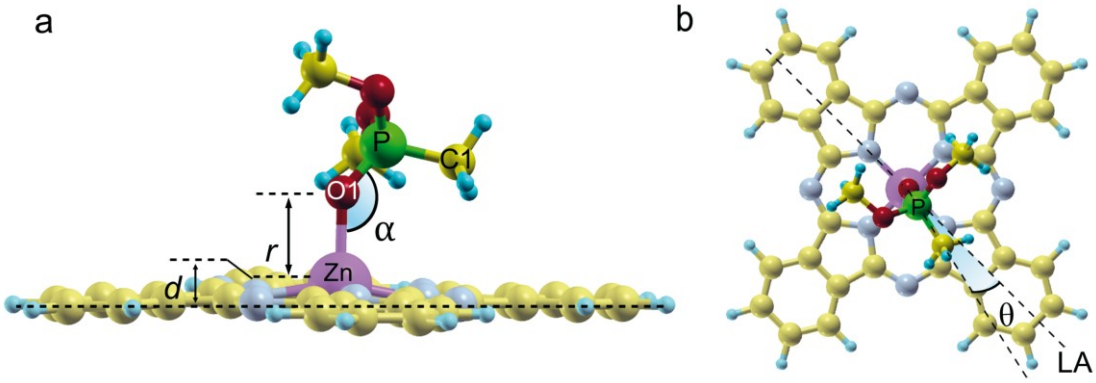

Figure 5.15. a: Top and b: side-views of the most stable adsorption configuration of DMMP on ZnPc. The adsorption geometry parameters are shown: *r* denotes the length of the covalent bond formed between O_1 from DMMP and Zn atom in ZnPc, *d* denotes the upwards movement of the Zn atom, the angle Zn-O1-P denoted as *α,* and the angle between ZnPc long axis (LA) and the C1-P from DMMP given by θ.

Since other local minima in category A are less stable than S-type, they are denoted as less stable structure 1, 2 and 3. To describe the geometries of these structures, the parameters *r*, *d*, α and θ were employed again. The calculations showed all less stable structures have the same values of *d* (0.35 Å) and *r* (1.67 Å) as the most stable structure, but they differ in the values of α and θ (see Figure 5.16 and Table 5.3). In less stable structure 1 (see Figure 5.16), the P, O1 and the Zn atoms are situated almost on a vertical line (α = 176°). Compared to S-type, the methyl group which includes the C1 atom is now pushed upwards while those including the C_{II} atoms are shifted downwards. The energy of this structure is 25 meV (i.e., less stable than S-type by 25 meV), while the value of θ is 40°. In the less stable structure 2 (3), the parameters α and θ are 215° (230°) and 45° (0°), respectively. The methyl groups which include the C1 atom are further shifted upwards. The energy of this structure is 27 (86) meV (see Figure 5.16 c, d and Table 5.3).

As a result of above discussion, the most stable structure in category 1 (S-type) 1 was chosen for the further investigation as the most stable conformation. Adsorption energy of DMMP on ZnPc for the most stable structure was determined as 0.92 eV with dispersion interactions contribution of 0.45 eV.

Table 5.3. Calculated total energies (E) of different less stable structures within category 1, referenced to the most stable structure (S-type). The geometrical parameters (*r*, d, α and θ) are defined in Figure 8.16.

Structure	E (meV)	r (Å)	α (°)	θ (°)
Most stable structure (S-type)	0	2.14	140°	12°
Less stable structure 1	25	2.14	176°	40°
Less stable structure 2	27	2.14	215°	45°
Less stable structure 3	86	2.14	230°	0°

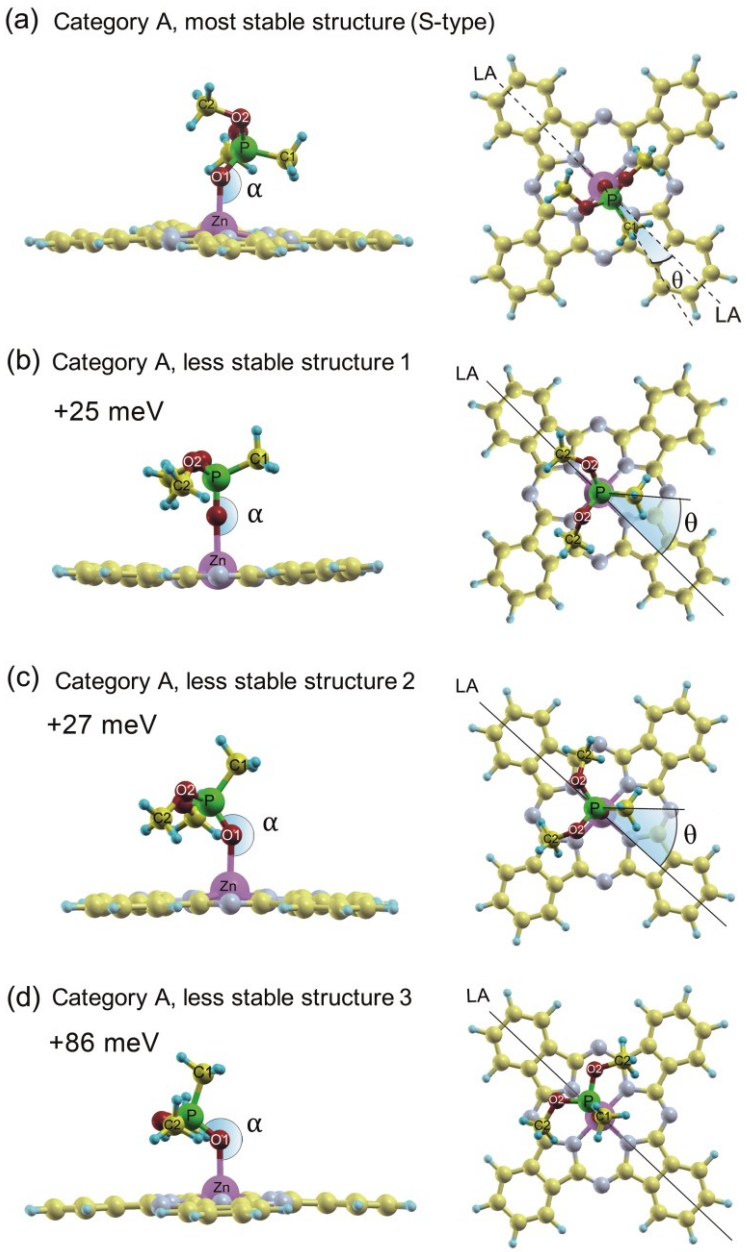

Figure 5.16. a-d Top and side-views of the stable structures of DMMP adsorbed on ZnPc in the category 1. (a) The most stable structure. The other less stable structures are labelled as 1 (b), 2 (c) and 3 (d).

DMMP adsorption on various transition metal phthalocyanines

The adsorption energy of DMMP on ZnPc obtained from DFT calculations was compared with the adsorption energies for different transition metal phthalocyanines (NiPc, CuPc, CoPc) commonly applied in experimental and theoretical investigation of reducing gases sensors[234]. The preliminary study of DMMP adsorption on MPcs that was performed by PM6 semi-empirical method has taken into account CuPc. It was clearly demonstrated that PM6 method is not suitable for calculating the adsorption energy of this structure, because it neglects the dispersion interaction of CuPc with DMMP. For this reason, DFT methods with dispersion interaction should be employed to compare different transition metal Pcs. The most stable

conformation obtained for ZnPc was used as an initial structure for relaxation with various central atoms. The final structures after relaxation and corresponding adsorption energies are presented in the Figure 5.17 and Table 5.4 respectively. The adsorption of DMMP on NiPc, CuPc and CoPc takes place mostly through dispersion interaction. The binding energies are 3-4 times lower than for ZnPc. The order of adsorption energy values is as follows: ZnPc > CoPc > CuPc > NiPc, what is in accordance with DFT study for other reducing gas, NH_3[34]. The explanation of this order of binding energies was given in[34] for NH_3 basing on the MPcs interaction with strong ligands. The study of this interaction by Liao *et al.*[248] revealed strong sensitivity of $a_{1g}(d_{z2})$ and $e_g(d_{xz}, d_{yz})$ MPcs orbitals. Among investigated MPcs, CoPc has half-filled d_{z2} orbital, enabling electron donor to bind the central metal. NiPc and CuPc exhibit the lowest adsorption energies, because their d_{z2} orbital is filled. The strong adsorption on ZnPc with filled d_{z2} orbital is attributed to the changes in the ZnPc geometry while interacting with the ligand. The Zn atom with filled d_{x2-y2} orbital pointing to nitrogen atoms is displaced out-of plane in order to stabilize in a 5-coordination structure.

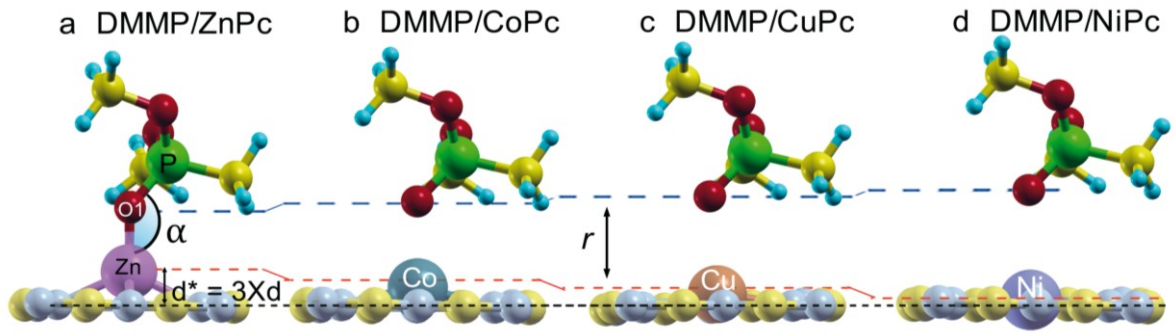

Figure 5.17. Schematic representation of the most stable geometries of DMMP on a: ZnPc, compared with those on B: CoPc, C: CuPc, D: NiPc (only the central parts of MPcs are shown.

Table 5.4. Calculated adsorption energies and geometry parameters of DMMP on different MPcs (E_{ads}).

Structure	**E_{ads} (eV)**	**Dispersion energy in eV (contribution to E_{ads} %)**	***d* (Å)**	***r* (Å)**
ZnPc	-0.92	-0.45 (49%)	0.35	2.14
CoPc	-0.80	-0.52 (65%)	0.15	2.23
CuPc	-0.51	-0.45 (88%)	0.09	2.46
NiPc	-0.42	-0.40 (95%)	0.01	2.80

DMMP adsorption on ZnPc monolayer

In the gas sensor, ZnPc can be deposited on the various substrates as a monolayer or multilayer film. However, the gas adsorption first takes place on the top layer of the sensing structure surface. To evaluate mechanism of DMMP adsorption on the ZnPc surface, a monolayer was considered as a representative structure of the Pc sensing layer.

The first step in this part was the optimization of the ZnPc monolayer. Basic parameters to optimize were dimensions (*a* and *b*) and angle (γ) of the oblique unit cell. To reduce the computational cost, approximated angle from the literature experimental data for ZnPc monolayer on gold was assumed (γ=85 °)[249]. The value for the monolayer on gold was chosen, because gold-organic interfaces are typical examples of weakly interacting interfaces[250]. Given the Pc molecular structure, the second assumption was made - *a* and *b* unit cell parameters were considered equal (hereafter, the unit cell parameter will be labeled as *a*) (Figure 5.18a).

For the given γ and fixed supercell height, ZnPc molecule was relaxed in the unit cells with different *a* (from 6.5 Å to 15 Å). Three local minima were found. They were a result of three various final geometries of molecules in the monolayer (Figure 5.18b):

I. planarly oriented flat molecules – monolayer type I with minimum at 14 Å
II. planarly oriented distorted molecules – monolayer type II with minimum at 12 Å
III. out of plane molecules – monolayer type III with minimum at 7.5 Å

The closer Pc molecules come to each other, the stronger are the intermolecular interactions leading to reorientation and molecular deformation. As a consequence, interacting molecules tend to stack out of molecular plane when their distance decreases.

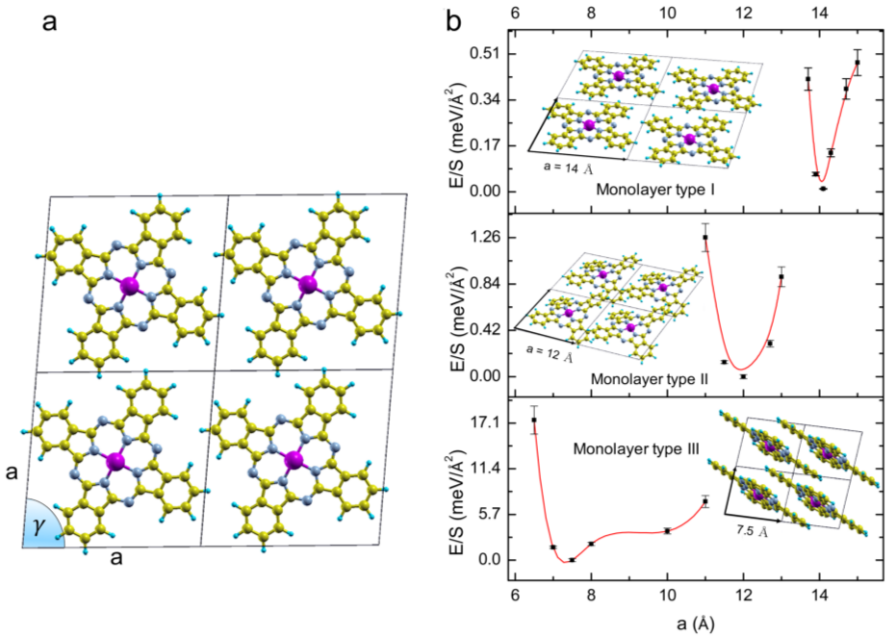

Figure 5.18. a: A schematic representation of a monolayer of ZnPc with dimensions a and γ (shown here for a =14 Å and γ=85°). b: Calculated energy/area (S) curves for the three types of ZnPc monolayers. The energy of most stable structure of each monolayer type is considered as an energy reference (0 eV). A perspective-view of the geometries corresponding to each energy-minimum structure is shown on the side panel.

The monolayer structures obtained above were used to study the adsorption of DMMP. The stable structures are shown in Figure 5.19. As it was presented for the isolated ZnPc molecule, DMMP tends to interact with the metal atom in the center of the Pc. It makes monolayers of type 1 and type 2 more predestinated for DMMP sensing than monolayer of type 3, because of the higher adsorption sites availability. In the case of type 3 monolayer, DMMP molecules can adsorb on the ZnPc's surface created by edges of the molecules (see Figure 5.19f). Therefore, the strong chemical bonding is less probable favoring the van der Waals interaction. (see Figure 5.19e).

Compared to the adsorption on single ZnPc molecules (S-type), the adsorption of DMMP molecules on monolayers of type I and II slightly enhances their stability by about 20 and 10 meV, respectively (see Table 5.5) and only slight variations of the adsorption geometry are observed: θ is now about 0° while r and d as well as α have been barely changed. This means that the sensitivity per DMMP molecule is rather stable. For the type-III monolayer, which does not allow for covalent bonding, adsorption energy is four times lower than for structures with covalent bonding.

.

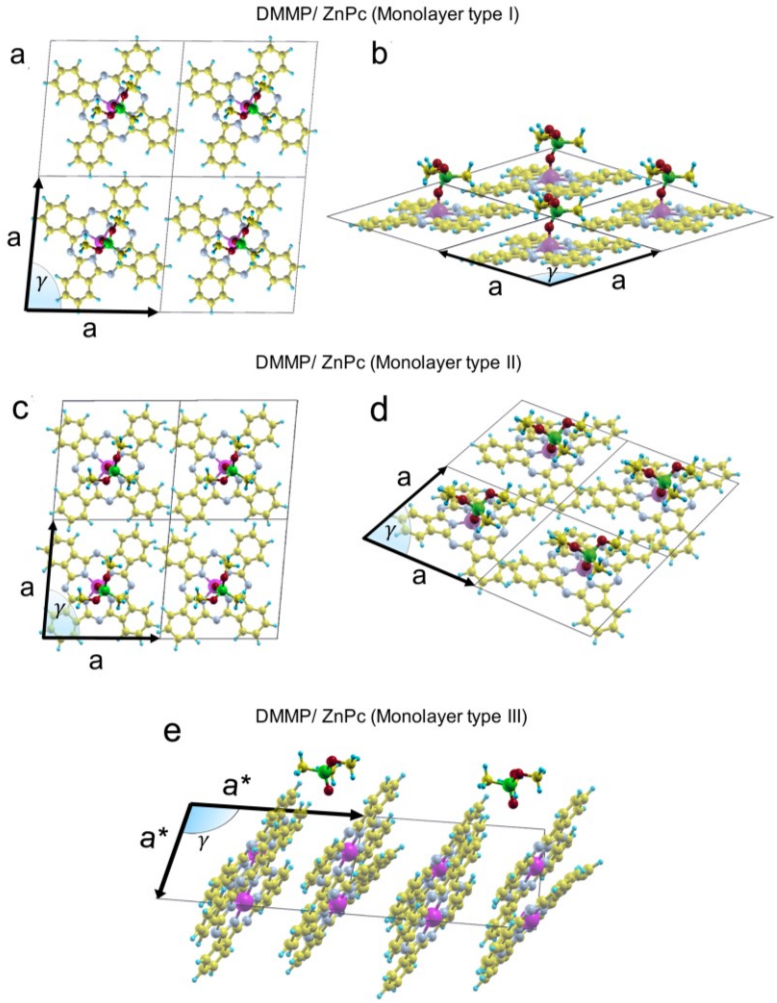

Figure 5.19. a/b and c/d Top/perspective views of DMMP adsorbed on ZnPc monolayers of types I and II. For the dimensions of the unit cells, see text. e: A perspective view of DMMP adsorbed on ZnPc monolayers type III. The dimensions of the unit cell are twice like that shown in Figure 4 (a* = 2a) so that the dimensions of the unit cell are closed to those of monolayers types I and II.

Table 5.5. Calculated adsorption energies and geometry parameters for DMMP molecule on isolated ZnPc and in the various monolayer configurations.

DMMP adsorbed on	E_{ads} (eV)	d (Å)	r (Å)	α (°)
Isolated ZnPc molecule	-0.92	0.35	2.14	140
ZnPc monolayer type I	-0.94	0.35	2.14	140
ZnPc monolayer type II	-0.93	0.33	2.15	139
ZnPc monolayer type III	-0.38	—	-—	—

DMMP adsorption on ZnPc double-stack

Besides adsorption energies, other parameters like charge transfer and/or dipole layers are related to the sensing performance and the mechanism behind[105]. Since DMMP interacts rather strongly with ZnPc forming a covalent bond, charge relocation at the interface can be important factor in DMMP detection by ZnPc.

To analyze the charge transfer in the sensing structures that are based on phthalocyanine multilayers, it is important to consider adsorption on a double ZnPc stack as a simplified model of multilayered ZnPc configuration. For this purpose, ZnPc double stack was first optimized. To optimize the structure of ZnPc double-stacks, different stacking possibilities were tested. The angle between the long axis (LA) of both stacking molecules was considered as a reference for the molecular orientation (φ) while the relative lateral distance (m) between the Zn atoms was taken as a reference for the molecular registries. The calculations showed two energy minima. A local energy minimum was obtained for parallel planes of both ZnPc molecules, but with a tilting angle $\varphi = 45°$ (see Figure 5.20a). In the global minimum (energetically more stable by 0.26 eV), the LAs of both molecules are parallel to each other ($\varphi = 0°$). However, their centers are laterally shifted by $m = 1.32$ Å, and vertically separated by 2.92 Å (see Figure 5.20b). Denoted as slipped-stack packing, this way of crystallization is commonly known for phthalocyanines[251,252]. Again, the DMMP adsorption geometry (see Figure 5.20 c and d), exhibits no significant changes compared to these related to the S-type. The adsorption energy for this structure equals -0.89 eV. Is is around 30 meV less stable than for the single ZnPc molecule.

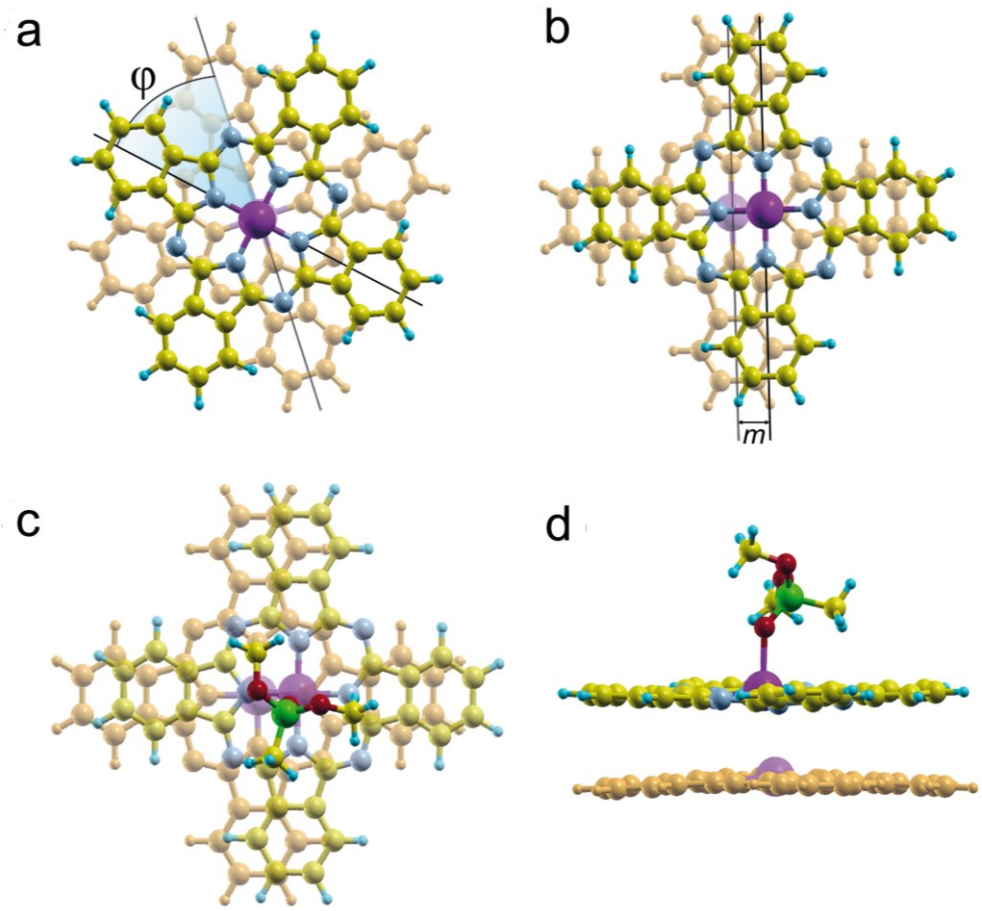

Figure 5.20. Top-views of ZnPc double layers in the a: energetically local minimum and b: global minimum structures. The lines indicate the long axes of the molecules, the parameter *m* indicates the relative lateral shift between the Zn atoms in the stacked molecules, while φ indicates the relative azimuthal orientations of stacked molecules. c: Top-view and d: side views of DMMP adsorbed on double-stacked ZnPcs in its most stable structure.

Charge transfer between DMMP and ZnPc

Since DMMP is covalently bonded with ZnPc, one can expect the charge relocation that directly influences sensor performance. Löwdin analysis was performed to evaluate amount and direction of this charge transfer. Results of this analysis for single molecules showed electrons relocation from DMMP to ZnPc as expected for a reducing gas. Mean value of net charge transfer was around 0.3 e per molecule. The charge depletion was uniformly distributed on all DMMP atoms, but mainly from the region between P-O1 atoms. For the ZnPc molecule electrons are accumulated at the center of the ZnPc molecule, at the Zn atom as well as in the region between the Zn and the attached O1 atom. The other part of the ZnPc molecule undergoes a polarization effect. Thereby, a slight charge accumulation on the inner nitrogen atoms by 0.08 e and a depletion of 0.05 e on the outer ones were calculated. On carbon atoms, the calculations showed a total charge accumulation by about 0.2 e. For monolayers type I and type II there are no significant changes in the charge transfer with respect to the isolated ZnPc molecule. Table 5.6 summarizes charge transfer between DMMP and ZnPc molecules. It is important to note that the calculated charge distribution does not change considerably upon interacting with

monolayers of types I and II, which again confirms the conclusion that forming monolayers of ZnPc barely influences the interaction between DMMP gas particles and ZnPc as long as the interaction is mediated by covalent bonding. As it was mentioned in the previous section, the most important for a gas sensor based on multilayered phthalocyanine is a charge relocation between Pc layers. Results of a charge transfer investigation for DMMP-double ZnPc system revealed that the amount of a charge transferred from DMMP to ZnPc is the same as for a single ZnPc molecule. However, the most important finding was a very small charge transfer between ZnPc layers - 85 % of charge accumulated on top ZnPc molecule, 15 % on the bottom one (Table 5.7). As a consequence, the DFT analysis indicates the formation of a surface dipole layer as a main ingredient of the sensing mechanism. The latter will be verified experimentally as it will be shown in next section.

It has also to be mentioned that the sensing material is further deposited on MoO_3. While the computational resources available within this thesis did not allow for the atomistic modelling of the complete system, the approximation of a possible electron transfer across the second interface by considering charged models for DMMP+ZnPc with additional net charges up to ± 2 e was performed. The calculations showed that, irrespective of the sign and value of the net charge, the extra charge completely distributes on deeper ZnPc without changing the induced dipole layer considerably. In other words, the secondary interface might induce some modification of the Fermi level of the system of DMMP adsorbed on ZnPc, but the induced surface-layer dipole turns out to be very robust against recharging.

Table 5.6. Results of charge transfer analysis between DMMP and ZnPc single molecule and monolayers (negative values mean electrons depletion and positive values mean electrons accumulation)

Molecule	**Δq (e)**	**Δq per atom type (e)**				
ZnPc single molecule						
DMMP	-0.19					
ZnPc	0.35	Zn	N inner	N outer	C	H
		0.08	-0.08	0.05	0.25	0.04
ZnPc monolayer type I						
DMMP	-0.19					
ZnPc	0.35	Zn	N inner	N outer	C	H
		0.08	-0.1	0.05	0.3	-0.02
ZnPc monolayer type II						
DMMP	-0.16					
ZnPc	0.34	Zn	N inner	N outer	C	H
		0.08	-0.075	0.05	0.25	0.05

Table 5.7. Results of charge transfer analysis for the DMMP-ZnPc double-stack system

Molecule	**Δq (e)**	**Δq per atom type (e)**				
ZnPc double-stack						
DMMP	-0.16					
ZnPc top	0.294	Zn	N inner	N outer	C	H
		0.06	-0.09	0.05	0.25	0.05
ZnPc bottom	0.052	Zn	N inner	N outer	C	H
		-0.01	-0.02	0.01	0.04	0.03

5.2.4 MoO_3/ZnPc surface morphology

In order to study the Pc arrangement in the applied real structures, AFM was employed again. The exemplary AFM images taken for bare MoO_3 layer and MoO_3/ZnPc are shown in the Figure 5.21 a and b respectively. As the measure of roughness the RMS of roughness parameter was calculated for all the samples. In case of MoO_3, the RMS was equal 1.58 nm while for MoO3/ZnPc RMS was determined as 6.41. The active surface was determined as 1.002 μm^2 and 1.021 respectively (see Table 5.8). The values for the structure with Pc correspond to the moderately developed surface. However, looking at the topography images one can observe areas of bigger topographical feauters, reaching nearly 25 nm. The surface exhibist developed number of topography – related adsorption sites. The uncovered parts of MoO_3 surface can adsorb either the impurities from ambience (H_2O or carbon species) or create additional sites for DMMP adsorption. On the oder hand, as it was demonstrated from DFT calculations, the well-ordered very thin Pc layers are required to enhance the sesitivity to DMMP. Since the obtained Pc layers are disordered and not equally distributed on the substrate, one can expect significant contribution of vdW interactions to the structres' responses to DMMP. However, there can be a number of adsorption sites available also for the covalent bond between Zn atoms and DMMP.

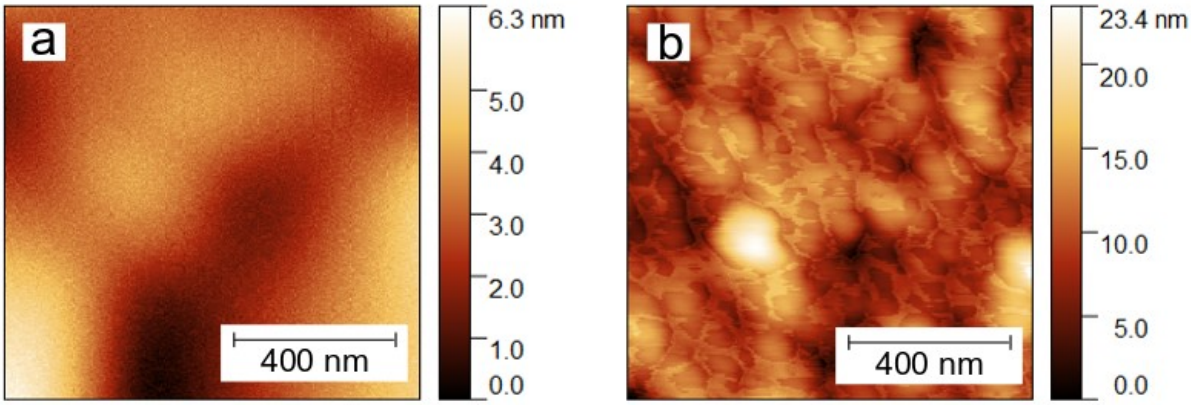

Figure 5.21. The AFM topography images (1 μm x 1 μm) of a: bare MoO_3, b: MoO_3/ZnPc structures' surfaces

Table 5.8. RMS parameters of roughness and active surfaces of MoO_3 and MoO_3/ZnPc surfaces determined from AFM topography images.

	MoO_3	**MoO_3/ZnPc**
RMS, nm	1.58	6.41
Active surface, μm^2	1.00225	1.02082

5.2.5 MoO_3/ZnPc surface chemical and electronic structure

Following the simulations, the experimental confirmation of the above findings was performed by means of XPS and UPS techniques. Figure 5.22a – d presents the set of high-resolution XPS regions recorded for pristine ZnPc (bottom row) and DMMP – exposed (upper row) samples. As the matter of fact, the DMMP adsorption shall be discussed as first. Making an insight into the chemical structure of both: ZnPc and DMMP molecules it is clear that the phosphorus existence would be the only reliable indicator of DMMP existence at the ZnPc surface. Figure 5.22a shows the comparison of P 2p region and as one can see in case of pristine sample there is no distinct signal indicating phosphorus presence at all. Following, for the DMMP – exposed sample the slight rise of the signal is present at ~130 eV (binding energy, decomposed into $2p_{1/2}$ and $2p_{3/2}$ signals as points spin – orbit splitting of the P 2p) which is consistent with the literature position of the P 2p energy level. However the intensity of the signal is extremely weak, with this result one can confirm the adsorption of the DMMP at the sample's surface with a relatively low coverage.
Next, the chemical composition was checked by detailed analysis of the C 1s, Zn 2p and N 1s energy regions. Figure 5.22b presents decomposition of the C 1s energy region. The decomposition of the region revealed signals which could be assigned to C-C and C-N signals accompanied with their respective satellites[247]. No other signal was introduced to the spectrum due to following assumptions: the majority of adventitious carbon signal is incorporated in the tail of the C-C component and the lack of C=P signal is due to extremely weak P 2p intensity. The latter means that the existing C=P component would be at the noise level in the photoemission spectrum taking into consideration difference in relative sensitivity factors of C 1s and P 2p regions. Next, C=P component, due to P atoms electronegativity shall be expected in the vicinity of C-C component, is strongly suppressed by the C-C counterpart. However, one can notice slight increase of the S_{C-N} region.
Following, the Zn $2p_{3/2}$ region was considered. As it can be observed in Figure 5.22d one prominent Zn component is visible showing the stable form of Zn (no additional oxidized states are present). The difference between pristine and DMMP – exposed samples is the chemical shift which is present in case of DMMP-exposed one. Particularly the Zn $2p_{3/2}$ region was shifted by nearly 3 eV towards lower binding energies after the exposure. This would suggest significant electron accumulation in this region. Further analysis made on the basis of N 1s region showed the existence of three components which can be attributed to (starting from lowest binding energy) residual substrate-related Mo $3p_{3/2}$ component, N-C component and N-H component which is a representation of the residual contribution of base-free Pc. Among them, the N-C component is of interest since it is one of the main constituents of the examined ZnPc structure. After energy position analysis it appeared that this component suffers significant shift also towards lower binding energies by 0.8 eV after DMMP adsorption, which is consistent with the direction of Zn $2p_{3/2}$ shift. Although quantitatively the N 1s shift is different than Zn $2p_{3/2}$ (~0.8 eV vs 3.0 eV) the trends correspond to each other in that sense that the pyridine rings experience lower electron accumulation leading to lower detected chemical shift. This finding is of importance in the view of simulation results: particularly it

suggests that the Zn atoms adopts the majority of the incoming from DMMP electrons while the nitrogen atoms are becoming only partially charged upon ZnPc contact with DMMP.

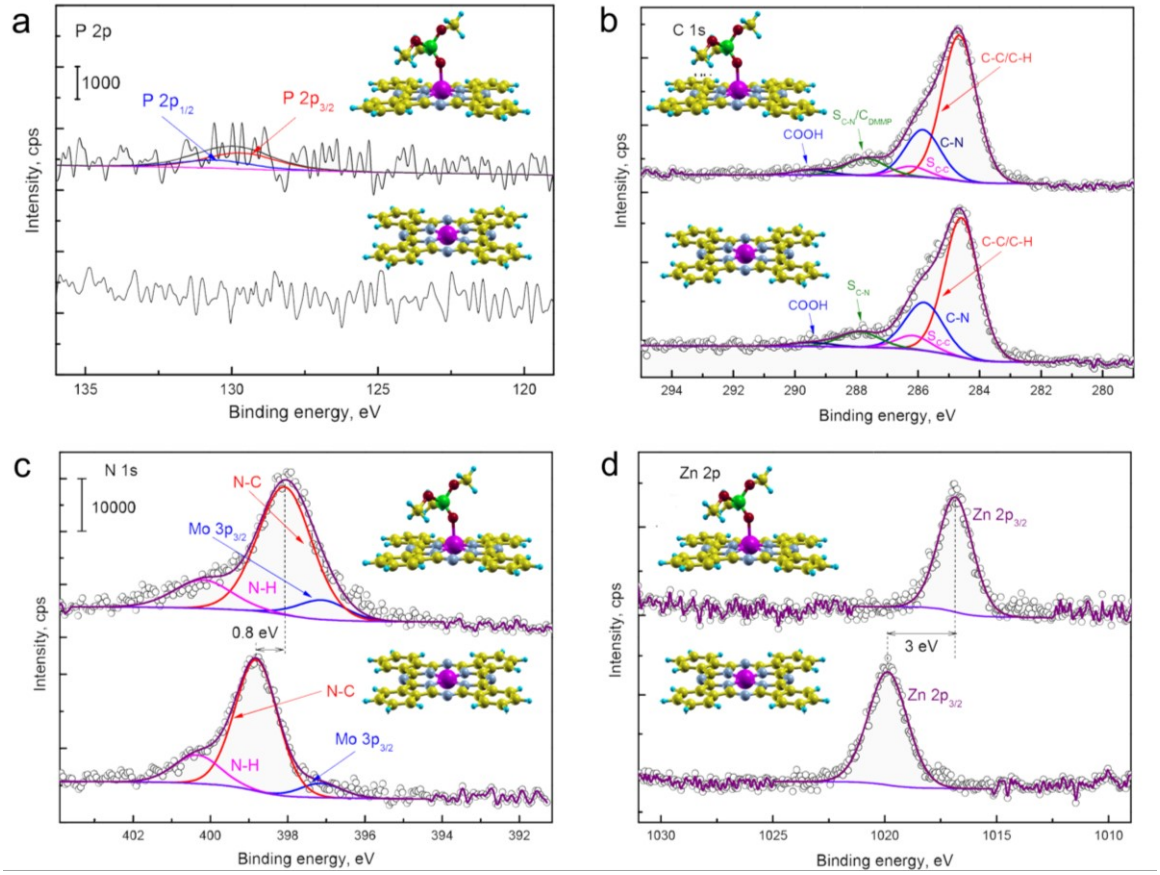

Figure 5.22. High-resolution XPS spectra (a: P 2*p*, b: C 1*s*, c: N 1*s* and d: Zn $2p_{3/2}$) assess the relative shifts of the binding-energies induced in the DMMP–exposed samples (upper panels) compared to the pristine ZnPc samples (bottom panels). A: The P 2*p* signal is decomposed into $2p_{1/2}$ and $2p_{3/2}$ signals. Each of the other recorded energy regions (b-d) has been decomposed into components from non-equivalent constituent atoms. The characteristic shifts in the N 1*s* and Zn $2p_{3/2}$ energy levels in the DMMP-exposed samples have been also indicated.

Following, the hi-resolution UPS measurements were performed. Figure 5.23a presents high energy cut-off recorded for the pristine ZnPc layer as well as for the layer extensively exposed to DMMP. Since the analyzer and the sample were kept at the same potential, the significant shift of the photoemission cut-off signal directly corresponded to the shift of the work function of the sample's surface. Quantitatively, the work function was changed form 3.2 eV for pristine ZnPc (which is in agreement with other literature data[253]) to 5.1 eV upon DMMP exposure. Although the shift of nearly 2 eV seems enormously big, it has to be kept in mind that UPS is purely surface – sensitive method due to relation between kinetic energy of the excited photoelectrons and their attenuation length. Therefore the shift of the surface work function can be interpreted as the confirmation of existence of significant DMMP – induced surface dipole. Which is important, the direction of the work function changes corresponds to shift of the core levels and (even more important) with the direction of the charge relocation obtained from simulation studies. The WF shift towards higher values is a result of the electron depletion. From the theoretical calculations we predicted charge relocation from DMMP to ZnPc. Since we detect mostly WF of the DMMP adsorbate layer, its large increase confirmed that electrons

were transferred from DMMP molecules to the ZnPc, resulting in the surface dipole formation. The summary of the photoelectron spectroscopy results were presented in the energy level-like diagram in Figure 5.23b.

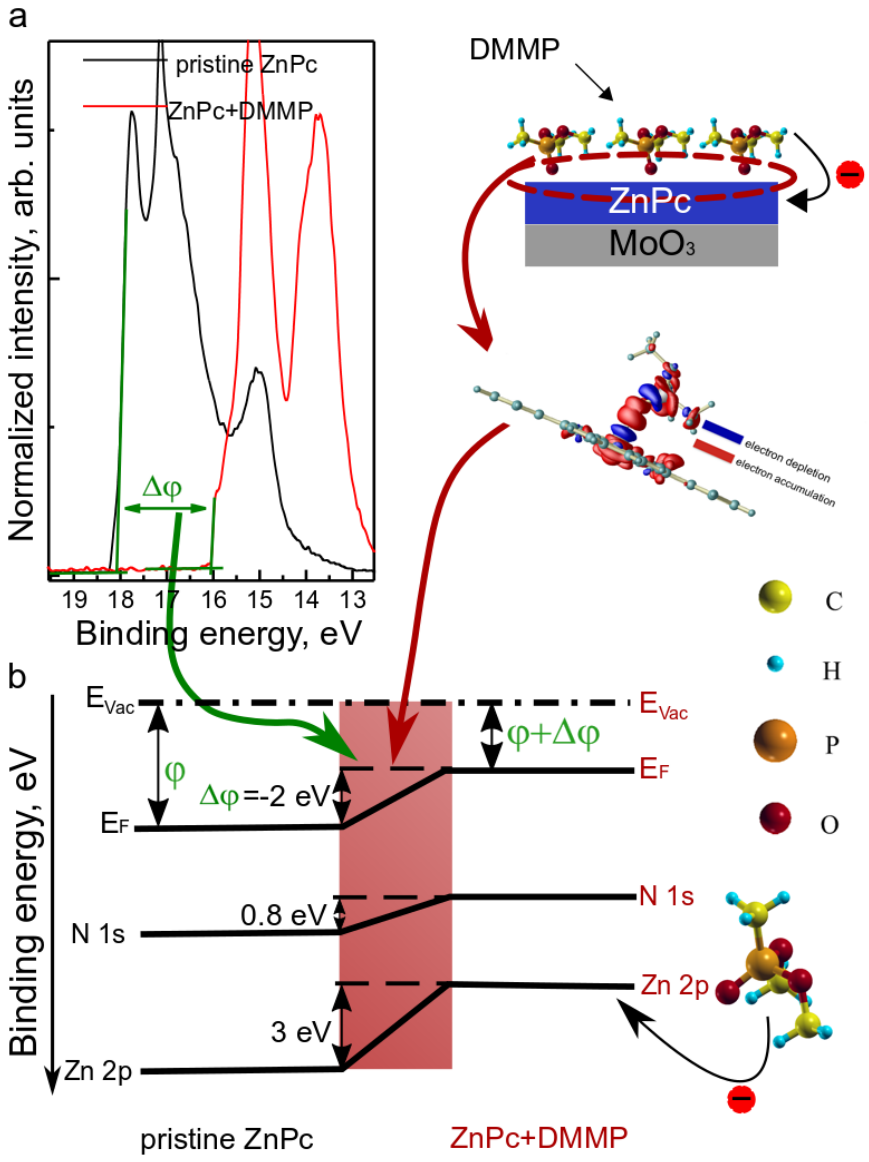

Figure 5.23. Changes in ZnPc Surface electronic structure induced by DMMP adsorption: a) high energy cut-off recorded for the pristine ZnPc layer as well as for the layer exposed to DMMP with work function change indicated as $\Delta\varphi$, b) the summary of the photoelectron spectroscopy results presented in the energy level-like diagram.

5.2.6 MoO_3/ZnPc thermal desorption study

To complement the investigation of the adsorption-desorption processes, the TDS experiment was performed for both - bare MoO_3 layer and MoO_3/ZnPc structure before and after DMMP exposition. Since due to the experimental setup restrictions the measurements had to been carried out for 10 different atomic masses up to 100 amu (see section 4.2.2), it was not possible to detect the DMMP molecule (124 amu). Thus, the following possible products of DMMP decomposition have been chosen based on the literature[51,52,162]: H_2 (2 amu), H_2O (18 amu), CO (28 amu), CO_2 (44 amu), phosphorus (31 amu), PO_3 (79 amu), methyl phosphonate (94 amu), dimethyl ether (46 amu), methyl (15 amu), formaldehyde (30 amu). Additionally, the desorption of water (18 a.m.u.) as a common species adsorbed from the ambience was monitored. The survey TDS spectra for bare MoO_3 and MoO_3/ZnPc structures are presented in the Figure 5.24 a and b respectively.

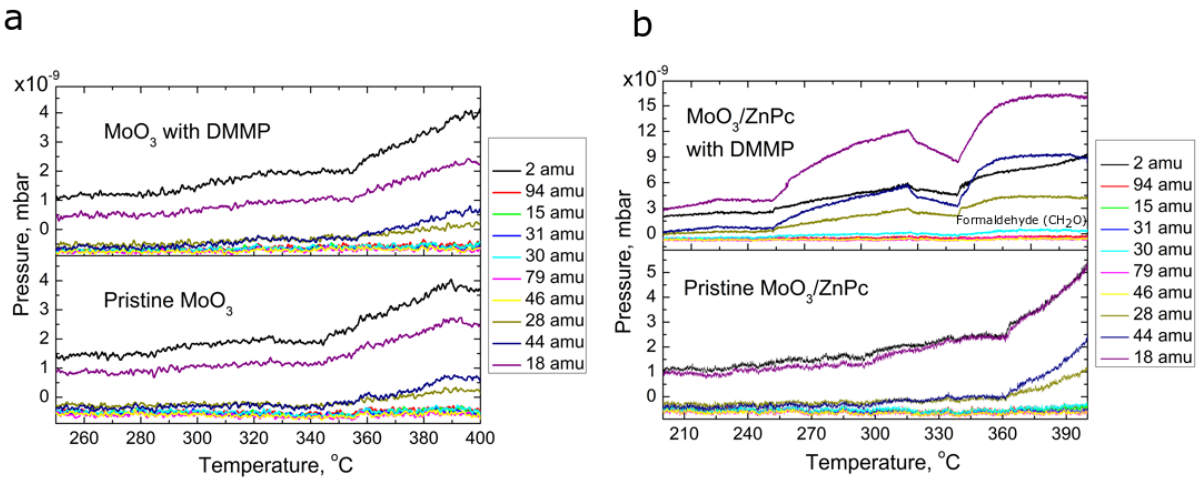

Figure 5.24. The survey TDS spectra for a: bare MoO_3 and b: MoO_3/ZnPc structures

Partial pressure variation during the surfaces' heating revealed peak-features at the spectra with a shape depending on the nature and quantity of the desorbing species. As the DMMP desorption is crucial for this thesis, the spectra of the possible DMMP desorption resulting components should be discussed at first. For the bare MoO_3, the desorption of H_2, CO, CO_2 and H_2O was observed. Although the shapes of the spectra where similar for the pristine and DMMP exposed sample, the more accurate analysis revealed some differences. The H_2O spectra exhibited a main broad peaks with maximum located around 400°C and partial pressure at the level of 10^{-9} mbar that were preceded by other minor (partial pressure at level of 10^{-10} mbar) broad peaks with maximum around 360°C. This characteristics was mimicked by H_2 desorption spectra. The Co and CO_2 spectra also revealed the main peaks with maximum around 400°C for both – pristine and DMMP exposed sample. The only difference between the spectra before and after DMMP exposition was a very slight rise of the signal just before the main peak in the case of DMMP exposed sample. However, as all the detected components were present before and after DMMP exposition and can all be an outcome of ambience impurities adsorption, it cannot be concluded that some of the desorbing species resulted from the DMMP decomposition. On the contrary, for MoO_3/ZnPc structure, beside the desorption of H_2O, H_2,

CO and CO_2, the slight signal of formaldehyde (CH_2O) with a maximum around 375ºC was observed for the DMMP exposed sample and was not present for the pristine one. This result is an indirect confirmation of DMMP adsorption on the ZnPc surface. Moreover, it suggests that DMMP desorbing from the ZnPc was decomposed and one of the products of this decomposition was formaldehyde. The relatively low partial pressure of the desorbing species can be due to the fact that only part of the adsorbed DMMP was covalently bonded to the ZnPc and decomposed in the given range of temperature. The part of DMMP was attached by vdW interactions and desorbed without decomposition at lower temperature. The information about other possible products of the DMMP decomposition among the monitored species can be obtained from the recorded spectra. As the remaining observed components are present also in the pristine sample as the residual species adsorbed from the ambience, the detailed analysis of the spectra had to be performed in order to extract single components. In this purpose, the detected TDS peaks for each species were decomposed applying peak fitting procedure with asymmetrical Gaussian function lines that can be used for the first order kinetics of desorption. This mechanism of desorption was assumed based on the Contour *et al.*[254] first studies of desorption from phthalocyanines. The decomposed spectra (for the desorption windows) of all detected species are presented in the Figure 5.25. The Figure 5.25a shows the spectra of formaldehyde (CH_2O). Four peaks were fitted to the spectrum of DMMP exposed sample – first with the maxima at 265 ºC (1), 299.9 ºC (2), 334.3 ºC (3) and 375.6 ºC (4). For all other species, the slight rise of signal with the maximum around 265 ºC is also visible only for the DMMP exposed sample. This rise is followed by a group of broad peaks with shapes mimicking the formaldehyde spectrum and the maxima around the temperatures of formaldehyde maxima. The last peaks for H_2O, H_2, CO and CO_2 revealed two components as the desorption of those species from the pristine sample also appeared around this temperature. One can notice that for the H_2, H_2O and CO_2 in pristine sample there are peaks at the position of the middle peaks for DMMP exposed sample. However, their maximum partial pressures are almost one order of magnitude lower.

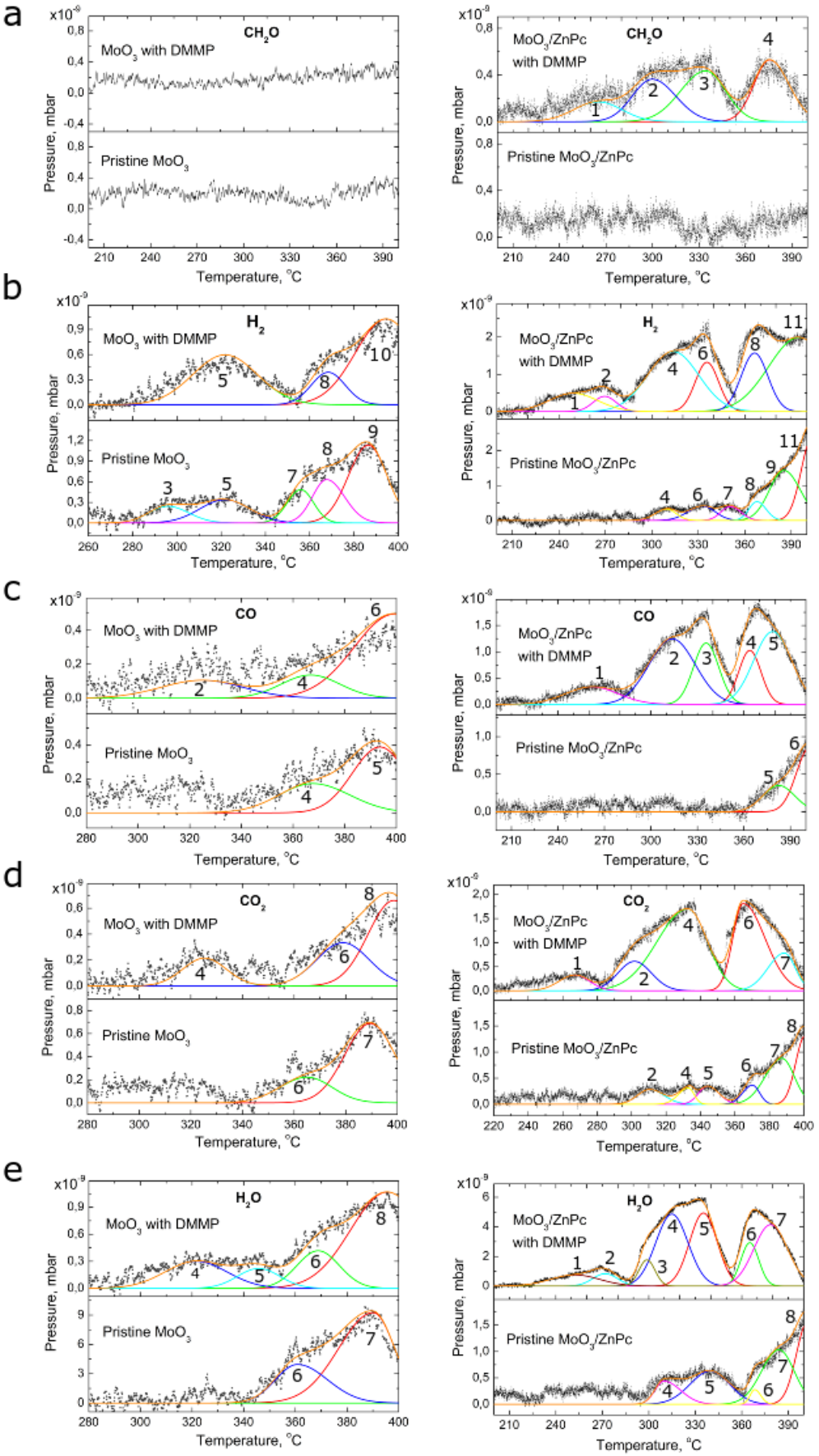

Figure 5.25. The decomposed spectra (for the desorption windows) of bare MoO_3 and MoO_3/ZnPc structure for the following species: a) formaldehyde, b) hydrogen, c) carbon oxide, d) carbon dioxide, e) water.

To complement the above discussion, activation energies for desorption (E_a^d) of all desorbed species were calculated applying Redhead equation (see eq. 4.19 in section 4.2.2). The value of the pre-exponential factor ϑ is often assumed as equal to 10^{13} 1/s. For this value of ϑ and β=0.5 K/min the condition of Redhead formula application (ϑ/β between 10^8 K^{-1} and 10^{18} K^{-1}) was fulfilled (ϑ/β equaled around 10^{15} K^{-1}). All estimated temperatures of peaks maxima with corresponding E_a^d are collected in the Table 5.9. For the present discussion, the most important are the energies for formaldehyde desorbing from MoO_3/ZnPc exposed to DMMP. The desorption activation energy is approximately equal to the adsorption energy. Thus, the experimental values obtained here can be directly compared with the adsorption energies obtained from the theoretical modeling. Obtained set of activation energies indicated existence of more than one binding states within the energy range from 1.7 eV to 2.1 eV that could be assigned to the various surface coverages – the lowest for 1.7 eV and the highest for 1.95 eV. The same trend in coverages was observed for the respective energies for all desorbing species. The obtained values are higher than theoretical DMMP adsorption energy on ZnPc layers (0.9 eV). However, one has to remember that Redhead's method gives only a rough approximation of E_a^d. Moreover, the theoretical value was obtained for ideal system of DMMP adsorbed on ZnPc monolayer in the vacuum. The experiment was performed for the multi-layered ZnPc deposited on MoO_3. The influence of this factor on the desorption process is visible also as the different energy states that can be a result of the desorption from the different depths of the adsorbing layer. Since the ZnPc sample exhibited highly developed surface, the part of DMMP molecules was possibly adsorbed directly on the surface, while other part penetrated deeper into the structure through the structural defects. One has to also remember that studied ZnPc layer is not perfectly ordered, so different adsorption geometries can be formed depending on the preferable adsorption sites availability. For bare MoO_3, any particular peak that could have been assigned to DMMP has been not observed. However, the semi-empirical modeling showed that DMMP adsorption energy on MoO_3 is higher than 2.5 eV. Thus, the desorption of DMMP from MoO_3 could be expected for temperatures higher than 500 °C. Both studied materials adsorb impurities such as carbon species, water and hydrogen from the ambience. Thus, the potential DMMP adsorption sites are partially occupied. However, the partial pressures of the components related to the impurities are relatively low, so although the studied materials adsorb species from ambience, the number of adsorption sites is still available for DMMP.

Table 5.9. Desorption activation energies and relative areas of particular peaks for species desorbing from pristine and DMMP exposed MoO_3 and MoO_3/ZnPc samples. E_a^d and relative areas were calculated from the decomposed TDS spectra.

Desorbing species	No	Pristine MoO_3		MoO_3 with DMMP		Pristine MoO_3/ZnPc		MoO_3/ZnPc with DMMP	
		T, °C	E^a_{des}, eV	T, °C	E^a_{des}, eV	T, °C	E^a_{des}, eV	T, °C	E^a_{des}, eV
CH_2O	1	-		-		-		265.0	1.73
	2							299.9	1.85
	3							334.3	1.96
	4							375.6	2.10
H_2	1	-		-		-		249.3	1.68
	2							266.3	1.75
	3	295.6	1.83					-	
	4	-				309.7	1.88	313.7	1.89
	5	321.7	1.92	321.8	1.92	-		-	
	6	-		-		332.7	1.96	335.6	1.97
	7	356.0	2.03			350.6	2.02	-	
	8	367.6	2.07	368.4	2.07	367.8	2.07	366.3	2.07
	9	386.5	2.13	-		385.2	2.13	-	
	10	-		394.6	2.16	-			
	11					403.6	2.19	394.8	2.16
CO	1	-		-		-		261.9	1.72
	2			319.0	1.91			313.7	1.89
	3			-				335.6	1.97
	4	367.7	2.06	358.5	2.04			363.8	2.06
	5	393.7	2.14			382.5	2.12	378.5	2.11
	6	-		398.3	2.17	402.5	2.19	-	
CO_2	1	-		-		-		267.1	1.74
	2					310.4	1.88	301.7	1.85
	3			324.8	1.93	-		-	
	4			-		333.0	1.96	332.6	1.96
	5					344.2	1.99		
	6	365.1	2.06	366.8	2.07	370.2	2.08	364.7	2.06
	7	389.5	2.14			387.3	2.14	388.7	2.14
	8			399.3	2.18	400.7	2.18		
H_2O	1	-		-		-		252.4	1.69
	2							271.8	1.75
	3							298.8	1.84
	4			321.6	1.92	309.8	1.88	314.9	1.90
	5			345.8	2.00	339.7	1.98	335.2	1.96
	6	360.8	2.05	368.8	2.08	368.3	2.07	365.2	2.06
	7	390.2	2.15			384.0	2.13	378.6	2.11
	8	-		395.6	2.17	402.7	2.19	-	

5.2.7 Sarin adsorption on MPcs – theoretical study

DMMP is a well-known sarin simulant widely used in experimental study of CWA sensors. In most laboratories it is necessary to use a less toxic gas due to the safety requirements. Therefore, there are only few studies comparing sensitivity of investigated materials to DMMP with the sensitivity to sarin. This thesis in the experimental part as most of the research was limited to DMMP. However, the DFT method gives an opportunity to compare the adsorption of DMMP with adsorption of sarin at the theoretical level. Thus, the validity of using DMMP as a sarin model in case of investigated materials can be verified. In this purpose, the modeling of sarin adsorption on single molecule of all MPcs investigated for DMMP by DFT method was performed. To optimize the number of calculations, similarly to the modeling of DMMP adsorption, the most stable structure for ZnPc+sarin was found and compared with other Pcs (NiPc, CuPc and CoPc).

Sarin adsorption on single MPc molecule

The stable structures of sarin molecules adsorbed on single ZnPc molecule were determined as in case of DMMP by probing a huge variety of possible starting configurations. The stable structures of sarin on ZnPc can be categorized into four groups. To simplify their characterization again, the LA was defined for ZnPc molecule and oxygen atoms in sarin molecule were labeled as O1 and O2 (Figure 5.26). Categories A, B and C correspond to the categories with the same labels in case of DMMP. In category A (Figure 5.27a), a covalent bond is formed between the zinc atom from ZnPc and the reactive O1 atom from sarin. In category B (Figure 5.27b), a covalent bond is formed between an O2 atom and the Zn atom in ZnPc. In category C (Figure 5.27c), the adsorption of sarin is dominated by the vdW forces with no indication of a covalent bond between sarin and ZnPc. For sarin there is one more category (see category D in Figure 5.27d) in which a covalent bond is formed between the zinc atom from ZnPc and fluorine atom from sarin.

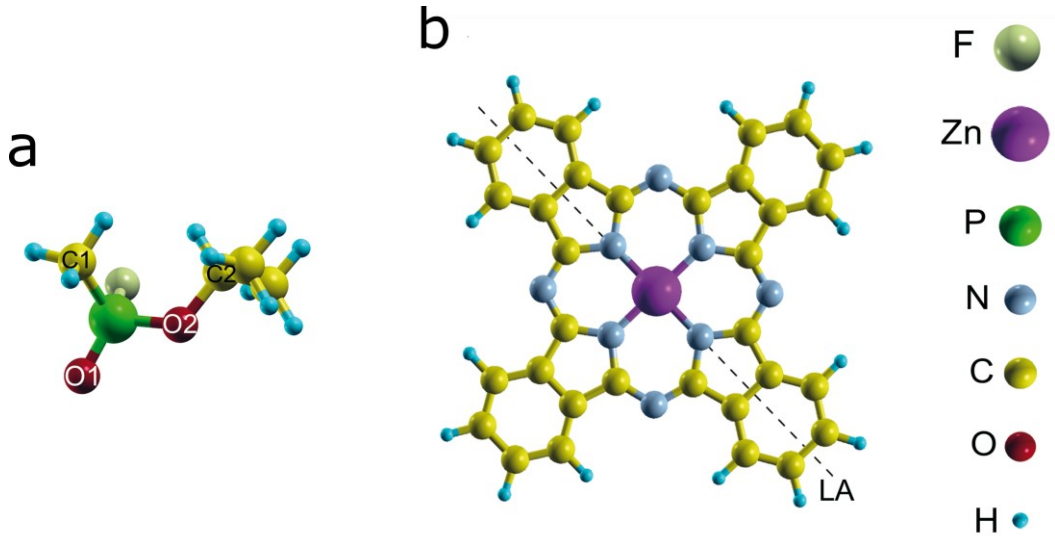

Figure 5.26. Schematic representation of a: the saein and b: ZnPc. On sarin, the non-equivalent carbon\oxygen atoms are labeled as C_I\$O_I$ and C_{II}\$O_{II}$. On ZnPc, the dashed line marks a long molecular axis (LA).

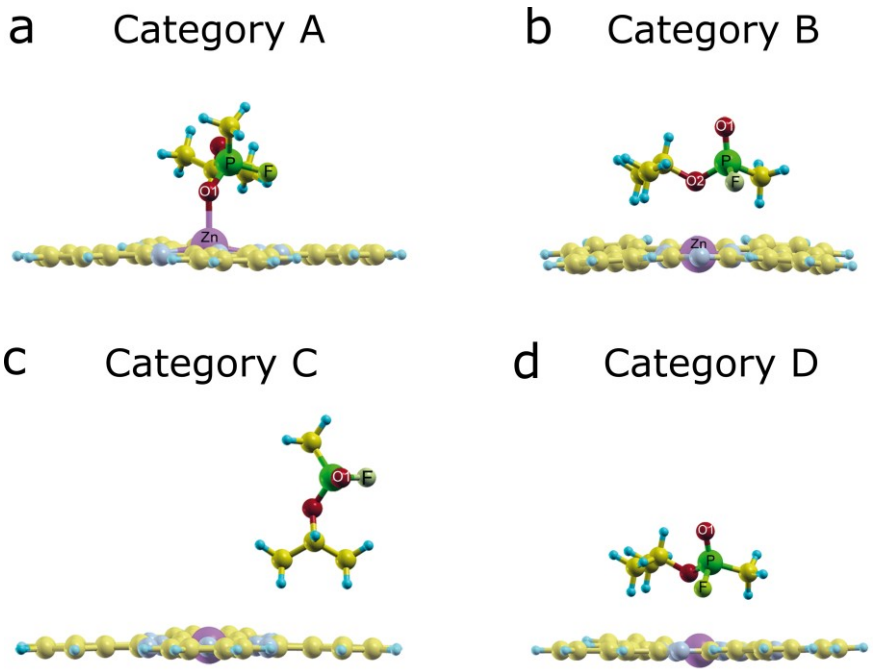

Figure 5.27. Side-views of the different calculated stable structures of sarin on ZnPc denoted as categories depending on a the type of the formed bond.

The calculations showed that as for DMMP, the category A is the most stable one. Categories B, C and D are less stable than category 1 by about 1.07, 1.4 and 0.45 eV, respectively. In order to describe the adsorption geometry in category A, the same parameters as for DMMP were employed (r, d, α and θ) (Figure 5.28). The parameters r and d for sarin adsorption geometry were the same as for DMMP (within the uncertainty), while angles α and θ differed slightly. The biggest difference was obtained for angle θ (12° for sarin vs 30° for DMMP). However, the influence of parameter θ on adsorption energy is negligible. The change of θ to 45° increases the energy only by 5 meV. The adsorption energy of sarin on ZnPc is slightly lower (10 meV) that the value obtained for DMMP with higher contribution of vdW interactions (see Table 5.10). In order to verify if sarin adsorbs similarly as DMMP also on other MPcs, the adsorption energies and geometry parameters r and d were calculated for CoPc, CuPc and NiPc and compared to the corresponding values for DMMP (Table 5.10). As one can observe, sarin similarly to DMMP interacts with studied MPcs mostly through vdW interactions and the order of adsorption energies is the same as for DMMP.

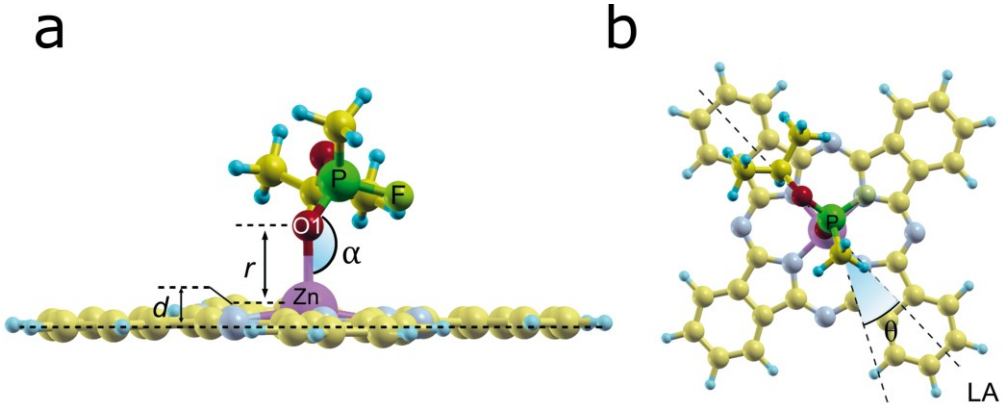

Figure 5.28. a: Top and b: side-views of the most stable adsorption configuration of sarin on ZnPc.

Table 5.10. Calculated adsorption energies and geometry parameters of sarin on different MPcs, compared with the corresponding parameters from DMMP.

Structure	E_{ads} (eV)		Dispersion energy in eV (contribution to E_{ads} %)		*d* (Å)		*r* (Å)	
	sarin	**DMMP**	**sarin**	**DMMP**	**sarin**	**DMMP**	**sarin**	**DMMP**
ZnPc	-0.93	-0.92	-0.43 (46%)	-0.45 (49%)	0.35	0.35	2.18	2.14
CoPc	-0.83	-0.80	-0.49 (58%)	-0.52 (65%)	0.10	0.15	2.28	2.23
CuPc	-0.58	-0.51	-0.44 (77%)	-0.45 (88%)	0.06	0.09	2.57	2.46
NiPc	-0.52	-0.42	-0.46 (90%)	-0.40 (95%)	0.002	0.01	2.94	2.80

Charge transfer

Beside the adsorption geometries and energies, the other important factor for sensing structure performance is charge transfer as it was demonstrated for DMMP. Since the most stable structure of ZnPc/sarin system is similar to that for ZnPc/DMMP in terms of both – adsorption geometry and energy, one can expect also similar charge transfer. In order to verify it, the Lowdin analysis was performed for sarin interacting with single molecule of ZnPc. The results of this analysis showed the electrons transfer from sarin to ZnPc with a value similar to the one obtained in case of DMMP (see Table 5.11). Again, there was a charge accumulation mostly on the Zn atom in the center of Pc. As it was shown for DMMP, the charge transferred from the adsorbed species barely relocate between Pc layers. Thus, also for sarin the main sensing mechanism expected from the calculations is a charge transfer from sarin to the Pc and surface dipole formation. Given almost the same geometry of adsorption in case of DMMP and sarin and the same values of charge transfer, the dipole should be similar to the one formed between ZnPc and DMMP in terms of the direction and the value.

Table 5.11. Results of charge transfer analysis between sarin and ZnPc single molecule

Molecule	**Δq (e)**	**Δq per atom type (e)**				
ZnPc single molecule						
Sarin	-0.20					
ZnPc	0.34	Zn	N inner	N outer	C	H
		0.08	-0.07	0.04	0.24	0.05

5.2.8 Second approach conclusions

In this part of the thesis, the comprehensive study of DMMP interaction with MPcs was carried out. First, ZnPc was chosen as the best candidate for DMMP detection among the most common MPcs (CuPc, ZnPc, PbPc, FePc) based on the preliminary theoretical study using semi-empirical methods. Next, DFT calculations of DMMP adsorption were performed for ZnPc. The investigation allowed determining preferable adsorption sites for DMMP on ZnPc surface. The most stable conformation was found for the DMMP covalently bonded with Zn atom through the oxygen present in the O=P bond in DMMP molecule. The adsorption geometry and adsorption energy for this conformation was compared with other transition metal phthalocyanines (NiPc, CuPc and CoPc) and the strongest interaction was found for ZnPc. In the next step the detailed theoretical study of adsorption on ZnPc monolayers was carried out. It was found that among possible types of ZnPc monolayers, the most preferable ones in DMMP sensor are those where molecules are planarly well-ordered, so the adsorption sites are highly available. Since the orientation of Pc in the real sensing structure depends on the substrate, deposition technique and deposition temperature and pressure, it is important to take this factor into account during sensor device design. The crucial part of this research was a charge relocation investigation. The theoretical investigation of the charge transfer after DMMP adsorption was confirmed by XPS and UPS studies. The results indicated that the modification of the surface dipole was instrumental for the sensing mechanism and needs to be evaluated in sensing device design. Finally, The TDS study before and after ZnPc exposition to DMMP was carried out. The results indicated that DMMP desorbs from the ZnPc surface with the desorption activation energy in the range from 1.7 eV to 2.1 eV and decompose into formaldehyde. Other possible products of desorbing DMMP decomposition are hydrogen, water, carbon oxide and carbon dioxide. However, those species exist also in the pristine sample as impurities adsorbed from the ambience. The study of DMMP desorption from the ZnPc surface requires further investigation. Because of the limitations of experimental setup applied in this thesis, it was not possible to detect the entire DMMP molecule and the detection of possible decomposition products was limited to ten different atomic masses. Moreover, in situ TDS study should be performed to reduce the number of impurities adsorbed from the ambience.

In order to verify the validity of using DMMP as a model molecule of sarin in the sensing mechanism investigation of structures based on MPcs, the DFT modeling of sarin adsorption was performed. The adsorption geometries and energies for sarin interacting with ZnPc, NiPc, CuPc and CoPc were compared with corresponding parameters obtained from calculations for DMMP. The results showed that both, DMMP and sarin in the most stable adsorption geometry form covalent bond with ZnPc central atom via the O=P oxygen. The charge transfer analysis was performed for sarin adsorbed on ZnPc and the results indicated the formation of a surface dipole with the same direction and value as in case of DMMP. Thus, the conclusion arises that in the experimental investigation of sarin interaction with MPcs, DMMP can be used as a model molecule giving with a good approximation the results comparable with a real CWA.

6 Summary and outlook

The aim of this thesis was to develop a fundamental approach to sensing mechanisms evaluation and its application for DMMP sensing by hybrid sensor structures based on Pcs, Pd and PdO. Several theoretical and experimental methods have been employed.
After initial studies, H_2Pc/Pd sensing structure has been chosen for further investigation with the assumption that Pd layer can be partially oxidized, forming H_2Pc/Pd/PdO structure. The studied structure revealed sensing response to DMMP at room temperature. This response has been correlated with the results of semi-empirical modelling of DMMP adsorption, AFM topography images and the XPS spectra of DMMP exposed sample. The most important outcomes were as follows:

- The physisorption with formation of a surface dipole is the main sensing mechanism;
- Pd/PdO layer enhances the H_2Pc sensing performance by increasing the DMMP adsorption energy and forming metal nanoclusters on the H_2Pc surface that can help adsorbed gas diffusion into the sensing structure.

The second part of the research was focused on the investigation of sensing mechanisms in MPc-based sensing structures for DMMP detection. The significant part of this study was a detailed theoretical investigation of DMMP adsorption on MPcs. The analysis has been performed by DFT method that was complemented by XPS, UPS, TDS and AFM study of ZnPc layers. Also the theoretical study of sarin adsorption on MPcs has been carried out in order to support the choice of DMMP as a benign model of sarin. The most important outcomes of this part were:

- DMMP interacts with ZnPc via a covalent bond between P=O and Zn atom that induces electrons transfer from DMMP molecule to the first layer of the ZnPc and the formation of surface dipole;
- Among possible types of ZnPc layers orientations, the most preferable ones in DMMP sensor are those where molecules are planarly well-ordered, so the preferable adsorption sites are available;
- DMMP desorbing from the ZnPc surface undergoes decomposition with formaldehyde among the products;
- DMMP can be used as a model molecule giving, with a good approximation, theoretical results comparable with the real CWA.

The author's original contribution to the field of CWAs sensors includes:

- The development of a fundamental approach to the sensing mechanisms investigation, based on theoretical and experimental studies of DMMP and sarin adsorption;
- The study of DMMP sensing mechanisms for hybrid structures consisting of metal-free phthalocyanine, palladium and palladium oxide;
- The comprehensive theoretical investigation of DMMP and sarin adsorption on ZnPc single molecule, monolayers and multi-stacks, supported by XPS, UPS and TDS experimental results.

Although the research performed within this thesis gave enough results to explain the mechanisms of DMMP sensing by Pcs and hybrid structures based on Pc and Pd/PdO, there are still open questions that can be addressed in the future work. At the level of fundamental study of DMMP/sarin adsorption mechanisms on ZnPc and SMO/ZnPc hybrid structures, the influence of SMO/ZnPc interface on sensing performance should be studied in detail. Moreover, the DMMP desorption from the ZnPc surface requires further investigation. Finally, based on the outcomes of this thesis, the real sensing structure can be designed and tested

Appendix A. Abbreviations

AFM – atomic force microscopy

AM1 - Austin model 1

BE – binding energy

BET – Branauer, Emmet and Teller

CWA – chemical warfare agents

DFT – density functional theory

DMMP – dimethyl methylophosphonate

FET – field effect transistor

GGA - general gradient approximation

GTO – Gaussian type orbitals

HF – Hartree-Fock

IDE – interdigitated electrodes

LA –long axis

LDA - local density approximation

ML – monolayer

MNDO - modified neglect of differential overlap

MO – molecular orbital

MPc- metallo-phthalocyanine

NCPP - norm-conserving pseudopotential

NNDO - neglect of differential diatomic overlap

PAW - projector-augmented wave

PBE - Perdew, Burke, Enzerhof functional

Pc – phthalocyanine

PE – photoemission

PES – photoelectron spectroscopy

PL – photoluminescence

PM3 - parametric model number 3

PM6 - parametric model number 6

PVD – physical vapor deposition

QCM – quartz crystal microbalance

RMS – root mean square

SMO – semiconducting metal oxide

SR – sensor response

STO – Slater type orbitals

TDS – thermal desorption spectroscopy

UHV – ultrahigh vacuum

UPS – ultraviolet photoelectron spectroscopy

UV – ultraviolet

vdW – van der Waals

WF – work function

XPS – X-ray photoelectron spectroscopy

Appendix B. Publications and conference presentations

PUBLICATIONS

1. M. Matys, P. Powrożnik, D. Kupka, B. Adamowicz, Two-dimensional modeling of surface photovoltage in metal/insulator/n-GaN structure with cylindrical symmetry, Optica Applicata 43 (2013), 47-52.

2. W. Jakubik, P. Powroźnik, J. Wrotniak, M. Krzywiecki, T. Hejczyk, Theoretical Analysis of Acoustoelectrical Sensitivity in SAW Gas Sensors, Procedia Engineering 120 (2015), 1261–1264.

3. P. Powroźnik, W. Jakubik, A. Kaźmierczak-Bałata, Detection of organophosphorus (DMMP) vapour using phthalocyanine-palladium bilayer structures, Procedia Engineering 120 (2015), 368-371.

4. W. Jakubik, P. Powroźnik, J. Wrotniak, M. Krzywiecki, Theoretical analysis of acoustoelectrical sensitivity in SAW gas sensors with single and bi-layer structures, Sensors and Actuators B: Chemical 236 (2016), 1069-1074.

5. P. Powroźnik, M. Krzywiecki., L. Grządziel., W. Jakubik, Study of Sensing Mechanisms in Nerve Agent Sensors Based on Phthalocyanine-palladium Structures, Procedia Engineering 168 (2016), 586-589.

6. M. Krzywiecki, L. Grzadziel., P. Powroźnik., M. Kwoka., J. Rechmann, A. Erbe, Oxide-organic heterostructures: A case study of charge transfer disturbance at a SnO_2-copper phthalocyanine buried interface, Physical Chemistry Chemical Physics 20, 23 (2018), 16092-16101.

7. J. Wrotniak, W. Jakubik, P. Powroźnik, A. Stolarczyk, M. Magnuski, Acoustical studies of polymer (RR)-P3HT type for the determination of DMMP in air, Przegląd Elektrotechniczny 94 (2018), 70-73.

8. W. Jakubik, J. Wrotniak, P. Powroźnik, Theoretical analysis of a surface acoustic wave gas sensor mechanism using electrical conductive bi-layer nanostructures, Sensors and Actuators B: Chemical 262 (2018), 947-952.

9. P. Powroźnik, L. Grządziel, W. Jakubik, M. Krzywiecki, Sarin-simulant detection by phthalocyanine/palladium structures: From modeling to real sensor response, Sensors and Actuators B: Chemical 273 (2018), 771-777.

10. P. Powroźnik, W. Jakubik, A. Stolarczyk, A. Kaźmierczak-Bałata, J. Wrotniak, T. Jarosz, Study of light-activated regioregular poly(3-hexyltiophene) photoconductive polymer sensins properties in nerve agent simulant (DMMP) detection, Sensors 20 (2020), 491.

11. H. Adahhak, P. Powroźnik, P. H. Pander, W. Jakubik, F. B. Dias, W. G. Schmidt, U. Gerstmann and M. Krzywiecki, Towards Efficient Toxic-Gas Detectors: Exploring Molecular Interactions of Sarin and Dimethyl Methylphosphonate With Metal-Centered Phthalocyanine Structures, https://doi.org/10.1021/acs.jpcc.9b11116.

CONFERENCE PRESENTATIONS

1. XII Seminar Surface and Film Film Structures, Szklarska Poręba (Poland), 9-12.05.2012, poster "Two-dimensional modeling of a surface photovoltage in structures metal/insulator/GaN with cylindrical symmetry"

2. Eurosensors 2015, 6-9.09.2015, Freiburg (Germany), oral presentation "Detection of organophosphorus (DMMP) vapour using phthalocyanine-palladium bilayer structures"

3. IX International Workshop on Semiconductor Gas Sensors, 13-16.12.2015, Zakopane (Poland), poster "Organophosphorus vapours detection using phthalocyanine-palladium nanostructures"

4. InterNanoPoland 2016, 14.06.2016, Katowice (Poland), poster "Detection of nerve agents and organic vapours using thin semiconductor films"

5. Eurosensors 2016, 4-7.09.2016, Budapest (Hungary), poster "Study of Sensing Mechanisms in Nerve Agent Sensors Based on Phthalocyanine-Palladium Structures"

6. Eurosensors 2017, 3-6.09.2017, Paris (France), poster "Study of Poly(3-hexyltiophene) Polymer Sensing Properties in Nerve Agent Simulant (DMMP) Detection"

7. V Workshop on Organic Electronics and Nanophotonics (WOREN 2018), 11-15.02.2018, Wisła (Poland) poster "A cluster approach for electronic structure description in multilayered oxide/organic hybrids"

8. UK Semiconductors 2019, 10-11.07.2019, Sheffield (UK), oral presentation "Adsorption of DMMP molecules on zinc phthalocyanine: towards nerve agents sensor design"

References

[1] National Research Council, Acute Exposure Guideline Levels for Selected Airbone Chemicals, The National Academies Press: Washington, DC 3 (2003).

[2] F. I. Bohrer, C. N. Colesniuc, J. Park, M. E. Ruidiaz, I. K. Schuller, A. C. Kummel, W. C. Trogler, Comparative gas sensing in cobalt, nickel, copper, zinc, and metal-free phthalocyanine chemiresistors, J. Am. Chem. Soc. 131 (2) (2009) 478-485.

[3] J. Wang, X. Du, Y. Long, X. Tang, X. Tai, Y. Jiang, The response comparison of a hydrogen-bond acidic polymer to sarin, soman and dimethyl-methylphosphonate based on a surface acoustic wave sensor, Appl. Methods. 6 (2014), 1951.

[4] J. P. Novak, E. S. Snow, E. J. Houser, D. Park, J. L. Stepnowski, R. A. McGill, Nerve agent detection using networks of single-walled carbon nanotubes, App. Phys. Lett. 83 (2003) 4026.

[5] Y. Wang, Z. Yang, Z. Hou, D. Xu, L. Wei, E. Siu-Wai Kong, Y. Zhang, Flexible gas sensors with assembled carbon nanotube thin films for DMMP vapor detection, Sens. Actuat. B: Chem 150 (2010) 708–714.

[6] R. Yoo, J. Kim, M. J. Song, W. Lee, and J. S. Noh, Nano-composite sensors composed of single-walled carbon nanotubes and polyaniline for the detection of a nerve agent simulant gas**,** Sens. Actuat. B: Chem 209 (2015) 444-448.

[7] X. Ji, W. Yao, J. Peng, N. Ren, J. Zhou, Y. Huang, Evaluation of Cu-ZSM-5 zeolites as QCM sensor coatings for DMMP detection, Sens. Actuat. B: Chem 166– 167 (2012) 50–55.

[8] S. Guo, Z. Cheng, H. Zhu, L. Wang, C. Zhou, Hydrogen-bond acid group functionalized mesoporous- silica MCM-41 as sensing material to detect trace level organophosphorus vapour, Adv. Mat. Res. 1092-1093 (2015) 780-783.

[9] Y. Long, Y. Wang, X. Du, L. Cheng, P. Wu, Y. Jiang, The different sensitive behaviors of a hydrogen-bond acidic polymer-coated SAW sensor for chemical warfare agents and their simulants, Sensors 15 (2015) 18302-18314.

[10] X. Du, Z. Ying, Y. Jian, Z. Liu, T. Yang, G. Xie, Synthesis and evaluation of a new polysiloxane as SAW sensor coatings for DMMP detection, Sens. Actuat. B: Chem 134 (2008) 409–413.

[11] R. Yoo, S. Chi, M. J. Song, W. Lee, Highly sensitive gas sensor based on Al-doped ZnO nanoparticles for detection of dimethyl methylphosphonate as a chemical warfare agent simulant, Sens. Actuat. B: Chem 221 (2015) 217-223.

[12] S. M. Kanan, A. Waghe, B. L. Jensen, C. P. Tripp, Dual WO3 based sensors to selectively detect DMMP in the presence of alcohols, Talanta 72 (2007) 401–407.

[13] S. C. Lee, Ho Y. Choi, S. J. Lee, W. S. Lee, J. S. Huh, D. D. Lee, J. C. Kim, The development of SnO2-based recoverable gas sensors for the detection of DMMP, Sens. Actuat. B: Chem 137 (2009) 239–245.

[14] C. V. Kumar, G. Sfyri, D. Raptis, E. Stathatos and P. Lianos, Perovskite solar cell with low cost Cu-phthalocyanine as hole transporting material, RSC Adv. 5 (2015) 3786-3791.

[15] K. T. Cho, K. Rakstys, M. Cavazzini, S. Orlandi, G. Pozzi, M. K. Nazeeruddin, Perovskite Solar Cells Employing Molecularly Engineered Zn(II) Phthalocyanines as Hole-transporting Materials, Nano Energy 30 (2016) 853-857.

[16] K. T. Cho, O. Trukhina, C. Roldan-Carmona, M. Ince, P. Gratia, G. Grancini, P. Gao, T. Marszalek, W. Pisula, P. Y. Reddy, T. Torres, M. K. Nazeeruddin, Molecularly Engineered Phthalocyanines as Hole-Transporting Materials in Perovskite Solar Cells Reaching Power Conversion Efficiency of 17.5%, Adv. Energy Mater. 7, 7 (2016).

[17] M. Urbani, M. E. Ragousi, M. K. Nazeeruddin, T. Torres, Phthalocyanines for dye-sensitized solar cells, Coord. Chem. Rev. 381 (2019) 1-64.

[18] A. Kumar, J. Brunet, C. Varenne, A. Ndiaye, A. Pauly, M. Penza, M. Alvisi, Tetra-tert-cutyl-copper phthalocyanine based QCM sensor for toluene detection in air at room temperature, Sens. Actuat. B: Chem. 210 (2015) 398-407.

[19] A. Rydosz, E. Maciak, K. Wincza, S. Gruszczynski, Microwave-based sensors with phthalocyanine films for acetone, ethanol and methanol detection, Sens. Actuat. B: Chem. 237 (2016) 876-886.

[20] Q. Sun, W. Feng, P. Yang, G. You, Y. Chen, Highly selective room-temperature NO_2 sensor based on a fluoroalkoxy-substituted phthalocyanine, New J. Chem. 42 (2018) 6673-6688.

[21] Z. Dong, X. Kong, Y. Wu, J. Zhang, Y. Chen, High-sensitive room-temperature NO_2 sensor based on a aoluble n-type phthalocyanine semiconductor, Inorg. Chem. Commun. 77 (2017) 18-22.

[22] D. Mukherjee, R. Manjunatha, S. Sampath, A. Kumar Ray, Phthalocyanines as sensitive materials for chemical sensors. In: Cesar Paixão T., Reddy S. (eds) Materials for Chemical Sensing, Springer Chem., 2017.

[23] C. Tasaltin, I. Gurol, M. Harbeck, E. Musluoglu, V. Ahsen, Z. Z. Ozturk, Synthesis and DMMP sensing properties of fluoroalkyloxy and fluoroaryloxy substituted phthalocyanines in acoustic sensors, Sens. Actuat. B: Chem. 150 (2010) 781-787.

[24] A. T. Bilgicli, A. Gunsel, M. Kandaz, A. Altindal, H. Comert, Double-decker senor phthalocyanines functionalizes with 1-hydroxyhexane-3-ylthio moieties; synthesis, characterization, electrical properties and *H*- or *J*- type aggregation studies, J. Organomet. Chem.785 (2015) 112-121.

[25] A. K. Sharma, A. Mahajan, R. K. Bedi, S. Kumar, A. K. Debnath, D. K. Aswal, Non-covalently anchored multi-walled carbon nanotubes with hexa-decafluorinated zinc phthalocyanine as ppb level chemiresistive chlorine sensor, Appl. Surf. Sci. 427 (2018) 202-209.

[26] F. Siviero, N. Coppedè, A. Pallaoro, A. M. Taurino, T. Toccoli, P. Siciliano, S. Iannotta, Hybrid *n*-TiO_2-CuPc gas sensors sensitive to reducing species, synthesized by cluster and supersonic beam deposition, Sens. Actuat. B: Chem 126 (2007) 771-777.

[27] X. Zhou, X. Wang, B. Wang, Z. Chen, C. He, Y. Wu, Preparation, characterization and NH_3-sensing properties of reduced graphene oxide/copper phthalocyanine hybrid material, Sens. Actuat. B: Chem 193 (2014) 340-348.

[28] N. Coppedè, M. Villani, R. Mosca, S. Iannotta, A. Zappettini, D. Calestani, Low Temperature Sensing Properties of a Nano Hybrid Material Based on ZnO Nanotetrapods and Titanyl Phthalocyanine, Sensors 13, 3 (2013) 3445-3453.

[29] A. V. Zasedatelev, D. M. Krichevsky, Y. M. Zelenskiy, A. Y. Tolbin, V. I. Krasovskii, A. B. Karpo, L. G. Tomilova, Enhancement of NO_2 gas detection in hybrid silver nanoparticles-phthalocyanine thin films, J. Phys.: Conf. Ser. 737 (2016) 012031.

[30] R. D. Yang, J. Park, C. N. Colesniuc, I. K. Schuller, J. E. Royer, W. C. Trogler and A. C. Kummel, Analyte chemisorption and sensing on *n*- and *p*- channel copper phthalocyanine thin film transistors, J. Chem. Phys. 130 (2009) 164703.

[31] D. C. Tiwari, R. Sharma, K.D. Vyas, M. Boopathi, V. V. Singh, P. Pandey, Electrochemical incorporation of copper phthalocyanine in conducting polypyrrole for the sensing od DMMP, Sens. Actuat. B: Chem. 151 (2010) 256-264.

[32] C. Tasaltin, I. Gurol, M. Harbeck, E. Musluoglu, V. Ahsen, Z.Z. Ozturk, Synthesis and DMMMP sensing properties of fluoroalkyloxy and fluoroaryloxy substituted phthalocyanines in acoustic sensors, Sens. Actuat. B: Chem 150 (2010) 781-787.

[33] D. Zou, W. Zhao, B. Cui, D. Li, D. Liu, Adsorption of gas molecules on a manganese phthalocyanine molecular device and its possibility as a gas sensor, Phys. Chem. Chem. Phys. 20 **(**2018) 1364-1372.

[34] Baggio, A. R.; Machado, D. F. S.; Carvalho-Silva, V. H.; Patemo L. G.; De Oliveira, H. C. B, Rovibrational spectroscopic constants of the interaction between ammonia and metallo-phthalocyanines: a theoretical protocol for ammonia sensor design, Phys. Chem. Chem. Phys. 19 **(**2017) 10843-10853.

[35] B. Aurian-Blajeni, M. M. Boucher, Interaction of Dimethyl Methylphosphonate with Metal Oxides. Langmuir 5 (1989**)** 170-174.

[36] J. Zhou, K. Varazo, J. E. Reddic, M. L. Myrick, D. A. Chen, Decomposition of Dimethyl Methylphosphonate on TiO2(110): Principal Component Analysis Applied to X-ray Photoelectron Spectroscopy, Anal. Chim. Acta 496 (2003) 289-300.

[37] C. N. Rusu, J. T. Yates Jr., Adsorption and Decomposition of Dimethyl Methylphosphonate on TiO2. J. Phys. Chem. B 104 (2000) 12292-12298.

[38] C. S. Kim, R. J. Lad, C. P. Tripp, Interaction of Organophosphorous Compounds with TiO2 and WO3 Surfaces Probed by Vibrational Spectroscopy, Sens. Actuat. B: Chem. 76 (2001) 442-448.

[39] D. A. Panayotov, J. R. Morris, Uptake of a Chemical Warfare Agent Simulant (DMMP) on TiO2: Reactive Adsorption and Active Site Poisoning. Langmuir 25 (2009) 3652-3658.

[40] D. A. Panayotov, J. R. Morris, Thermal Decomposition of a Chemical Warfare Agent Simulant (DMMP) on TiO2: Adsorbate Reactions with Lattice Oxygen as Studied by Infrared

Spectroscopy, J. Phys. Chem. C 113 (2009) 15684-15691.

[41] J.A. Moss, S. H. Szczepankiewicz, E. Park, M. R. Hoffman, Adsorption and Photodegradation of Dimethyl Methylphosphonate Vapor at TiO2 Surfaces, J. Phys. Chem. B 109 (2005) 19779-19785.

[42] M. B. Mitchell, V. N. Sheinker, E. A. Mintz, Adsorption and Decomposition of Dimethyl Methylphosphonate on Metal Oxides, J. Phys. Chem. B 101 (1997) 11192-11203.

[43] M. K. Templeton, W. H. Weinberg, Decomposition of Phosphonate Esters Adsorbed on Aluminum Oxide, J. Am. Chem. Soc. 107 (1985) 774-779.

[44] M. K. Templeton, W. H. Weinberg, Adsorption and Decomposition of Dimethyl Methylphosphonate on an Aluminum Oxide Surface, J. Am. Chem. Soc. 107 (1985) 97-108.

[45] M. A. Henderson, T. Jin, J. M. White, A TPD/AES Study of the Interaction of Dimethyl Methylphosphonate with α-Fe2O3 and SiO2, J. Phys. Chem. 90 (1986) 4607-4611.

[46] T. M. Tesfai, V. N. Scheinker, M. B. Mitchell, Decomposition of Dimethyl Methylphosphonate (DMMP) on Alumina-Supported Iron Oxide, J. Phys. Chem. B 102 (1998) 7299-7302.

[47] S. M. Kanan, C. P. Tripp, An Infrared Study of Adsorbed Organophosphonates on Silica: A Prefiltering Strategy of the Detection of Nerve Agents on Metal Oxide Sensors, Langmuir 17 (2001) 2213-2218.

[48] Y. Paukku, A. Michalkova,J. Leszczynski, Adsorption of dimethyl methylphosphonate and trimethyl phosphate on calcium oxide: an ab initio study, Struct. Chem. 19 (2008) 307–320.

[49] A. R. Head, R. Tsyshevsky, L. Trotochaud, Y. Yu, O. Karslıoğlu, B. Eichhorn, M. M Kuklja and H. Bluhm, Dimethyl methylphosphonate adsorption and decomposition on MoO_2 as studied by ambient pressure X-ray photoelectron spectroscopy and DFT calculations, J. Phys.: Condens. Matter 30 (2018) 134005.

[50] Y. Paukku, A. Michalkova, and J. Leszczynski, Quantum-Chemical Comprehensive Study of the Organophosphorus Compounds Adsorption on Zinc Oxide Surfaces, J. Phys. Chem. C 113 (2009) 1474–1485.

[51] A. R. Head, R. Tsyshevsky, L. Trotochaud, Y. Yu, L. Kyhl, O. Karslıoğlu, M. M. Kuklja, and H. Bluhm, Adsorption of Dimethyl Methylphosphonate on MoO_3: The Role of Oxygen Vacancies, J. Phys. Chem. C 120 (2016) 29077−29088.

[52] S. Holdren, R. Tsyshevsky, K. Fears, J. Owrutsky, T. Wu, X. Wang, B. W. Eichhorn, M. M. Kuklja, and M. R. Zachariah, Adsorption and Destruction of the G-Series Nerve Agent Simulant Dimethyl Methylphosphonate on Zinc Oxide, ACS Catal. 9 (2019) 902−911.

[53] U. Lampe, M. Fleischer, J. Reitmeier, J. B. McMonagle, A. Marsh, and H. Meixner, Metal Oxide Gas Sensors, in Sensors Update, edited by H. Baltes, W. Göpel, and J. Hess (1996) 1–36.

[54] V.Ya. Sukharev, L.Yu. Kupriyanov (Ed.), Semiconductor Sensors in Physico-Chemical Studies, Elsevier, Amsterdam (1996) 5-101 (Chapter 1).

[55] K. Galatsis, Y. X. Li, W. Wlodarski, E. Comini, G. Sberveglieri, C. Cantalini, S. Santucci, M. Passacantando, Comparison of single and binary oxide MoO_3, TiO_2 and WO_3 sol–gel gas sensors, Sens. Actuat. B: Chem 83 (2002) 276-280.

[56] M.B. Rahmani, S.H. Keshmiri, J. Yu, A.Z. Sadek, L. Al-Mashat, A. Moafi, K. Latham, Y.X. Li, W. Wlodarski, K. Kalantar-zadeh, Gas sensing properties of thermally evaporated lamellar MoO_3, Sens. Actuat. B:Chem 145 (2010) 13-19.

[57] K. Galatsis, Y.X. Li, W. Wlodarski, E. Comini, G. Faglia, G. Sberveglieri, Semiconductor MoO_3-TiO_2 thin film gas sensors, Sens. Actuat. B: Chem 77 (2001) 472-477.

[58] D Mutschall, K Holzner, E Obermeier, Sputtered molybdenum oxide thin films for NH3 detection, Sens. Actuat. B: Chem. 35/36 (1996) 320-324.

59S.S. Sunu, E. Prabhu, V. Jayaraman, K.I. Gnanasekar, T.K. Seshagiri, T. Gnanasekaran, Electrical conductivity and gas sensing properties of MoO3, Sens. Actuat. B:Chem 101 (1–2) (2004) 161-174.

[60] C. Imawan, H. Steffes, F. Solzbacher, E. Obermeier, A new preparation method for sputtered MoO3 multilayers for the application in gas sensors Sens. Actuat. B: Chem. 78 (2001) 119-125.

[61]M. Ferroni, V. Guidi, G. Martinelli, P. Nelli, M. Sacerdoti, G. Sberveglieri, Characterization of a molybdenum oxide sputtered thin film as a gas sensor, Thin Solid Films 307 ((1997) 148-151.

[62]S.S. Sunu, E. Prabhu, V. Jayaraman, K.I. Gnanasekar, T.K. Seshagiri, T. GnanasekaranElect rical conductivity and gas sensing properties of MoO3, Sens. Actuat. B: Chem. 101 (2004) 161-174.

[63] S.S. Sunu, E. Prabhu, V. Jayaraman, K.I. Gnanasekar, T. Gnanasekaran, Gas sensing properties of PLD made MoO3 films, Sens. Actuat. B: Chem. 94 (2003) 189-196.

[64] S. Barazzouk, R.P. Tandon, S. Hotchandani, MoO_3-based sensor for NO, NO_2 and CH_4 detection, Sens. Actuat. B: Chem. 119 (2006) 691-694.

[65] S. Yang, Y. Liu, T. Chen, W. Jin, T. Yang, M. Cao, S. Liu, J. Zhou, G. S. Zakharowa, W. Chen, Zn doped MoO_3 nanobelts and the enhanced gas sensing properties to ethanol, Appl. Surf. Sci. 393 (2017) 377-384.

[66] H. M.M. Munasinghe Arachchige, D. Zappa, N. Pioli, N. Guanawardhana, E. Comini, Gold funcionalized MoO_3 nano flakes for gas sensing applications, Sens. Acctuat. B: Chem. 269 (2018) 331-339.

[67] Z. li, P. Song, Z. Yang, Q. Wang, In situ formation of one-dimensional $CoMoO_4/MoO_3$ heterojunction as an effective trimethylamine gas sensor, Ceram. Int. 44 (2018) 3364-3370.

[68] W. Jiang, L. Meng, S. Zhang, X. Chuai, Z. Zhou, C. Hu, P. Sun, F. Liu, G. Lu, Design of highly sensitive and selective xylene gas sensor based on Ni-doped MoO_3 nano-pompon, Sens. Actuat. B: Chem. 299 (2019) 126888.

[69] W. Jakubik, M. Krzywiecki, E. Maciak, M. Urbańczyk, Bi-layer nanostructures of CuPc and Pd for resistance-type and SAW-type hydrogen gas sensors, Sens. Actuat. B: Chem 175 (2012) 255-262.

[70] B. H. Fisher, D. C. Malocha, IEEE Transitions on Ultrasonics, Ferroelectrics and Frequency Control 57 (2010) 698

[71] C. Viespe, D. Miu, Surface Acoustic Wave sensor with Pd/ZnO bilayer structure for room temperature hydrogen detection, Sensors 17 (2017) 1529.

[72] Yu-Ju Chiang, Kuang-Chung Li, Yi-Chien Lin and Fu-Ming Pan, A mechanistic study of hydrogen gas sensing bu PdO nanoflake thin films at temperatures below 250 ºC, Phys. Chem. Chem. Phys. 17 (2015) 3039-3049.

[73] E. Brunol, F. Berger, M. Fromm, R. Planade, Detection of dimethyl methylphosphonate (DMMP) by tin dioxide-based gas sensor: Response curve and understanding of the reactional mechanism, Sens. Actuat. B: Chem 120 (2006), 35-41.

[74] F. Schedin, A. K. Geim, S. V. Morozov, E. W. Hill, P. Blake, M. I. Katsnelson, K. S. Novoselov, Detection of individual gas molecules adsorbed on graphene, Nature Materials 6 (2007) 652-655.

[75] G. Korotcenkov, M. Ivanov, I. Blinov, J. R. Stetter, Kinetics of indium oxide-based thin film gas sensor response: The role of “redox” and adsorption/desorption proceses in gas sensing effects, Thin Solid Films 515 (2007) 3987-3996.

[76] L. Kou, T. Frauenheim, C. Chen, Phosphorene as a Superior Gas Sensor: Selective Adsorption and Distinct I-V Response, J. Phys. Chem. Lett. 5, 15 (2014) 2675-2681.

[77] S. Aghaei, M. M. Monshi, I. Calizo, A theoretical study of gas adsorption on silicone nanoribbons and its application in highly sensitive molecule sensor, RSC Adv. 6 (2016) 94417-94428.

[78] A. Hulanicki, S. Geab, F. Ingman, Chemical Sensors Definitions and Classification, Pure and Appl. Chem. 63 (1991) 1247.

[79] R.W. Catterall, Chemical Sensors (Oxford Chemistry Primers), Oxford Science Publications, 1997.

[80] X. Liu, S. Cheng, H. Liu, S. Hu, D. Zhang, H. Ning, A survey on gas sensing technology, Sensors 12 (2012) 9635–9665.

[81] E. Comini, Metal oxide nano-crystals for gas sensing, Anal. Chem. Acta 568 (2006) 28–40.

[82] N. Tachugi, Japanese Patent 45-38200.

[83] G. Neri, First Fifty Years of Chemoresistive Gas Sensors, Chemosensors 3 (2015) 1-20.

[84] A. Dey, Semiconductor metal oxide gas sensors: A review, Mater. Sci. Eng. B, 229 (2018) 206-217.

[85] B. Sharma, J-S Kim, MEMS based highly sensitive dual FET gas sensor using graphene decorated Pd-Ag alloy nanoparticles for H_2 detection, Scientific Reports 8 (2018) 5902.

[86] Z. Zhang, X. Zou, L. Xu, L. Liao, W. Liu, J. Ho, X. Xiao, C. Jiang, J. Li, Hydrogen gas sensor based on metal oxide nanoparticles decorated graphene transistor, Nanoscale 22 (2015) 10078-10084.

[87] M. Wu, J. Shin, Y. Hong, D. Jang, X. Jin, H-I Kwon, J-H Lee, An FET-type gas sensor with a sodium ion conducting solid electrolyte for CO_2 detection, Sens. Actuat. B: Chem 259 (2018), 1058-1065.

[88] S. Hong, J. Shin, Y. Hong, M. Wu, D. Jang, Y. Jeong, G. Jung, J-H Bae, H. W. Jang, J-H Lee, Observation of physisorption in a high-performance FET-type oxygen gas sensor operating at room temperature, Nanoscale 10 (2018) 18019-18027.

[89] S. T. Tan, C. H. Tan, W. Y. Chong, C. C. Yap, A. A. Umar, R. T. Ginting, H. B. Lee, K. S. Lim, M. Yahaya, M. M. Salleh, Microwave-assisted hydrolysis preparation of highly crystalline ZnO nanorod array for room temperature photoluminescence-based CO gas sensor, Sens. Actuat. B: Chem 227 (2016), 304-312.

[90] R-B Lin, S-Y Liu, J-W Ye, X-Y Li, J-P Zhang, Photoluminescent Metal–Organic Frameworks for Gas Sensing, Adv. Sci. 3 (2016), 1500434.

[91] K. Yadav, S. K. Gahlaut, B. R. Mehta, J. P. Singh, Photoluminescence based H_2 and O_2 gas sensing by ZnO nanowires, Appl. Phys. Lett. 108 (2016), 071602.

[92] M. Ando, T. Kamimura, K. Uegaki, V. Biju, Y. Shiger, Sensing of ozone based on its quenching effect on the photoluminescence of CdSe-based core-shell quantum dots, Microchimica Acta 183 (2016) 3019-3024.

[93] X. Liu, B. Du, Y. Sun, M. Yu, Y. Yin, W. Tang, C. Chen, L. Sun, B. Yang, W. Cao, M. N. R. Ashfold, Sensitive Room Temperature Photoluminescence-Based Sensing of H2S with Novel CuO–ZnO Nanorods, ACS Appl. Mater. Interfaces 8 (2016) 16379-16385.

[94] W. Jakubik, Zastosowanie akustycznych fal powierzchniowych w czujnikach gazowych", Wydawnicteo Politechniki Śląskiej, Gliwice, 2012, p. 47.

[95] J. Wojas, Fizyka powierzchni półprzewodników, Akademicka Oficyna Wydawnicza PLJ, Warszawa, 1995.

[96] J. McMurry, Fundamentals of Organic Chemistry (Fith ed.), Agnus McDonald, 2003, p. 409.

[97] F. C. Tompkins, Chemisorpcja gazów na metalach, PWN, Warszawa, 1985.

[98] J. H. Bar *et al*., Struktura materii, PWN, Warszawa, 1980.

[99] D. M. Crowell, A. D. Young, Physical adsorption of gases, Butterworths, 1962.

[100] S. Brunauer, The adsorption og gases and vapors, Vol. I Physical Adsorption, Oxford University Press, London, 1943.

[101] R. Masel, Principles of Adsorption and Reaction on Solid Surfaces, Wiley Interscience, 1996, p. 240.

[102] S. Brunauer, P. H. Emmett and E. Teller, Adsorption of Gases in Multimolecular Layers, Am. Chem. Soc. 60 (1938) 309-319.

[103] A. Kahn, Fermi level, work function and vacuum level, Mater. Horiz. 3 (2016) 7-10.

[104] T. Sahm, A. Gurlo, N. Barsan, U. Weimar, Basics of oxygen and SnO2 interaction; work function change and conductivity measurements, Sens. Actuat. B: Chem 118 (2006) 78-83.

[105] A. Oprea, N. Barsan, U. Weimar, Work function changes in gas sensitive materials: Fundamentals and applications, Sens. Actuat. B: Chem 142 (2009) 470–493.

[106] G. Martinelli, M. C. Carotta, Thick-film gas sensors, Sens. Actuat. B: Chem 23 (1995), 157-161.

[107] W. H. Branttain and J. Bardeen, Hell. Si/sf. Tech. j. 32, 1 (1953).

[108] T. Seiyama, A. Kato, K. Fujiishi, and M. Nagatani, A New Detector for Gaseous Components Using Semiconductive Thin Films. Anal. Chem. 34, 1502 (1962) 1502-1503.

[109] N. Yamazoe and N. Miura, Chemical Sensor Technology (S. Yamauchi, Ed.), Vol. 4, Kodansha, Tokyo, 1992, p. 19.

[110] V. E. Bochenkov, G. B. Sergeev, Nanomaterials for sensors, Usp. Khim. 76, 11 (2007) 1084–1093.

[111] E. Kanazawa, G. Sakai, K. Shimanoe, Y. Kanmura, Y. Teraoka, N. Miura, N. Yamazoe, Metal Oxide Semiconductor N_2O Sensor for Medical Use, Sens. Actuat. B: Chem 77 (2001) 72-77.

[112] K. Arshak, E. Moore, G.M. Lyons, J. Harris, S. Clifford, A review of gas sensors employed in electronic nose applications, Sensor Review 24, 2 (2004) 181-194.

[113] C. Wang, L. Yin, L. Zhang, D. Xiang, R. Gao, Metal Oxide Gas Sensors: Sensitivity and Influencing Factors, Sensors 10 (2010) 2088-2106.

[114] S. Ahlers, G. Muller, T. Doll, A rate equation approach to the gas sensitivity of thin-film

SnO2, Sensor. Actuat. B-Chem. 107 (2005) 587–599.

[115] A. Helwig, G. Muller, G. Sberveglieri, G. Faglia, Gas response times of nano-scale SnO2 gas sensors as determined by the moving gas outlet technique. Sens. Actuat. B: Chem 126 (2007) 174–180.

[116] E. Schaller, J.O. Bosset and F. Escher, Electronic noses and their application to food, Lebensmittel-Wissenschaft und-Technologie 31, 4 (1998) 305-316.

[117] J.H. Yu, G.M. Choi, Electrical and CO Gas Sensing Properties of ZnO-SnO_2 Composites, Sens. Actuat. B: Chem 52 (1998) 251-256.

[118] B. P. J. De Lacy Costello, R. J. Ewen, P. R. H. Jones, N. M. Wat, A Study of the

Catalytic and Vapour-Sensing Properties of Zinc Oxide and Tin Dioxide in Relation to 1-Butanol and Dimethyldisulphide. Sens. Actuat. B: Chem. 61 (1999) 199-207.

[119] D.H. Yoon, J.H. Yu, G.M. Choi, CO Gas Sensing Properties of ZnO-CuO Composite, Sens. Actuat. B: Chem 46 (1998) 15-23.

[120] C. L. Zhu, Y. J. Chen, R.X. Wang, L.J. Wang, M.S. Cao, X.L. Shi, Synthesis and Enhanced Ethanol Sensing Properties of α-Fe2O3/ZnO Heteronanostructures. Sens. Actuat. B: Chem. 140 (2009) 185-189.

[121] H. Teterycz, R. Klimkiewicz, B. W. Licznerski, A New Metal Oxide Catalyst in Alcohol

Condensation. Appl. Catal. A: Gen. 214 (2001) 243-249.

[122] H. Meixner, U. Lampe, Metal Oxide Sensors, Sens. Actuat. B: Chem. 33 (1996) 198-202.

[123] N. Du, H. Zhang, B.D. Chen, X.Y. Ma, Z.H. Liu, J.B. Wu, D. R. Yang, Porous Indium Oxide Nanostructures: Layer-by-Layer Assembly on Carbon-Nanotube Templates and Application for Room-Temperature NH_3 Gas Sensors, Adv. Mater. 19, 12 (2007) 1641-1645.

[124] K. Suri, S. Annapoorni, A.K. Sarkar, R.P. Tandon, Gas and humidity sensors based on iron oxide-polypyrrole nanocomposites, Sens. Actuat. B: Chem. 81 (2002) 277-282.

[125] S. Gupta Chatterjee, S. Chatterjee, A. K. Ray, A. K. Chakraborty, Graphene-metal oxide nanohybrids for toxic gas sensor: A review, Sens. Actuat. B: Chem. 221 (2015) 1170-1181.

[126] J. Gong, Y. Li, Z. Hu, Z. Zhou, Y. Deng, Ultrasensitive NH_3 Gas Sensor from Polyaniline Nanograin Enchased TiO_2 Fibers, J. Phys. Chem. C 114, 21 (2010) 9970-9974.

[127] G. Korotcenkov, Metal Oxides for Solid-State Gas Sensors: What Determines Our Choice? Mater. Sci. Eng. B 139 (2007) 1-23.

[128] T. B. Fryberger, S. Semancik, Fundamental studies of gas sensor response mechanisms: palladium on SnO2 (110), Sens. Actuat. B: Chem. 2 (1990) 305.

[129] S. Semancik, T. B. Fryberger, Model studies of SnO_2-based gas sensors: Vacancy defects and Pd additive effects, Sens. Actuat. B: Chem. 1 (1990) 97-102.

[130] L. Madler, A. Roessler, S. F. Pratsinis, T. Sahm, A. Gurlo, N. Barsan, and U. Weimar, Direct formation of highly porous gas-sensing films by in situ thermophoretic deposition of flame-made Pt/SnO_2 nanoparticles, Sens. Actuat. B: Chem. 114 (2006) 283-295.

[131] U.-S. Choi, G. Sakai, K. Shimanoe, and N. Yamazoe, Sensing properties of Au-loaded SnO_2-Co_3O_4 composites to CO and H_2, Sens. Actuat. B: Chem. 107 (2006) 397-401.

[132] O. Wurzinger and G. Reinhardt, CO-sensing properties of doped SnO_2 sensors in H_2-rich gases, Sens. Actuat. B: Chem. 103 (2004) 104-110.

[133] R. K. Joshi, F. E. Kruis, and O. Dmitrieva, Gas sensing behavior of $SnO_{1.8}$:Ag films composed of size-selected nanoparticles, J. Nanopart. Res. 8 (2006) 797-808.

[134] J. Gong, Q. Chen, M. R. Lian, N. C. Liu, R. G. Stevenson, and F. Adami, Micromachined nanocrystalline silver doped SnO_2 H_2S sensor, Sens. Actuat. B: Chem. 114 (2006) 32-39.

[135] M. K. Kennedy, E. E. Kruis, H. Eissan, B. R. Mentha, S. Stappert, and G. Dumpich, Tailored nanoparticle films from monosized tin oxide nanocrystals: Particle synthesis, film formation, and size-dependent gas-sensing properties, J. Appl. Phys. 93 (2003) 551.

[136] D. Wang, Z. Ma, S. Dai, J. Liu, Z. Nie, M. H. Engelhard, Q. Huo, C. Wang, R. Kou, Low-Temperature Synthesis of Tunable Mesoporous Crystalline Transition Metal Oxides and Applications as Au Catalyst Supports. J. Phys. Chem. C 112 (2008) 13499-13509.

[137] D. Haridas, K. Sreenivas, V. Gupta, Improved Response Characteristics of SnO2 Thin Film Loaded with Nanoscale Catalysts for LPG Detection, Sens. Actuat. B: Chem. 133 (2008) 270-275.

[138] Y. Shimizu, N. Matsunaga, T. Hyodo, M. Egashira, Improvement of SO_2 Sensing Properties of WO_3 by Noble metal Loading, Sens. Actuat. B: Chem. 77 (2001) 35-40.

[139] G. Korotcenkov, The Role of Morphology and Crystallographic Structure of Metal Oxides in Response of Conductometric-Type Gas Sensors, Mater. Sci. Eng. R 61 (2008) 1-39.

[140] S. Ahlers, C. Muller, and T. Doll, Arate equation approach to the gas sensitivity of thin film metal oxide materials, Sens. Actuat. B: Chem. 107 (2005) 587-599.

[141] M. Iwamoto, Chemical Sensor Technology (S. Yamauchi, Ed.), Vol. 4, p. 63. Kodansha, Tokyo, 1992.

[142] S. Wlodek, K. Golbow, and F. Consadori, Kinetic model of thermally cycled tin oxide gas sensor, Sens. Actuat B: Chem. 3 (1991) 123-127.

[143] W. M. Sears, K. Colbov, and F. Consadori, Algorithms to improve the selectivity of thermally-cycled tin oxide gas sensors, Sens. Actuat. B: Chem. 19 (1989) 333-349.

[144] P.T. Moseley, Materials selection for semiconductor gas sensors, Sens. Actuators B 6 (1992) 149–156.

[145] Y. Sadaoka, Organic semiconductor gas sensors, in: G. Sbeveglieri (Ed) Gas sensors, Kluwer Academic, Dordrecht, 1992, p. 187-218.

[146] S. Mubeen, T. Zhang, B. Yoo, M. A. Deshusses, N. V. Myung, Palladium Nanoparticles Decorated Single-Walled Carbon Nanotube Hydrogen Sensor, J. Phys. Chem. C 111 (2007) 6321-6327.

[147] M. Bouvet, P. Gaudillat, J. M. Suisse, Phthalocyanine-based hybrid materials for chemosensing, J. Porphyrins Phthalocyanines 17 (2013) 913.

[148] J. Brunet, A. Pauly, L. Mazet, J.P. Germain, M. Bouvet, B. Malezieux, Improvement in real time detection and selectivity of phthalocyanine gas sensors dedicated to oxidizing pollutants evaluation, Thin Solid Films 490 (2005) 28-35.

[149] J.D. Wright, Gas adsorption on phthalocyanines and its effects on electrical properties,

Prog. Surface Sci. 31 (1989) 1.

[150] A.W. Snow, W.R. Barger, in: C.C. Leznoff, A.B.P. Lever (Eds.), Phthalocyanine. Properties and Applications, VCH, New York, 1989, 341.

[151] Z. Pei, X. Ma, P. Ding, W. Zhang, Z. Luo, G. Li, Study of a QCM Dimethyl Methylphosphonate Sensor Based on a ZnO-Modified Nanowire-Structured Manganese Dioxide Film, Sensors 10 (2010), 10, 8275-8290.

[152] A. A. Tomchenko, G. P. Harmer, B. T. Marquis, Detection of chemical warfare agents using nanostructured metal oxide sensors, Sens. Actuat. B: Chem 108 (2005) 41–55.

[153] J. Jun, J. S. Lee, D. H. Shin, J. Oh, W. Kim, W. Na and J. Jang, Fabrication of a one-dimensional tube-in-tube polypyrrole/tin oxide structure for highly sensitive DMMP sensor applications, J. Mater. Chem. A 5 (2017) 17335-17340

[154] T. Alizadeh, L. H. Soltani, Reduced Graphene oxide-based gas sensor array for pattern recognition of DMMP vapor, Sens. Actuat. B: Chem. 234 (2016) 361-370.

[155] Y. Zhu, Z. Cheng, Q. Xiang, X. Chen, J. Xu, Synthesis of functionalized mesoporous TiO_2-SiO_2 with organic fluoroalcohol as high performance DMMP gas sensor, Sens. Actuat. B: Chem. 248 (2017) 785-792.

[156] R. Yoo, S. Too, D. Lee, J. Kim, S. Cho, W. Lee, Highly selective detection of dimethyl methylphosphonate (DMMP) using CuO nanoparticles/ZnO flowers heterojunction, Sens. Actuat. B: Chem. 240 (2017) 1099-1105.

[157] T. A. Temofonte, K. F. Schoch, Phthalocyanine semiconductor sensors for room-temperature ppb level detection of toxic gases, J.Appl. Phys. 65 (1989) 1350.

[158] Y. Wang, N. Hu, Z. Zhou, D. Xu, Z. Wang, Z. Yang, H. Wei, E. s-W Kong, Y. Zhang, Single-walled carbon nanotube/conalt phthalocyanine derivative hybrid material: preparation, characterization and its gas sensing properties, J. Mater. Chem. (2011) 3779-3787.

[159] P-H. Wang, J-H. Yu, Z-J. Li, Z-J. Ding, L. Guo, B. Du, Synthesis and evaluation of a new phthalocyanine as sensor material for sarin detection, Sens. Actuat. B: Chem. 188 (2013) 1306-1311.

[160] D. A. Chen, J. S. Ratliff, X. Hu, W.O. Gordon, S. D. Senanayake, D. R. Mullins, Dimethyl Methylphosphonate Decomposition on Fully Oxidized and Partially Reduced Ceria Thin Films, Surf. Sci. 604 (2010) 574-587.

[161] Y. J. Jang, K. Kim, O. G. Tsay, D. A. Atwood, D. G. Churchill, Update 1 of: Destruction and Detection of Chemical Warfare Agents, Chem. Rev. 115 (2015) PR1−PR76.

[162] V. N. Sheinker, M. B. Mitchell, Quantitative Study of the Decomposition of Dimethyl Methylphosphonate (DMMP) on Metal Oxides at Room Temperature and Above, Chem. Mater. 14 (2002) 1257−1268.

[163] S. Ma, J. Zhou, Y. Kang, J. Reddic, D. Chen, Dimethyl Methylphosphonate Decomposition on Cu Surfaces: Supported Cu Nanoclusters and Films on TiO2 (110). Langmuir 20 (2004) 9686−9694.

[164] L. Cao, S.R. Segal, S.L. Suib, X. Tang, S. Satyapal, Thermocatalytic oxidation of dimethyl methylphosphonate on supported metal oxides, J. Catal. 194 (2000) 61-70.

[165] L. Cao, S.L. Suib, X. Tang, S. Satyapal, Thermocatalytic decomposition of dimethyl methylphosphonate on activated carbon, J. Catal., 197 (2001) 236-243.

[166] J. W. Grate, M. H. Abraham, Solubility interactions and the design of chemically selective sorbent coatings for chemical sensors and arrays, Sens. Actuat. B: Chem. 3 (1991) 85-111.

[167] J. W. Grate, Acoustic Wave Microsensor Arrays for Vapor Sensing, Chem. Rev. 100 (2000) 2627-2648.

[168] A. Hierlemann, A. J. Ricco, K. Bodenhofer, W. Gopel, Effective Use of Molecular Recognition in Gas Sensing: Results from Acoustic Wave and in Situ FT-IR Measurements, Anal. Chem. 71 (1999) 3022-3035.

[169] M. S. Liao, T. Kar, S. M. Gorun, S. Scheiner, Effects of Peripheral Substituents and Axial Ligands on the Electronic Structure and Properties of Iron Phthalocyanine, Inorg. Chem. 43 (2004) 7151–7161.

[170] R. Tongpool, S. Yoriya, Kinetics of nitrogen dioxide exposure in lead phthalocyanine sensors, Thin Solid Films 477 (2005) 148-152.

[171] Y. L. Lee, W. C. Tsai, C. H. Chang, Y. M. Yang, Appl. Surf. Sci. 172 (2001) 191-199.

[172] K. Suto, S. Yoshimoto, K. Itaya, Two-Dimensional Self-Organization of Phthalocyanine and Porphiryn: Dependence on the Crystallographic Orientation of Au, J. Am. Chem. Soc. 125, 49 (2013) 14976-14977.

[173] S. Kera, M. B. Casu, K. R. Bauchspies, D. Batchelor, Th. Schmidt, E. Umbach, E. Growth mode and molecular orientation of phthalocyanine molecules on metal single crystal substrates: A NEXAFS and XPS study, Surf. Sci. 600 (2006) 1077-1084.

[174] L. Gaffo, M. R. Cordeiro, A. R. Freitas, W. C. Moreira, E. M. Girotto, V. Zucolotto, The effects of temperature on the molecular orientation of zinc phthalocyanine films, J Mater Sci. 45 (2010) 1366-1370.

[175] J. J. Cox, S. M. Bayliss, T. S. Jones, Influence of substrate orientation on the formation of ordered copper phthalocyanine overlayers on InAs, Surf. Sci. 425 (1999) 326-333.

[176] J. S. Louis, D. Lehmann, M. Friedrich, D. R. T. Zahn, Study of dependence of molecular orientation of zinc phthslocyanine grown under two different pressure conditions, J. Appl. Phys 101 (2007) 013503.

[177] J. A. Pople, Nobel lecture: Quantum chemical models, Rev. Mod. Phys. 71 (1999) 1267–1274.

[178] P. Hohenberg and W. Kohn, Inhomogeneous electron gas, Phys. Rev. 136 (1964) B864–B871.

[179] K. I. Ramachandran, D. Gopakumar, K. Namboori, Computational Chemistry and Molecular Modeling: Principles and Applications, Springer, 2008, p. 5.

[180] M. J. S. Dewar and W. Thiel, Ground states of molecules. 39. MNDO results for molecules containing hydrogen, carbon, nitrogen, and oxygen, J. Am. Chem. Soc. 99 (1977) 4907–4917.

[181] 181 M. J. S. Dewar and W. Thiel, Ground states of molecules. 38. MNDO method. Approximations and parameters, J. Am. Chem. Soc. 99 (1977) 4899–4907.

[182] M. J. S. Dewar, E. G. Zoebisch, E. F. Healy, J. J. P. Stewart, The development and use of quantum mechanical molecular model, J. Am. Chem. Soc. 107 (1985) 3902–3909.

[183] J. J. P. Stewart, Optimization of parameters for semiempirical methods I. Method, J. Comp. Chem. 10 (1989) 209–220.

[184] J. J. P. Stewart, Optimization of parameters for semiempirical methods I. Applications, J. Comp. Chem. 10 (1989) 221–264.

[185] J. J. P. Stewart, Optimization of parameters for semiempirical methods. III Extension od PM3 to Be, Mg, Zn, Ga, Ge, As, Se, Cd, In, Sn, Sb, Te, Hg, Tl, Pb, and Bi, J. Comp. Chem. 12 (1991) 320–341.

[186] E. Anders, R. Koch, and P. Freunscht, Optimization and application of lithium parameters for PM3, J. Comp. Chem. 14 (1993) 1301-12.

[187] J. J. P Stewart, Optimization of parameters for semiempirical methods V: Modification of NDDO approximations and application to 70 elements, J. Mol. Model. 13 (2007) 1173-1213.

[188] J. Řezáč, J. Fanfrlík, D. Salahub, P. Hobza, Semiempirical Quantum Chemical PM6 Method Augmented by Dispersion and H-Bonding Correction Terms Reliably Describes Various Types of Noncovalent Complexes, J. Chem. Theory Comput.57 (2009) 1749-1760.

[189] E. Broclawik, R. Yamauchi, A. Endou, M. Kubo, A. Miyamoto, Density functional study on the activation of methane over Pd_2, PdO, and Pd_2O clusters, Int. J. Quantum Chem. 61 (1997) 673-682.

[190] W. Kohn and L. J. Sham, Self-consistent equations including exchange and correlation effects, Phys. Rev. 140 (1965) A1133–A1138.

[191] R. O. Jones and O. Gunnarsson, The density functional formalism, its applications and prospects, Rev. Mod. Phys. 61 (1989) 689–746.

[192] W. Kohn, L. J. Sham, Self-consistent equations including exchange and correlation effects, Phys. Rev. 140 (1965) 1133-1138.

[193] D. M. Ceperley and B. J. Alder, Ground state of the electron gas by a stochastic method, Phys. Rev. Lett., 45 (1980) 566–569.

[194] A. J. Cohen and N. C. Handy, Assessement of exchange correlation functionals. Chem. Phys. Lett. 316 (2000) 160-166.

[195] D. R. Hamann, H2O hydrogen bonding in density-functional theory, Phys. Rev. B 55 (1997) R10157–R10160.

[196] J. P. Perdew, J. A. Chevary, S. H. Vosko, K. A. Jackson, M. R. Pederson, D. J. Singh, and C. Fiolhais, Atoms, molecules, solids, and surfaces: Applications of the generalized gradient approximation for exchange and correlation, Phys. Rev. B 46 (1992) 6671–6687.

[197] J. P. Perdew, K. Burke, and M. Ernzerhof, Generalized Gradient Approximation Made Simple, Phys. Rev. Lett. 77 (1996) 3865–3868.

[198] H. J. Monkhorst and J. D. Pack, Spatial points for Brillouin-zone integrations, Phys. Rev. B 40 (1989) 3616-3621.

[199] M. Methfessel and A. T. Paxton, High-precision sampling for Brillouin-zone integration

in metals, Phys. Rev. B 40 (1989) 3616–3621.

[200] N. Marzari, D. Vanderbilt, A. De Vita, and M. C. Payne, Thermal Contraction and Disordering of the Al (110) Surface, Phys. Rev. Lett. 82 (1999) 3296–3299.

[201] D. R. Hamann, M. Schlüter, and C. Chiang, Norm-conserving pseudopotentials, Phys. Rev. Lett. 43 (1979) 1494–1497.

[202] D. Vanderbilt, Soft self-consistent pseudopotentials in a generalized eigenvalue formalism, Phys. Rev. B 41 (1990) 7892–7895.

[203] P. E. Blöchl, Projector augmented-wave method, Phys. Rev. B 50 (1994) 17953–17979.

[204] P. Giannozzi, S. Baroni, N. Bonini, M. Calandra, R. Car, C. Cavazzoni, D. Ceresoli, G. L. Chiarotti, M. Cococcioni, I. Dabo, et al. QUANTUM ESPRESSO: a Modular and Open-Source Software Project for Quantum Simulations of Materials, J. Phys.: Condens. Matter 21 (2009) 395502.

[205] J. P. Perdew, K. Burke, M. Ernzerhof, Generalized Gradient Approximation Made Simple, Phys. Rev. Lett. 77 (1996) 3865−3868.

[206] F. Ortmann, F. Bechstedt, W. G. Schmidt, Semiempirical van der Waals Correction to the Density Functional Description of Solids and Molecular Structures, Phys. Rev. B: Condens. Matter Mater. Phys. 73 (2006) 205101.

[207] H. Hertz, Ann. Phys. (Leipzig) 31 (1887) 983.

[208] A. Einstein, Ann. Phys. (Leipzig) 17 (1905) 132.

[209] K. Siegbahn, C. Nordling, A. Fahlman, H. Nordberg, K. Hamrin, J. Hedman, G. Johansson, T. Bergmark, S. E. Karlsson, J. Lindgren, and B. Lindberg, E.s.c.a.: atomic, molecular and solid state structure studied by means of electron spectroscopy, Nova Acta Soc. Sci. Uppsala, Ser. IV 20 (1967).

[210] D. W. Turner, C. Baker, A.D. Baker, and C.R. Brundle, Molecular Photoelectron Spectroscopy, Wiley, London, 1970.

[211] W.E. Spicer, Photoemissive, Photoconductive, and Optical Absorption Studies of Alkali-Antimony Compounds, Phys. Rev. 112 (1958) 114.

[212] S. Hufner, Photoelectron Spectroscopy. Principles and Applications, Springer, 2003.

[213] J. W. Niemantsverdriet, Spectroscopy in Catalysis: An Introduction, Third Edition, Wiley VCH, 2007.

[214] V.L. Moruzzi, J.F. Janak, and A.R. Williams, Calculated Electronic Properties of Metals. Pergamon, New York, 1978.

[215] J. W. Niemantsverdriet, K. Markert and K. Wandelt, The compensation effect and the manifestation of lateral interactions in thermal desorption spectroscopy, Appl. Surf. Sci. 31 (1988) 211-219.

[216] P. A. Redhead, Thermal desorption of gases, Vacuum 12 (1962) 203-211.

[217] B.C. Gates, Catalytic Chemistry, Wiley, New York, 1992.

[218] C. M. Chan, R. Aris, and W.H. Weinberg, Analysis of thermal desorption mass spectra. I., Appl. Surface Sci. 1 (1978) 360-376.

[219] E. Habenschaden and J. Kuppers, Evaluation of flash desorption spectra, Surface Sci. 138 (1984) L147- L150.

[220] A. M. de Jong, J. W. Niemantsverdriet, Thermal desorption analysis: Comparative test of ten commonly applied procedures, Surf. Sci. 233 (1990) 355-365.

[221] S. N. Magonov, Visualization of Nanostructures with Atomic Force Microscopy, in: N. Yao, Z. L. Wang (Ed) Handbook of Microscopy for Nanotechnology, Springer, 2005, p. 113-155.

[222] E. Meyer, H.J. Hug, and R. Bennewitz, Scanning Probe Microscopy, The Lab on a Tip, Springer-Verlag, Berlin, 2004.

[223] S. Morita, R. Wiesendanger, and E. Meyer (Eds.), Noncontact Atomic Force Microscopy, Springer-Verlag, Berlin, 2002.

[224] D. Sarid, Scanning Force Microscopy with Applications to Electric, Magnetic and Atomic Forces. Oxford University Press, New York, 1991.

[225] http://www.parkafm.com/index.php/park-spm-modes

[226] http://gwyddion.net/documentation/

[227] M. Krzywiecki, L. Grządziel, J. Juszczyk, A. Kaźmierczak-Bałata, A. Erbe, J. Bodzenta, J. Phys. D: Appl. Phys. 47 (2014) 335304.

[228] M. Krzywiecki, L. Grządziel, J. Bodzenta, J. Szuber, Thin Solid Films, 520 (2012) 3965.

[229] P. Powroźnik, M. Krzywiecki, L. Grządziel and W. Jakubik, Study of sensing mechanisms in nerve agent sensors based on phthalocyanine-palladium structures, Procedia Engineering 168 (2016) 586-589.

[230] P. Powroźnik, W. Jakubik, A. Kaźmierczak-Bałata, Detection of organophosphorus (DMMP) vapour using phthalocyanine-palladium bilayer structures, Procedia Engineering 120 (2015) 368-371.

[231] M. Szybowicz, J. Makowiecki, Orientation study of iron phthalocyanine (FePc) thin films deposited on silicon substrate investigated by atomic force microscopy and micro-Raman spectroscopy, J. Mater. Sci. 47 (2012) 1522-1530.

[232] L. Grządziel, J. Żak, J. Szuber, On the correlation between morphology and electronic properties of copper phthalocyanine (CuPc) thin films, Thin Solid Films 436 (2003) 70-75.

[233] J. Zhang, X. Liu, G. Neri and N. Pinna, Nanostructured materials for room-temperature gas sensors, Adv. Mater. 28 (2016) 795-831.

[234] S. Abdulla, T. Lazar Mathew, B. Pullithadathil, Highly sensitive, room temperature gas sensor based on polyaniline-multiwalled carbon nanotubes (PANI/MWCNTs) nanocomposite for trace-level ammonia detection, Sensor. Actuat. B-Chem 221 (2015) 1523-1534.

[235] C. Shao, Y. Chang, Y. Long, High performance of nanostructured ZnO film gas sensor at room temperature, Sensor. Actuat. B-Chem 204 (2014) 666-672.

[236] K. Kudo, T. Sumimoto, K. Hiraga, S. Kuniyoshi, K. Tanaka, Evaluation of electrical properties of evaporated thin films of metal-free, copper and lead phthalocyanines by in-situ field effect measurements, Jpn. J. Appl. Phys. 36 (1997) 6994-6998.

[237] R. Evans, U. Marini Bettolo Marconi and P. Tarazona, Fluids in narrow pores: Adsorption, capillary condensation and critical points, J. Chem. Phys. 84 (1986) 2376.

[238] P. Powroźnik, L. Grządziel, W. Jakubik, M. Krzywiecki, Sarin-simulant detection by phthalocyanine/palladium structures: From modeling to real sensor response, Sens. Actuat. B: Chem. 273 (2018) 771-777.

[239] E. Broclawik, R. Yamauchi, A. Endou, M. Kubo, A. Miyamoto, Density functional study on the activation of methane over Pd2, PdO, and Pd2O clusters, Int. J. Quantum Chem. 61 (1997) 673-682.

[240] M. Melle-Franco and G. Pacchioni, CO Adsorption on SnO_2(110): Cluster and Periodic Ab Initio Calculations, Surf. Sci. 461 (2000) 54–66.

[241] W Brutting, ed. Physics of Organic Semiconductor, Wiley-VCH Verlag, 2005.

[242] A. S. Bolina, A. J. Wolff and W. A. Brown, Reflection Absorption Infrared Spectroscopy and Temperature-Programmed Desorption Studies of the Adsorption and Desorption of Amorphous and Crystalline Water on a Graphite Surface, J. Phys. Chem. B 109 (2015) 16836-16845.

[243] H. F. Xiang, H. Y. Xu, Z. Z. Wang, C. H. Chen, Dimethyl methylphosphonate (DMMP) as an efficient flame retardant additive for the lithium-ion battery electrolytes, J. Power Sources 173 (2007) 562-564.

[244] X. Lu, Design and study of lyotropic liquid crystal-butyl rubber nanocomposites for chemical agent vapor barrier applications, ProQuest, 2007.

[245] L. Grządziel, M. Krzywiecki, Surface states and space charge layer electronic parameters specification for long term air-exposed copper phthalocyanine thin films, Thin Solid Films 550 (2014) 361-366.

[246] X. Yan, H. Wang, D. Yan, An investigation on air stability of copper phthalocyanine-based organic thin-film transistors and device encapsulation, Thin Solid Films 515 (2006) 2655-2658.

[247] D. A. Evans, H. J. Steiner, S. Evans, R. Middleton, T. S. Jones, S. Park, T.U. Kampen, D. R. T. Zahn, G. Cabailh, I. T. McGovern, Copper phthalocyanine on InSb(111)A-interface bonding, growth mode and energy band alignment, J. Phys.: Condens. Matter 15 (2003) S2729-S2740.

[248] M.-S. Liao and S. Scheiner, Electronic Structure and Bonding in Metal Phthalocyanines, Metal = Fe, Co, Ni, Cu, Zn, Mg, J. Chem. Phys. 114 (2001) 9780.

[249] H. Guo, Y. Wang, S. Du, H. Gao, High-resolution scanning tunneling microscopy imaging of Si (1 1 1)-7x7 structure and intrinsic molecular states, J. Phys.: Condens. Matter 26, 39 (2014).

[250] S. Ahmadi, M. N. Shariati, S. Yu, M. Gothelid, Molecular layers of ZnPc and FePc on Au(111) surface: Charge transfer and chemical interaction, J. Chem. Phys. 137 (2012)

[251] R. Hiesgen, M. Rabisch, H. Bottcher, D. Meissner, STM investigation of the growth structure of Cu-phthalocyanine films with submolecular resolution, Sol. Energy Mater. Sol. Cells 61 (2000) 73-85.

[252] T. D. Sims, J. E. Pemberton, P. Lee, N. R. Armstrong, Comparison of supermolecular aggregate structure and spectroscopic and photoelectrochemical properties of tetravalent and trivalent metal phthalocyanine thin films, Chem. Mater. 1 (1989) 26-34.

[253] W. Gao, A. Kahn, Controlled *p*-doping of zinc phthalocyanine by coevaporation with tetrafluorotetracyanoquinodimethane: A direct and inverse photoemission study, Appl. Phys. Lett. 78, 4040 (2001).

[254] J. P. Contour, P. Lenfant, A.K. Vijh, gas-phase chemisorption and electroreduction of oxygen on phthalocyanines, J. Catal. 29 (1973) 8-14.